Università degli Studi di Firenze
Vrije Universiteit Brussel
Joint PhD
Cycle XXXI, 2015-2019

Wind tunnel testing of small Vertical-Axis Wind Turbines for urban areas

Candidate
Andreu Carbó Molina

Supervisors
Prof. Gianni Bartoli

Prof. Tim De Troyer

PhD Coordinator
Prof. Claudio Borri

8th November 2019

Thesis submitted in partial fulfillment of the requirements for the degree of Doctor of Philosophy in International Doctorate in Civil and Environmental Engineering.

Any way the wind blows...

- Freddie Mercury, Bohemian Rhapsody.

Acknowledgments

I would like to express my gratitude for the support, help and wisdom received from my two supervisors, Prof. Gianni Bartoli and Prof. Tim De Troyer. Also, appreciate the possibility of testing at the VKI and the recommendation for this position given by Prof. Jeroen van Beeck. And to thank Prof. Claudio Borri and Dr. Enzo Marino for giving me this great opportunity within the AEOLUS4FUTURE project.

I would like to acknowledge the careful review and feedback given by my two external reviewers, prof. Marius Paraschivoiu and Prof. Valerio Iungo, and by the other members of the jury of my thesis, Prof. Marc C. Runacres, Prof. Giovanni Ferrara, Prof. Roger Vounckx and Prof. Klaus Thiele.

I am also very grateful for the help and contribution to this project done by all my colleagues at UniFI and VUB, in particular Tommaso Massai, Antoine Vergaerde, Alessandro Bianchini and Francesco Balduzzi who collaborated on the main parts of my research work.

And because not all the work was done within the walls of the university, I would like to praise all the friends I made during these three years, the Humans in Florence and the AEOLUS4FUTURE crew, who made me feel like at home wherever I travelled during this period.

Finally, I would like to send my love to all my friends and family that took some days off to visit me in Florence and Brussels, and specially to my partner Elena who made a three-year long-distance relationship such an easy and pleasant ride. And at the end, I would never thank enough all the love and support that my parents have given me during all my life.

Abstract

The implementation of small vertical-axis wind turbines (VAWTs) in urban environments is being studied by the scientific community to complement large wind farms in wind energy generation. The technology is, however, far from maturity due to the complexity of urban flows and the lack of knowledge in the field. This thesis focuses on turbulence, one of the main characteristics of urban flows, and its influence on VAWT performance. Its objective is to generate turbulent wind conditions inside a wind tunnel and testing a VAWT to determine how turbulence intensity (I_u) and integral length scale (L_{ux}) affect its operation.

The first part of the research was devoted to obtaining highly-turbulent wind profiles in the wind tunnel with the use of different configurations of square grids. Gathering experience from previous studies and literature, a careful study and validation of this technique was done, in order to obtain uniform wind conditions with the adequate values of turbulence intensity and length scales to model the urban flows. Then, a H-Darrieus VAWT prototype was tested under these turbulent conditions in two different wind tunnels (VUB in Belgium, and CRIACIV in Italy). Those campaigns allowed to evaluate the crossed effect of I_u, L_{ux} and Reynolds numbers on the VAWT performance, and quantify the effect of wind tunnel blockage in the measurements. Further tests with the same set-up included the study of the near wake of the VAWT and the aerodynamic characteristics of the individual blades, always focusing on the effect of incoming turbulence. Finally, a short campaign was done at the large VKI L1-B wind tunnel (in Belgium) to observe the effect of a shear flow with high levels of L_{ux} (impossible to model in smaller wind tunnels).

The tests on the VAWT revealed an important increase of performance for low to moderate I_u values (5 - 15%) in low chord-based Reynolds numbers ($\mathrm{Re}_c < 100000$), while the effect of L_{ux} was negligible. I_u also proved to cause a positive effect by providing faster wake recovery and by mitigating the negative effect of the turbine shaft. The study of the effect of turbulence on the aerodynamic coefficients of different typical VAWT aerofoils showed that turbulence considerably delays the stall in the blades, which was linked the increase of turbine performance. The tests at VKI proved that this positive effect of turbulence is also evident in shear flows. The possibility of testing in three different wind tunnels strengthens the results of this study, which have been already used in combination with CFD simulations, and present good agreement with literature. The findings of this thesis contribute to expand the knowledge of how turbulent flows interact with VAWT, and provide a useful insight for the optimization and combination of several VAWTs inside urban environments.

Sommario

Le mini-turbine ad asse verticale (VAWTs nell'acronimo inglese), sono considerate dalla comunità scientifica complementari ai grandi parchi eolici per la generazione di energia in ambiente urbano. Questa tecnologia, tuttavia, è lontana dell'esser considerata matura, in ragione della complessità dei flussi urbani e la mancanza di conoscenze riguardo a diversi fattori in questo campo. La presente tesi concerne lo studio della turbolenza, una delle caratteristiche più importanti dei flussi urbani, e il suo effetto nell'operatività ed efficienza delle VAWTs. Tale obiettivo è stato investigato generando condizioni di turbolenza omogenea dentro le camere di prova delle gallerie del vento utilizzate, testando un modello di VAWT per determinare le modalità con cui l'intensità di turbolenza (I_u) e la sua scala integrale (L_{ux}) affliggono la sua operatività.

Nella prima parte dello studio si è cercato di ottenere profili di vento con elevata intensità di turbolenza dentro la galleria, usando griglie di turbolenza in diverse configurazioni. Con l'esperienza maturata in precedenti studi e l'indagine di letteratura in questo campo, sono stati generati profili di vento uniformi, con valori di intensità di turbolenza e scala integrale simili a quelli trovati in ambienti urbani. In seguito, il modello di VAWT, tipologia H-Darrieus, è stato testato nelle condizioni selezionate in due diverse gallerie (VUB in Belgio e CRIACIV in Italia). Queste prove hanno permesso di studiare l'effetto di I_u, L_{ux} e Re_c (numero di Reynolds) sul rendimento della turbina, valutando anche l'influenza del bloccaggio nelle misure. Ulteriori prove con lo stesso set-up sono state effettuate per studiare le caratteristiche aerodinamiche sia della scia della turbina in rotazione sia della sezione della pala impiegata, sempre con speciale attenzione all'effetto della turbolenza. Infine, una breve campagna di misura è stata fatta nella grande galleria del vento VKI L-1 (in Belgio) per osservare l'effetto dello shear flow (flusso con importanti gradienti di velocità e quindi sforzi di taglio significativi) con alti livelli di L_{ux} (impossibile da modellare in gallerie del vento più piccole).

Le prove sulla turbina hanno rivelato un incremento sostanziale del rendimento della turbina per valori bassi e moderati di I_u (5 - 15%) in numeri di Reynolds bassi ($\mathrm{Re}_c < 100000$), mentre l'effetto della L_{ux} risulta trascurabile. L'intensità di turbolenza causa anche un recupero della scia più veloce e mitiga gli effetti negativi indotti dalla scia dell'asse della turbina. Lo studio dei coefficienti aerodinamici in diversi profili alari tipici delle VAWT ha an-

che dimostrato che la turbolenza ritarda considerevolmente l'angolo di stallo delle pale, fatto connesso con l'incremento nel rendimento della turbina. Le prove effettuate al VKI mostrano che questo effetto è anche visibile in flussi con sforzi di taglio significativi. La possibilità di sperimentare in tre gallerie del vento diverse irrobustisce i risultati di questo studio, che sono peraltro già stati utilizzati in combinazione con simulazioni numeriche (CFD), e che si trovano d'accordo con altri studi nello medesimo ambito di ricerca. I risultati di questa tesi contribuiscono a espandere le conoscenze su come i flussi turbolenti interagiscono con le VAWTs, e apportano informazioni importanti sull'operatività e interazione di più VAWTs in ambienti urbani.

Abstract

De installatie van kleine verticale-as windturbines (VAWTs) in stedelijke omgeving geniet tegenwoordig van een bijzondere interesse uit de wetenschappelijke gemeenschap, ter aanvulling van de huidige, grote windturbineparken. De technologie van zulke verticale-as windturbines voor de stedelijke omgeving is echter nog niet afdoende ontwikkeld voor de complexe windstromingen die er heersen. Deze thesis focust op turbulente stromingen, kenmerkend voor stedelijke windstromingen, en de invloed die dergelijke stromingen hebben op de prestatie van VAWTs. Het doel van de thesis omvat het opleggen van turbulente windstromingen in een windtunnel, om na te gaan hoe de prestatie van een VAWT beïnvloed wordt door turbulentie-intensiteit (I_u) en integrale lengteschaal (L_{ux}).

Het eerste deel van het onderzoek werd gewijd aan het verkrijgen van uniforme, hoog-turbulente windprofielen in een windtunnel door gebruik te maken van verschillende roosters met variërende configuraties. Ervaring werd opgedaan uit voorgaand onderzoek en literatuurstudies om vervolgens de gebruikte techniek (het gebruik van roosters) te valideren. Deze validatie diende ter keuring van het turbulentieniveau met bijhorende integrale lengteschaal in de uniforme stroming om stedelijke windcondities te reproduceren. Vervolgens werd een H-Darrieus VAWT-prototype grondig getest in dergelijke turbulente stromingen in twee verschillende windtunnels (VUB in België en CRIACIV in Italië). Dankzij deze campagnes kon het samenhangend effect tussen I_u, L_{ux} en het Reynoldsgetal geëvalueerd worden op de prestatie van de VAWT. Daarbovenop kon, dankzij het gebruik van twee verschillende windtunnels, ook een wand-interferentie-effect geïdentificeerd worden. Andere experimentele testen (gebruikmakend van dezelfde opstelling) omvatten een analyse van het nabije zog van de VAWT en de aerodynamische karakteristieken van de individuele vleugelprofielen, waarbij de focus nog steeds op het effect van turbulentie lag. Uiteindelijk werd een laatste, kortere meetcampagne uitgevoerd in de grote VKI L1-B-windtunnel (in België) om het effect van een stroming met sterke verticale gradiënt en hoge Lux op de VAWT-prestatie waar te nemen (dit is immers niet te modelleren in kleinere faciliteiten).

Het resultaat van de testen onthulde een significante toename van de VAWT-prestatie voor kleine tot matige waarden van I_u (5 - 15%) in lage Reynoldsgetallen gebaseerd op de vleugelkoorde ($\mathrm{Re}_c < 100000$). Daarente-

gen was het effect van L_{ux} verwaarloosbaar, terwijl het positieve effect gelinkt aan I_u een korter zog-herstel waarborgt en daarbovenop ook het negatieve effect van de turbine-as drukt. Een studie van het turbulentie-effect op de aerodynamische coëfficiënten van verscheidene typische VAWT-vleugelprofielen gaf aan dat loshaking aanzienlijk uitgesteld werd. Dit effect is één verklaring voor de toegenomen energieproductie van een VAWT in turbulente omgeving. De testen aan het VKI duidden dat dit positieve turbulentie-effect ook terug te vinden was in de stroming gekarakteriseerd door de sterke schuifspanningen. Doordat deze studie in drie verschillende windtunnel uitgevoerd werd kon de corroboratiegraad van de resultaten verhoogd worden. Deze resultaten werden inmiddels gebruikt in combinatie met CFD-analyses en vertonen een goede overeenkomst met de literatuur. De bevindingen in deze thesis dragen bij tot een uitgebreidere kennis van de invloed van turbulente stroming en hun interactie met VAWTs. Deze inzichten kunnen worden gebruikt om de optimalisatie en combinatie van VAWTs in de stedelijke omgeving uit te breiden.

Resumen

La instalación de pequeñas turbinas de eje vertical (VAWTs en su acrónimo inglés) en ambientes urbanos está siendo estudiada por la comunidad científica para complementar los grandes parques eólicos en la generación de energía. Esta tecnología, sin embargo, se encuentra aún en la fase de desarrollo debido a la complejidad de los vientos dentro de las ciudades y a la falta de conocimientos en este campo. Esta tesis está centrada en el estudio de la turbulencia, una de las principales características de los flujos de aire urbanos, y su influencia en el rendimiento de las VAWTs. Con ese objetivo, se han generado condiciones de alta turbulencia dentro de los túneles de viento utilizados y se ha medido cómo la intensidad de la turbulencia (I_u) y su escala integral (L_{ux}) afectan a la operación de una VAWT.

La primera parte de la investigación ha consistido en emplear diferentes configuraciones de redes cuadradas con el fin de modelar experimentalmente perfiles de viento con alta turbulencia. Combinando la experiencia previa y la bibliografía, se ha realizado un estudio detallado de esta técnica para obtener perfiles uniformes de viento con valores de intensidad y escala integral de turbulencia similar a los valores típicos de los ambientes urbanos. A continuación, un prototipo de VAWT del tipo H-Darrieus ha sido probado bajo esas condiciones en dos túneles de viento distintos (VUB en Bélgica y CRIACIV en Italia). Estas pruebas han permitido evaluar el efecto cruzado de I_u, L_{ux} y el número de Reynolds en el rendimiento de la turbina y valorar el efecto de la obstrucción (*blockage* en inglés) en los resultados. Usando el mismo set-up se han realizado otras pruebas para analizar la estela de la turbina y la aerodinámica de las palas, siempre centrándose en el efecto de la turbulencia. Finalmente se realizó también una campaña de experimentos en el túnel de viento L1-B en el VKI (Bélgica), que debido a su gran tamaño permite generar flujos de viento cortante con altos niveles de L_{ux} (imposibles de generar en túneles más pequeños).

Las pruebas sobre la turbina han mostrado una mejora sustancial de rendimiento para valores moderados de I_u (5 - 15%) en bajos números de Reynolds ($\mathrm{Re}_c < 100000$), mientras que el efecto de L_{ux} es mínimo. I_u también tiene un efecto positivo en la recuperación de la estela y mitiga la resistencia aerodinámica del eje de la turbina. El estudio del efecto de la turbulencia en la aerodinámica de las palas muestra un aumento de los ángulos de entrada en pérdida cuanto mayor es I_u, lo que justificaría la mejora del rendimiento de la VAWT detectado previamente. Las pruebas realizadas en el VKI han demostrado que este efecto de I_u también ocurre bajo flujos cortantes. La posibilidad de realizar experimentos en tres túneles de viento distintos refuerza los resultados de este estudio, que ya han sido publicados en combinación con simulaciones numéricas (CFD) y concuerdan con otras investigaciones realizadas en el mismo campo. Las conclusiones de esta tesis contribuyen a expandir el conocimiento sobre cómo los flujos turbulentos interactúan con las VAWTs y proporcionan información importante para la optimización y operación de VAWTs en ambientes urbanos.

Contents

List of Figures

List of Tables

List of Symbols

Acronyms

ABL	Atmospheric Boundary Layer
CFD	Computational Fluid Dynamics
$CRIACIV$	Centro di Ricerca Interuniversitario di Aerodinamica delle Costruzioni e Ingegneria del Vento
DC	Direct Current
$HAWT$	Horizontal-Axis Wind Turbine
HWA	Hot Wire Anemometer
IEA	International Energy Agency
ITN	Innovative Training Network
LES	Large Eddy Simulation
SST	Single Stream-Tube model
SWT	Small Wind Turbine
UBL	Urban Boundary Layer
$VAWT$	Vertical-Axis Wind Turbine
VKI	Von Karman Institute for Fluid Dynamics
VUB	Vrije Universiteit Brussel

Roman letters

A	Frontal area (m^2)
b	bar size (m)
c	Blade chord (m)
C_D	Drag coefficient
C_L	Lift coefficient
C_N	Normal force coefficient
C_P	Power coefficient
C_p	Pressure coefficient
D	Drag (N)
f	Frequency (Hz)
F	Force (N)
H	Turbine height (m)
I_{per}	Periodic unsteadiness
I_u	Turbulence intensity in the longitudinal direction (%)
k	Reduced frequency
k	Wave number (m^{-1})
L	Lift (N)
L_{ux}	Integral length scale in the longitudinal direction (m)
m	Correction factor for Savomius turbine
M	Mesh size (m)
N	Number of samples
P	Power (W)
p	Pressure (Pa)
Q	Mechanical torque (Nm)
R	Turbine radius (m)
R^2	Coefficient of determination of a linear fit
Re	Reynolds number
S	Blade surface (m^2)
S	Slope of a linear fit
S_u	Autospectral density function for u.
t	Time (s)
T_u	Integral time scale in the longitudinal direction (s)
U	Longitudinal wind speed (m/s)
U_c	Blockage-corrected wind speed (m/s)
u	Longitudinal fluctuations of V (m/s)
v	Traversal fluctuations of V (m/s)
V	Total wind speed (m/s)
w	Vertical fluctuations of V (m/s)
w	Gap distance from the grid bars to the walls (m)
x	Distance (m)

Greek letters

α	Angle of attack ($^\circ$)
δ	Mesurement uncertainty
ϵ	Blockage ratio
λ	Tip-speed ratio
μ	Dynamic viscosity (Pa $\cdot$ s
ω	rotational speed (rad/s)
ρ	Density (Kg/m^3)
ρ_u	Autocorrelation of the u signal in the longitudinal direction
σ	Standard deviation
θ	Azymuthal angle ($^\circ$)

Sub- and superscripts

c	Chord-related
max	Maximum
$mean$	Mean
opt	Optimum opreation point
per	Phase-resolved
sys	Systematic
r	Random
$test$	Test section
$VAWT$	Of the turbine

Preface

Climate change is one of the major issues that humanity is facing in the XXI century, and transition into a more environmentally friendly energy system is mandatory in order to rise to that challenge. This is one of the main objectives in the European Union Horizon 2020 research and innovation program and its Renewable Energy Directive, that set rules for the EU to achieve its 20% share for renewable energy target by 2020 [H2020, 2018]. The European Innovative Training Network (ITN) AEOLUS4FUTURE is funded by the Horizon 2020 program with the goal of researching towards 'Efficient Harvesting of the Wind Energy'. Under this program 15 young students were recruited at 10 different European universities in order to research innovative aspects of wind harvesting [A4F, 2016].

The present work is framed in the Aeolus4Future Work Package 2: 'Wind turbine load analysis, control and simulation' that was led by the University of Florence. This thesis objective was to investigate and improve the performance of Vertical-Axis Wind Turbines (VAWTs) in urban environments. This technology is considered as a promising alternative to the conventional wind turbines (with horizontal axis of rotation) when harvesting wind energy inside the cities. Their omnidirectionality, low centre of gravity and lower rotating speeds are useful features to deal with the highly turbulent, inclined and stratified flows found in urban environments. The Aeolus4Future proposal suggested testing in the wind tunnel several models of VAWT, in order to gain knowledge in the topic and develop an optimized VAWT prototype [A4F, 2014]. This research could be of much interest to validate VAWT numerical codes that are being developed within the AEOLUS4FUTURE network and the whole wind energy community.

A research of the state-of-the art in urban VAWTs showed that most of these installations appear to deliver very poor energy yields, normally well below the predictions of the producers. This is mainly due to the immaturity of the technology and the lack of understanding of urban flows, which leads to many cases of bad design and installations and gives a very negative image of the technology. Due to that, it was decided to take a more detailed approach of the problem, focusing in concrete aspects of urban winds and their effect into VAWTs instead of a general but not that defined optimization.

Turbulence is one of the main features of urban flows. Its effect in building aerodynamics and bluff bodies has been studied by many institutions, among those the University of Florence. The goal of this thesis, therefore, was to put that expertise in the study of how turbulence affects urban VAWTs performance. This is an interesting niche in the urban wind market, as turbulence is supposed to play an important role in turbine performance and life span, but results from field measurements are not conclusive. This study tried to establish a benchmark to evaluate this influence, and aimed to provide valuable experimental data for turbine manufacturers and to validate computational models. In addition, the effect of turbulence, due to its random and unpredictable behaviour, is difficult to model by numerical simulations, so wind tunnel tests are not only interesting but also advisable in order to study this phenomenon.

The first months of the project were devoted to perform a literature survey in both urban winds and VAWTs. The state-of-the-art of this technology was critically analysed, as well as the turbine aerodynamics and the wind tunnel testing methodologies. All these topics are addressed in Chapter 1: *Background and related work*. Chapter 2: *Facilities and measurement equipment* lists the elements of the set-up used along the thesis: facilities, equipment, data analysis and corrections applied. During the first experimental campaign the turbulence generation procedure was adapted and optimized for the present case, focusing in modelling urban wind conditions and achieving uniformity of the flow, as exposed in Chapter 3: *Generation of turbulence in the wind tunnel with passive grids*. The second row of experiments were devoted to test a VAWT prototype under those turbulent conditions, to identify the effect of the various parameters of turbulence on its operation. Chapter 4: *Testing on the effect of turbulence on VAWT performance* relates the procedure of this tests, done in both VUB and CRIACIV wind tunnels for validation and to evaluate the effect of blockage. Chapter 5: *Measurement of a VAWT wake under turbulent flow* summarizes the measurement campaign studying how turbulence influences the wind turbine wake and the vibrations in its structure. The goal of the last part of the thesis was to explain the results encountered, and a set-up was developed to study the blade aerodynamics and how to simplify its optimization. This process is described in Chapter 6: *Aerofoil testing and characterization for urban VAWT*. Overall conclusions and future developments are presented at the end.

Chapter 1

Background and related work

1.1 Urban winds and its characteristics

1.1.1 The wind resource

Wind flows represent one of the major sources of renewable energy in the planet. According to The International Energy Agency (IEA), wind energy potential available in the world accounts for 167000TWh a year, which supposes a 107% of the total energy consumption of the planet [Veljkovic, 2016]. It is lower than the solar energy potential (440000TWh a year) but leads by far other renewable energy sources as geothermal (139000TWh a year) and hydroelectric power (14000TWh a year). This resource has been exploited by humanity for thousands of years.

The ancient Chinese were the first to use sails to move ships, around the year 3000BC [Tong, 2010]. The first windmills are said to have been built by King Hammurabi of Babylon, as early as the 17th Century B.C. There is written evidence of the use of wind energy to grind grain in Afghanistan in the 7th Century AD (Figure 1.1). Those ancient devices had a vertical axis, and could be also found in China in the 10th Century [Gasch, 2012]. In Europe, grain grinding mills arrived in the 12th century, but were built using a horizontal axis. These mills spread during the 13th century, becoming a common sight in the countryside of Spain, France or England [Mathew, 2006] (Figure 1.2). In Northern Europe, the most famous use of windmills was for pumping water in the Netherlands, that led to the popular US water pumping mill powered by a multi-bladed turbine. However, with the invention of the steam engine and the irruption of fossil fuels, the use of windmills was progressively abandoned.

Figure 1.1: Ancient windmills in Nashtifan, Iran [Ramin, 2012].

Figure 1.2: Windmills in Mota del Cuervo, Spain [Sucoplus, 2010].

The first windmills used to produce electricity date back in the late nineteenth century in USA (C. F. Brusch) and Denmark (P. La Cour) [Burton et al., 2001]. However, the Wind Turbine technology was rarely used during most of the 20th century, with the exception of isolated areas away from the electrical grid. It was the oil crisis in 1973 that awakened the world interest for wind energy. The uncontrollable rise in fossil fuel prices led some governments to start research programs to develop renewable energy technologies. Some examples of the first prototypes developed by those programs were the NASA 100kW Mod-0 turbine built in 1975 in the USA [Ragheb, 2013], the 230kW Darrieus turbine built in 1977 by the Canadian National Research Council [Templin and Rangi, 1983], or the 130kW Musgrove H-rotor developed in the UK (those last two Vertical Axis Wind Turbines or VAWTs). As it can be seen in Figures 1.3 to 1.5 the optimal configuration, type of blades, orientation and location of the equipment were still unclear. Those prototypes lacked reliability, their performance in difficult wind climates was poor and generally encountered major problems when being built in large scales. But they set the ground floor for the later development of wind turbines.

In the eighties the "Danish" wind turbine concept, developed by Johannes Juul in the 50s, was adopted by some Danish manufacturers of agricultural

Figure 1.3: NASA Mod-0 turbine built near Sanduski, USA [Brown, 2009]

Figure 1.4: Darrieus Wind Turbine installed in the Magdalen Islands, Canada [Public domain].

machines (Vestas, Bonus, Nordtank, etc.) [Burton et al., 2001]. It consisted in a three-bladed horizontal axis rotor mounted in a tower, and operating by stall control and at a fixed speed. This design showed great performance

Figure 1.5: VAWT-450 turbine built in 1986 in Reading, UK [Price, 2006]

in the range of 30 to 100 kW turbines, grew quickly in popularity and was adopted by the major wind turbine manufacturers, that built larger and larger machines, becoming what now is known as a conventional wind turbine (Figure 1.6).

Figure 1.6: 2.3MW Siemens wind turbines in the Norrekaer Enge wind farm, Denmark [Staunited, 2018].

The growing evidence of Climate change due to CO_2 emissions gave the definitive push to renewable energies and wind turbines in particular. In

1997, the European Union introduced a White Paper calling for a 12% penetration of renewable energy in its countries prior to 2010 [European Commission, 1997]. During the period 2000-2015 the installed wind energy capacity in the EU passed from around 12.8 GW to 141.5 GW, supposing an increase of around 9 GW annually and reaching the 15.6% of the EU power mix [EWEA, 2016]. Nowadays the Asian market, specially China, is taking over the impulse of wind energy with 30.7 GW installed in 2015. Apart of Asia and Europe, only North America is developing wind energy in their land (10.8 GW installed in 2015), while the technology still has to kick off in Latin America, Africa or Oceania (See Figure 1.7) [GWEC, 2015].

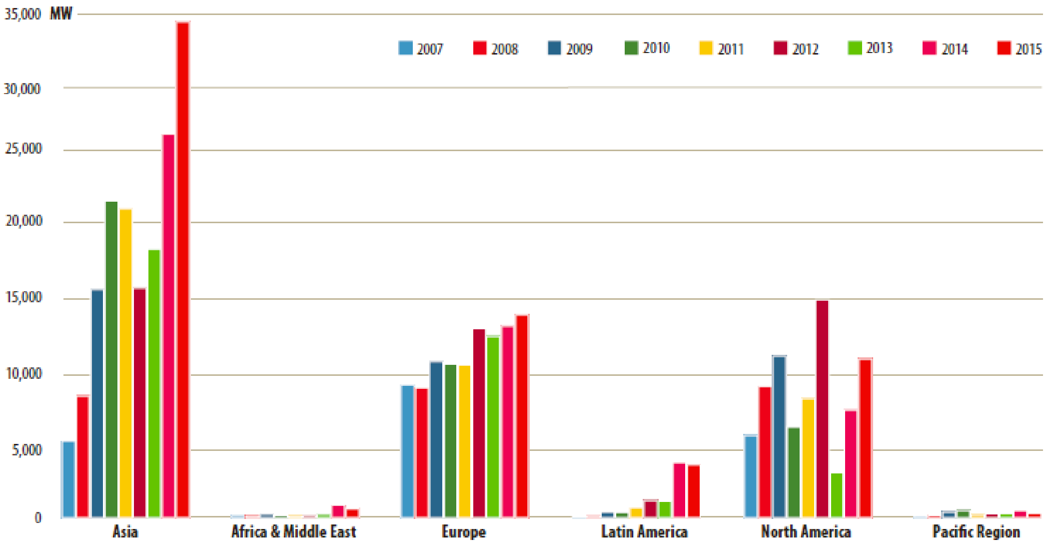

Source: GWEC

Figure 1.7: Annual installed capacity by region 2007-2015 [GWEC, 2015].

1.1.2 Wind in urban environments

United Nations identified city planning as a key aspect in order to face global warming. With half of the world population (and increasing) cities consume 75% of the world energy and generate 80% of greenhouse emissions [UN, 2007]. And while wind energy is becoming a factor in reducing greenhouse gases, only 0.2% of this wind energy is generated by small wind turbines as the ones present inside urban areas [WWEA, 2014]. Increasing that figure could help reducing this negative impact that cities have on the environment.

While it is clear that urban wind turbines, due to their limited size, will never reach the MW scale of the large offshore and open terrain models, their implementation has several positive aspects. First, they allow to consume the energy generated directly on-site, without the need of costly energy transport and electrical substations. They can be used as back-up generators in case of network problems or blackouts. And last but not least, they can increase the familiarization of the general public with wind energfy, especially for its promotion and study at schools and universities. However, harvesting winds in urban environments has proven to be more complicated than in open-terrain, and this fact is slowing down the development of urban wind technology. The immaturity of the technology and lack of knowledge on how to choose the right locations have led to multiple installations that under-perform or are directly still, resulting in bad press to wind energy [Gipe, 2013]. A first step, then, would be understanding the nature of winds inside built areas in order to achieve a successful implantation of urban wind turbines.

Several factors affect the atmospheric boundary layer (ABL) over the urban environments. On one side, tall buildings provide shape and frictional drag to the flow, which generates turbulence and low mean wind speeds. [Stathopoulos et al., 2018]. On the other side, human generated constructions and activities create what is known as the Urban Heat Island: the extra heat flux from buildings, refrigeration, lights and transport drives not only the temperature gradients but also the structure on the ABL [Barlow, 2014].

Three horizontal scales can be defined in the urban boundary layer (UBL):

- Scale 1-10 km: at city level advection is the key characteristic, and the size of the city defines the interaction between the UBL and the smoother rural ABL. If the city is large enough, the UBL replaces completely the rural ABL upstream [Barlow, 2014].

- Scale 100-1000 m: at neighbourhood level, the changes in roughness (from parks to suburbs to city centre) are the key factor, and determine the local ABL that will define the mean wind speeds present at the top of the buildings. This factor can be appreciated in Figure 1.8, which shows the mean wind speed in the Greater London area. It can be seen how higher wind speeds are reached in the outskirts, close to the undisturbed ABL, while in the city centre mean wind speed is lower due to taller and more dense buildings [Drew et al., 2013].

- Scale 10-100 m: at close proximity of buildings the flow is very complex, with large variability in the wind speed and direction over small distances [Mertens, 2006]. Closely spaced buildings create higher shape drag, directing flow over the top and forming eddies between them. The flow can also be channelled between them, with flow acceleration near the ground level (street canyon). This effect, though, is heavily influenced by the roadside trees, that reduce significantly the wind speed [Stathopoulos et al., 2018]. At this scale, wind gusts also play an important role, which can cause unexpected loads on the turbine elements. Figure 1.9 shows a schematic representation of the UBL near the surface.

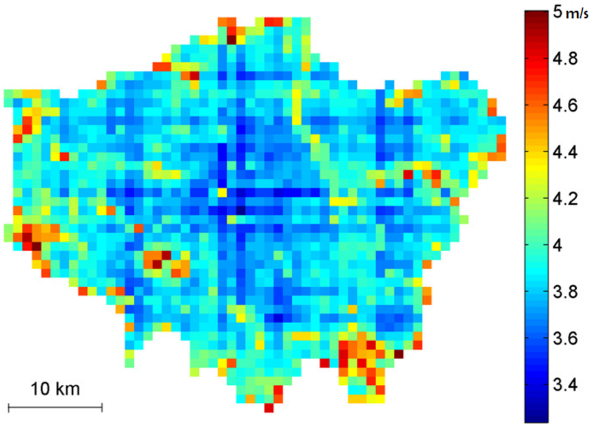

Figure 1.8: The annual mean wind speed, at building hub in the Greater London area [Drew et al., 2013].

In conclusion, the flow in urban environments is more complex and presents lower mean speeds as the wind found in the rural areas. However, here the objective is to harvest the maximum energy from the wind, therefore it is the opposite to the traditional wind engineering approach, where the focus would be to reduce wind speed in order to minimize the loads in the buildings and increase the pedestrian comfort [Stathopoulos et al., 2018]. Figure 1.10 shows that the wind resource decreases towards the centre of the city, but the standard deviation shows that individual sites can perform even

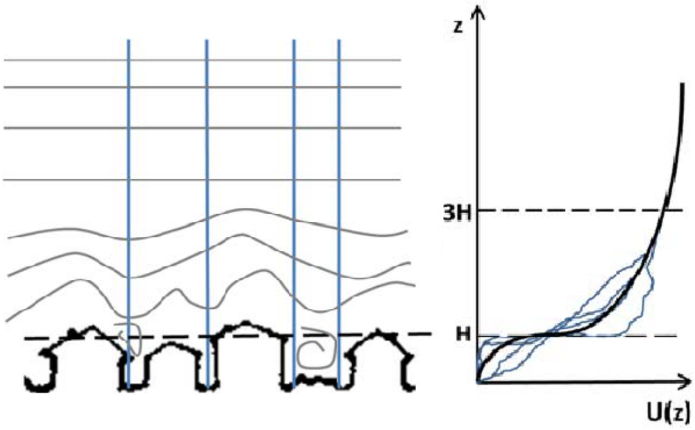

Figure 1.9: Schematic representation of the flow over an urban area, and graph of the spatially averaged flow, where H is the mean building height [Barlow, 2014].

better than rural sites up-stream. Those precise spots (parks, rivers, coastal urban areas, sub-urban sites, tall buildings) is where urban wind turbines could be economically viable [Barlow, 2014]. And therefore a deep understanding and modelling of the complete UBL to identify those locations is needed before any urban wind turbine is installed.

1.1.3 Modelling and simulation of urban conditions

Several methods are used for the assessment of the urban wind potential in the building scale, where urban wind turbines energy yield, wind loads and pedestrian comfort are of interest:

- Onsite measurements may not be necessary for small wind turbines (SWTs) exposed to prevailing winds in rural areas, but in urban environments field measurements are compulsory in order to understand all the particularities of the flow [Anup et al., 2019]. Those measurements are very time-consuming and expensive, and doing them for every installation would suppose a large obstacle in the economic viability of this technology, especially in the case where SWT have to be integrated in the building design [Stathopoulos et al., 2018].
- Numerical simulations with Computational Fluid Dynamics (CFD) have become a common practice to evaluate the wind resource in ur-

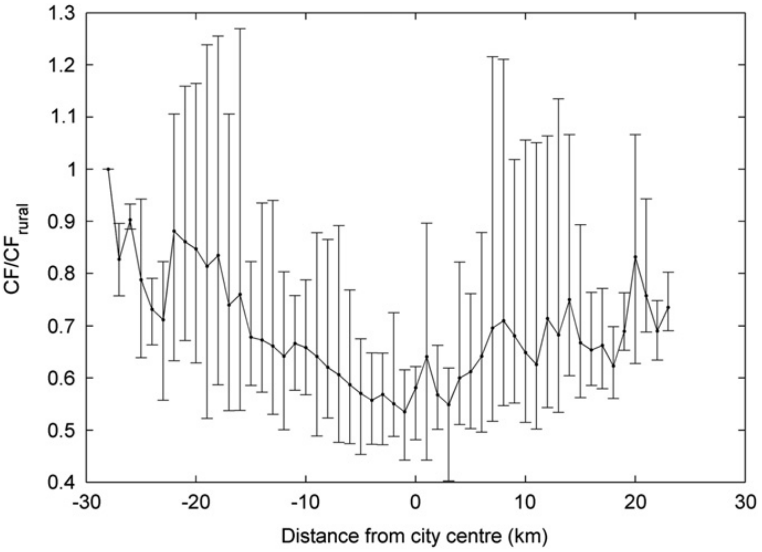

Figure 1.10: Mean capacityfactor of 34 turbines estimated at z_{hub} averaged along 15 transects through Greater London. The values have been normalised by the mean capacity factor at the rural site at the start of each transect [Drew et al., 2013].

ban environments, but they also require significant computational time and validation period. Advanced modelling like Large Eddy Simulation (LES) has been applied at this scale for the study of pollutant dispersion [Barlow, 2014], but it is still too costly for the reduced margins in which SWT moves [Anup et al., 2019].

- A simpler approach is to use probabilistic mathematical functions such as Weibull or Rayleigh adapted to the Urban boundary layer, and combining it with wind atlas data and close meteorological stations [Stathopoulos et al., 2018]. These logarithmic wind profiles show similarity with the results from rural areas, only the turbulence intensity is higher in the urban cases [Roth, 1999]. However, this approach is not precise enough for detailed yield predictions.
- Replicating inside the wind tunnel those logarithmic profiles allow to measure wind speeds and pressure distributions around scaled versions of the urban environments. This technique, which requires a boundary layer wind tunnel and turbulence generation devices as grids, spikes, barriers or cups (Figure 1.11) allows not only getting direct measure-

ments of non-dimensional quantities but also provides valuable data to validate CFD codes.

Figure 1.11: Grid, barrier and cups placed in the VKI L-1B wind tunnel in order to generate the desired wind profiles.

The previous cases are designed for the neutral boundary layer, but the approach gets even more complicated if the objective is to reproduce the nocturnal urban boundary layer. Its formation depends on several factors: low winds would generate buoyant winds over the cities, while orography can highly influence urban winds with down-slope flows, sea breezes and other phenomena [Barlow, 2014].

1.1.4 Description and importance of turbulence

High turbulence is one of the most characteristic features of urban flows. Turbulence is said to exert a considerable effect in turbine operation: increase of fatigue, unpredictability of energy production or influence on stall conditions [Paraschivoiu, 2002]. Turbulence I_u is a directional parameter defined as a measure of longitudinal fluctuations u of the wind speed of a flow with longitudinal mean wind speed U [Burton et al., 2001], and it is indicated in % (Eq. 1.1). The transversal components of the wind, being of low intensity compared to U, are not considered in this study.

$$I_u = \frac{\sigma_u}{U_{mean}} \tag{1.1}$$

Also meaningful for the description of a turbulent flow is the integral length scale, seen as the size of the most energetic turbulent eddies of the flow [Bearman and Morel, 1983]. This directional quantity (represented L_{ux} in the flow direction) can be calculated using the autocorrelation function (Eq. 1.2) upon a time sample T, that describes how much a measurement of a turbulence component $u(t)$ is related to the value of the same component at a consecutive time instant $t + \tau$, which defines the integral time scale T_u (Eq. 1.3, [Tavoularis, 2002]).

$$\rho_u(\tau) = \lim_{T\to\infty} \frac{1}{T} \int_0^T [u(t)] \cdot [u(t+\tau)]\, dt \tag{1.2}$$

$$T_u = \int \frac{\rho_u(\tau)}{\sigma_u^2} d\tau \tag{1.3}$$

In this case, and assuming Taylor's frozen-eddy hypothesis (the vortices are passing with mean velocity U_{mean}), the longitudinal integral length scale of u is:

$$L_{ux} = T_u U_{mean} \tag{1.4}$$

The results were confirmed by fitting the measured spectrum to a von Kármán spectrum (Eq.1.5) , that offers a good representation of turbulence inside wind tunnels [Burton et al., 2001].

$$\frac{fS_u}{\sigma_u^2} = \frac{4fL_{ux}/U_{mean}}{(1 + 70.8(fL_{ux}/U_{mean})^2)^{5/6}} \tag{1.5}$$

where f is frequency and S_u is the autospectral density function for the longitudinal component.

From the description of an unidirectional flow with 3D turbulence [Olivari and Benocci, 2013], it can be argued that turbulent flow is more energetic due to the fact that the variable components of the flow u, v and w (Eq. 1.6) add up to the power available by the law of the cube (Eq. 1.7) [Möllerström et al., 2016]

$$|V| = \sqrt{(U+u)^2 + v^2 + w^2} \tag{1.6}$$

$$P_{av} = \frac{1}{2}\rho A V^3 \tag{1.7}$$

It is not clear, though, if turbines are able to harvest this extra power, or, if on the other hand, fatigue and aerodynamic disturbances weight too much against operating in turbulent conditions. In HAWTs (Horizontal-Axis Wind Turbines), it is generally searched not to operate in turbulent flows to avoid the turbine being in yaw state [Lubitz, 2014], a fact that does not apply on VAWT. The study of turbulence effect on VAWTs is up to nowadays generally limited to on-field data obtained by comparing the performance of the installed turbines and the on-site wind turbulence measured by a meteorological station. These studies offer often unreliable and contradictory conclusions, as the effect of turbulence is said to be positive [Möllerström et al., 2016, Bertényi et al., 2010], negative [Pagnini et al., 2015, Kooiman and Tullis, 2015] or velocity-dependent [Lee et al., 2018]. The impossibility to control all external conditions and influences in a real urban environment suggests that wind tunnel measurements might be necessary in order to obtain precise and repeatable turbine power curves under the influence of different turbulence levels.

Since 2013, the International Energy Agency (IEA) Wind Task 27: *Small wind turbines in high turbulence sites* has been documenting the research activities related to understand how turbulence impacts small wind turbine production [IEA, 2018].

1.2 Vertical-Axis Wind Turbines (VAWTs)

1.2.1 VAWTs characteristics and applications

As it was explained in the previous section, the "Danish" Horizontal Axis Wind Turbine has been the most successful design so far. However, during last years the research in Vertical Axis Wind Turbines has re-emerged, in an attempt of overcoming the main drawbacks of the HAWTs technology: inaccessibility to the electrical equipment placed in the nacelle and adaptability to unstable winds. Traditionally, VAWT designs, especially Savonius, had been discarded by their lower efficiency compared with the horizontal axis rotors, even though recent research suggests that this is not necessarily true for Darrieus [Paraschivoiu et al., 2017]. This efficiency is generally expressed as the Power coefficient (Eq. 1.8), which is the ratio between the power extracted by the turbine and the available power in the wind. In most of the turbine ratings, the x axis of the graph is the tip-speed-ratio (λ, Eq. 1.9), an indication of the rotational speed of the turbine. Figure 1.12 presents examples of power curves for different types of turbines.

$$C_P = \frac{P_{VAWT}}{P_{av}} = \frac{P_{VAWT}}{\frac{1}{2}\rho A_{VAWT} U^3} \tag{1.8}$$

$$\lambda = \frac{\omega R}{U} \tag{1.9}$$

where ρ is the air density, A_{VAWT} the frontal swept area of the VAWT, U the wind speed, ω is the rotational speed and R the turbine radius.

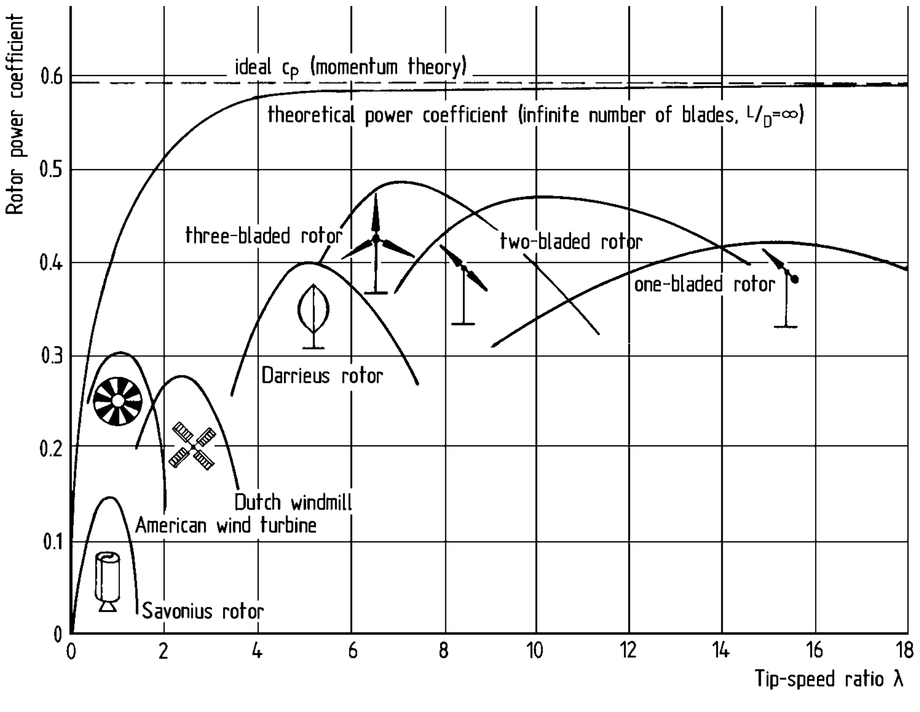

Figure 1.12: Power coefficient curves for rotors of different kind [Hau, 2006].

VAWTs, however, possess some qualities that may give them some advantage over conventional "Danish" wind turbines in special applications. Table 1.1 summarizes the advantages and inconveniences of each of the two technologies [Paraschivoiu, 2002].

Vertical Axis Wind Turbines	**Horizontal Axis Wind Turbines**
Advantages	
• Non-directional, can collect wind from any direction. • Gearbox and inverter located on the ground. • Good response to turbulent winds. • Less dangerous to birds and bats. • Low rotational speeds, therefore low noise. • Stable structure.	• Higher efficiency. • Established and socially accepted technology.
Drawbacks	
• Lower efficiency. • Technology still in the development phase. • Little known to the general public. • Generally needs the installation of guided wires.	• Directional, difficulties to collect changing winds. • Bad reaction to turbulence. • Electric equipment located up the tower, difficult to repair or check. • Huge torsional efforts on the tower structure. • Turning at high speeds can cause annoying noise for the neighbours.

Table 1.1: Advantages and drawbacks of VAWT and HAWT.

Generally speaking, the two advantages of HAWTs (higher efficiency and reliability) are definitive for any wind power installation. However, two situations have been identified where HAWTs have important operational problems that could be solved by VAWT technology:

1. Urban Wind Energy: Urban wind flows are normally low-speed, changing and turbulent, three conditions in which conventional wind turbines operate poorly. Furthermore, noise is a critical matter in populated areas, and in this case also VAWTs operate better. Several companies are already commercializing VAWTs for this use, and the technology, even not yet established, is improving at a good rate. In the following chapters this application will be analysed in detail.

2. Floating platforms off-shore wind turbines: In the locations where the sea floor does not allow building foundations, off-shore wind turbines must be placed in a floating platform. The complex structural dynamics of HAWTs can suppose an inconvenient to this purpose. VAWTs, with scalable and robust structures, simpler installation and lower centre of gravity, could adapt better to floating platforms [Euromech, 2016]. This technology, however, is in the earliest steps of design, and will not be analysed in this project.

As shown in previous chapters, VAWTs played an important role in wind energy history. The first prototypes, as the Cap Chat in Canada or the Sandia in the USA reached considerable sizes and rated power. But since then, the trend has been to design them mostly in the small scale, to take advantage of the strong points of the technology. Table 1.2 enumerates the main characteristics of some of the most significant VAWT models built.

As it can be seen in the table, there exist several operative designs for VAWTs. Unlike with HAWTs, it is not yet clear which configuration is better, existing successes, and specially failures, for each design.

	Year installed	Type	Diameter (m)	Height (m)	Swept Area (m^2)	Rated power (kW)
Eole C, Cape Chat (Canada)	1987	Darrieus	64	96	4096	4200
SANDIA Test Bed (USA) [Sutherland et al., 2012]	1988	Darrieus	34	42.5	963	500
VAWT-450 (UK)	1986	Musgrove	25	25	625	130
VAWT-850 (UK)	1990	H-rotor	38	45	1710	500
Flowind EHD (USA)	1985	Darrieus	18	48.5	582	300
Ropatec TS30 (Italy) [Ropatec, 2013]	2013	H-rotor	10	10	100	30
Windside WS-12 (Finland) [Windside, 2009]	2001	Savonius	2	6	12	5

Table 1.2: Characteristics of some VAWT prototypes.

1.2.2 Design and characteristics of current VAWTs

Savonius

The simplest of the designs, it is a drag-based device patented by Savonius in 1925 but appeared centuries ago [Savonius, 1925]. It is similar to cut a barrel in two halves and fix them together or to the working principle of a cup anemometer (figure 1.13). Its main advantages are simplicity and its high starting torque, meaning they are self-starting. The drawback of this technology is its low efficiency ($< 30\%$) and that their low rotating speed make them unable to be used in electricity production. Only one company operates successfully an helical version of this design (Windside, Finland, figure 1.14 [Windside, 2009]), while others as HelixWind exploited the concept for several years but ended in commercial failure [Clark, 2012]. Due to their poor electricity generation ability, Savonius turbines are not studied in this thesis.

Figure 1.13: Typical Savonius rotor [bobmcgov, 2016].

Figure 1.14: Turbines WS-4B from Windside [Windside, 2009].

Darrieus

Invented by the French engineer Georges Jean Marie Darrieus in 1931, is a lift-based machine, which allows higher efficiencies than the Savonius [Darrieus, 1931]. That feature turned the Darrieus into the main hope for VAWTs in the 70s, with the development of prototypes that reached rated powers of MW. The main research was conducted by the Canadian National Research Council (Magdalen Islands, Cap Chat) and the Sandia National Laboratories in the USA [Templin and Rangi, 1983, Sutherland et al., 2012]. Some companies commercialized Darrieus turbines in the past, as FloWind, that used Sandia's research for building the largest VAWT farm ever in the Tehachapi Pass in California (95 MW installed from 1986 until 1997 [Gipe, 2013]). However, their complexity (there are multiple possible variations of the design), high loads in the rotor bearings, and the rise of the 'Danish' HAWT concept made them unsuccessful.

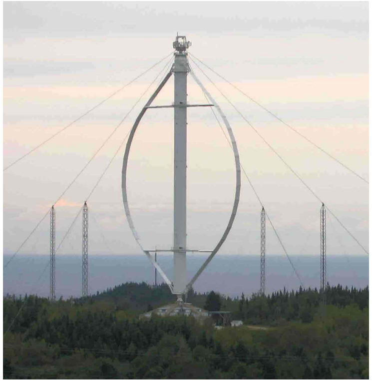

Figure 1.15: The 4.2MW Darrieus turbine in Cap Chat, Canada [Pierre5018, 2012].

Figure 1.16: FloWind wind farm in Tehachapi Pass, in the early 1990s [Gipe, 2013].

All the most recent VAWT designs evolved from the Darrieus lift-based concept. An interesting design has been proposed by the Taiwanese company Hi-VAWT, incorporating a Savonius rotor to obtain the starting torque for a Darrieus. This company started operations in 2005 and has successfully spread its operation across the globe [Hi-VAWT, 2012]. In 2008 the Canadian engineer Glen Lux proposed a design that removed the tower from the Darrieus turbine, allowing like this to reduce costs drastically. Still in the certification phase, was awarded with the *Create the Future Design Contest* by the *NASA Tech Briefs* magazine in 2013 [Lux, 2015].

Figure 1.17: 3KW wind turbine from Hi-VAWT built in China [Hi-VAWT, 2012].

Figure 1.18: Prototype from the company Lux Turbines [Lux, 2015].

H-rotor

In his 1931 patent Darrieus also proposed a lift-based device with straight blades to reduce its complexity [Darrieus, 1931]. This design is also called gyromill and it is one of the most used evolutions of the Darrieus design. When the blades possess pitch-changing devices, the system is called cycloturbine. During the seventies and eighties, several prototypes of H-rotor up to 500KW were built in Wales, UK [Price, 2006]. However, as with the rest of VAWTs, the trend evolved to smaller turbines until present time. The Danish company Aeolos commercialises since 1997 different models of VAWT to complement their HAWT offer [Aeolos, 2015]. Ropatec, in Italy, is another successful gyromill producer; they have sold more than 1000 turbines since 2001, and installed the only VAWT farm in Europe near Volterra, in the province of Pisa [Ropatec, 2013]. A variation of the H-rotor but more slender that had caused great impact in the wind energy community is the Windspire produced in the USA since 2005 [Wire, 2009].

Musgrove

During the seventies, and within the UK large-scale wind research program, the British engineer Peter Musgrove proposed a variation of the H-rotor, that integrated a reefing system which automatically feathered the blades in strong winds to avoid over-speeding. A 130KW turbine was built in 1986 and tested successfully during some years (see figure 1.5). However, those tests

Figure 1.19: Ropatec TS30 wind farm near Volterra, Italy [Ropatec, 2013].

Figure 1.20: Two 1.2KW Windspires [Wire, 2009].

showed that the reefing system was unnecessarily complex (as power control was automatically achieved by the natural passive-stalling of the aerofoils, even in strong winds with the blades remaining vertical) [Price, 2006].

Helical blades

An H-rotor with helically-twisted blades is known as Gorlov turbine due to its inventor, who designed it for water streams in 2001. Even considering the production difficulties for the curved blades, this design provides important results in uniformity of torque and acoustic emissions, having been adapted for wind applications [Battisti, 2012]. The University of Delft developed one of the first models, called Turby, in 2004, reaching 1KW of rated power [Turby, 2005]. Nowadays is one the most popular designs for small VAWT manufacturers, with companies as UGE producing it at commercial scale. Probably the main feature of this design is its futurist aesthetics, which makes it very attractive for urban environments, as the QuietRevolution QR5 that was built next to the London Olympic Stadium.

With the climate change and the need of renewable energy as a fact, a large number of research projects are being funded in the last years to study this technology, and a considerable number of companies are blooming in the field of producing small VAWTs. Figure 1.23 shows the comparison of the measured efficiency charts for some VAWT prototypes, compared with examples of commercial HAWTs.

Figure 1.21: Turby Prototype from the University of Delft [Turby, 2005].

Figure 1.22: UGE Visionair 3 (1KW rated power) in a roof in Brazil [UGE, 2016].

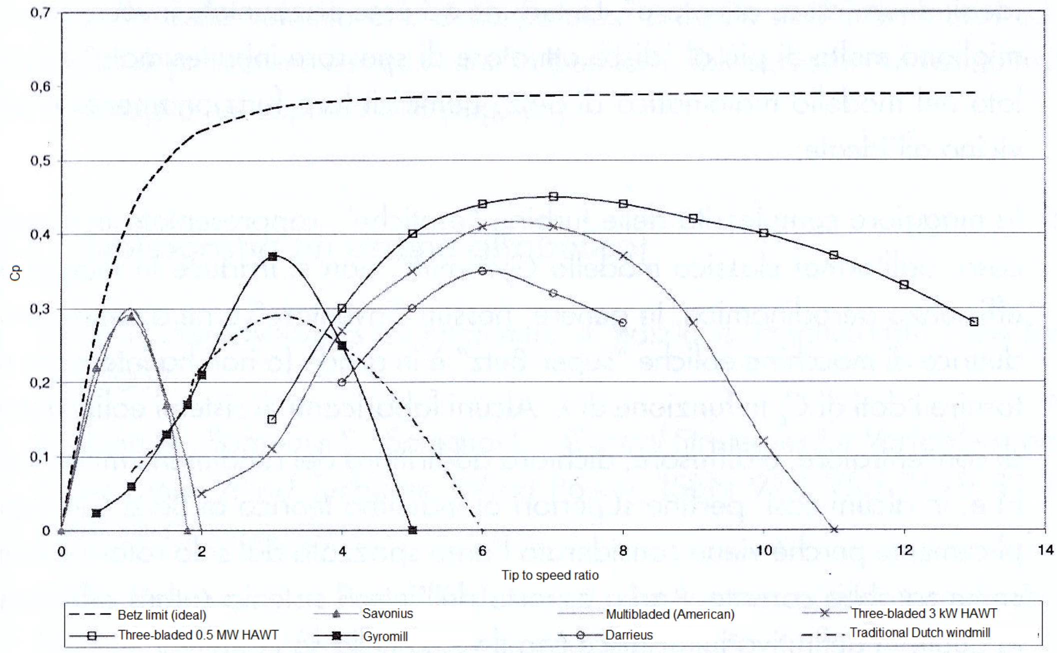

Figure 1.23: C_P curves comparison for various wind turbine designs [Rosato, 2015].

1.2.3 Wind tunnel testing of VAWTs

The first studies of VAWTs in the wind tunnel date to the end of the 1970s in the SANDIA research project [Blackwell et al., 1977]. The performance of a 2 m Darrieus VAWT measured in a 4.6 x 6.1 m wind tunnel was successfully compared with field tests [Sheldahl, 1981]. No turbulence or blockage effects were considered in that study. After the SANDIA VAWT project was closed, few more research was done in VAWT wind tunnel testing, mainly at the University of Montreal: there were done the first studies of the wake of a VAWT [Brochier et al., 1986] or the first attempt to model the influence of turbulence [Brahimi, 1970]. During the 1990s, some wind tunnel research was also carried out in Australia into VAWTs with variable pitching blades [Kirke and Lazauskas, 1993].

The 2000s saw the rebirth of VAWT technology for its applicability to urban environments. Delft University started testing the influence of skewed flows [Mertens and Bussel, 2003], and soon researchers from all over the world followed [Howell et al., 2010, Battisti et al., 2016]. Special interest has been paid in the study of VAWT wakes after a study from Caltech suggested a potential increase of energy density for VAWT farms [Dabiri, 2011]. Further research has increased the knowledge about the aerodynamic complexity of these structures and how to promote faster wake recovery [Tescione et al., 2014, Araya et al., 2017].

Wind tunnel tests onto the influence of turbulence in VAWTs have only been done in the last years. Miau measured a slight increase of power from for a 5-bladed Darrieus turbine [Miau, 2012]. Peng measured the influence of turbulence in the wake of the VAWT [Peng and Lam, 2016]. Ahmadi-Baloutaki performed full range of experiments regarding interaction between turbulent flows and a H-Darrieus, and although he detected a huge increase of power delivered, could not retrieve the complete power curves [Ahmadi-baloutaki et al., 2015].

1.3 Working principle of H-Darrieus VAWTs

1.3.1 Blade aerodynamics of H-Darrieus VAWT

Among the variety of VAWT designs, H-Darrieus turbines have especially attracted the attention of researchers, due to their higher efficiency and simple geometry [Aslam Bhutta et al., 2012]. Those turbines (Figure 1.19) are composed of a shaft, struts and straight blades (typically 2 to 5). Shaft and struts are designed to create as less drag as possible while maintaining structural properties, so the blades are the main feature that allows extracting energy from the wind. With this goal, the aerodynamics of an H-Darrieus VAWT aerofoil must be studied in detail. The complication resides in that during the rotation around the turbine shaft, the blade withstands variable conditions of wind speed and angle of attack (α), which at the same time carry with them large changes in the aerodynamic forces and torque generated. Figure 1.24 shows the relative velocity and aerodynamic forces suffered by a blade element in different positions along a rotation [Paraschivoiu, 2002].

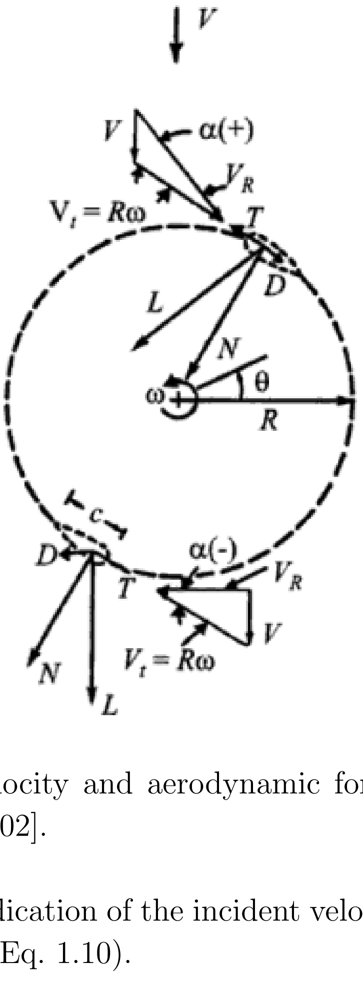

Figure 1.24: Relative velocity and aerodynamic forces for a typical blade element [Paraschivoiu, 2002].

A non-dimensional indication of the incident velocity can be given by the chord Reynolds number (Eq. 1.10).

$$\mathrm{Re}_c = \frac{\rho U_b c}{\mu} \tag{1.10}$$

where ρ is the air density, U_b the wind speed seen by the blade, c the blade chord and μ the air dynamic viscosity.

Two other non-dimensional coefficients need to be defined to describe blade aerodynamics, the lift coefficient 1.11 and the drag coefficient 1.12, that are dependent of α and in 3D flow are normalized with the blade surface S.

$$C_L = \frac{L}{\frac{1}{2}\rho S U_b^2} \tag{1.11}$$

$$C_D = \frac{D}{\frac{1}{2}\rho S U_b^2} \tag{1.12}$$

Figures 1.25 and 1.26 show the typical evolution of Re_c and α along the blade rotation. It can be seen how at $\theta = 0^\circ$ the blade, facing the flow, reaches the maximum Reynolds number but the effective α would be 0°. Minimum Re_c is obtained at the opposite side of the rotation, while during the rest of the rotation the wind incises the blade with a varying angle of attack. Specially at low λ the blade can enter stall conditions in some part of the rotation (see fig. 1.26). This fact, that depends on several factors (θ, Re_c, I_u, λ or the aerofoil shape), constitutes one of the main challenges in the operation of VAWTs.

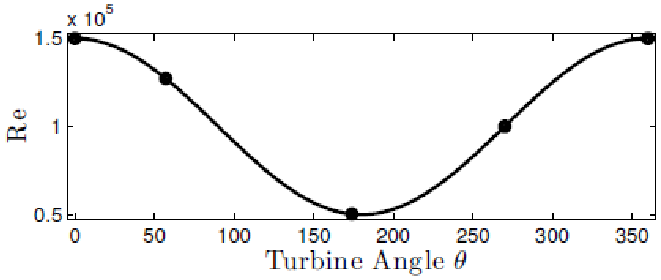

Figure 1.25: Incoming Re_c perceived by a NACA0018 blade along a rotation [Dunne, 2016].

1.3.2 Turbulence and stall

The impact of turbulent flows in the stall of the blades is a key aspect for the operation of urban wind turbines [Paraschivoiu, 2002]. Hoffman in 1991

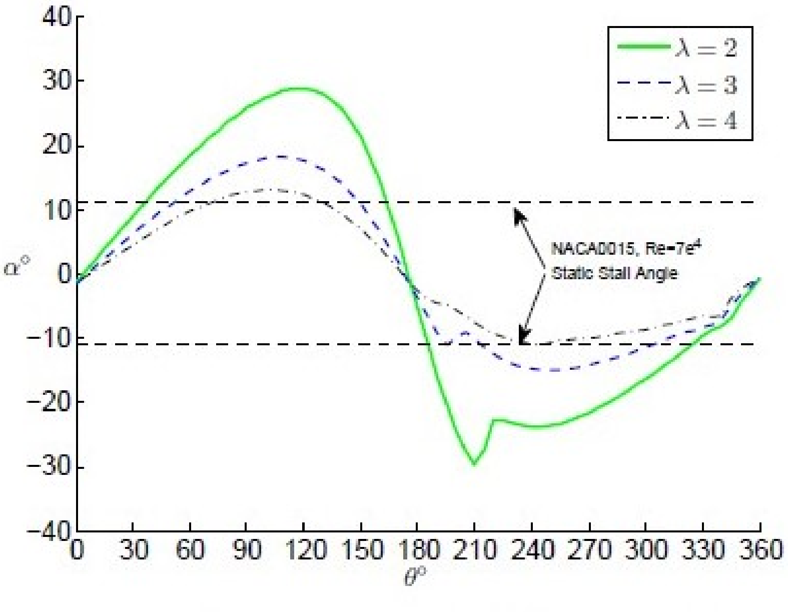

Figure 1.26: Plot of α perceived by the blade for $\lambda = 2$, 3 and 4, plotted in comparison to the static stall angle of a NACA0015 blade at similar Re_c [Ferreira, 2009a].

already detected a positive influence of turbulence in the lift of a symmetric NACA0015 aerofoil [Hoffmann, 1991]. Then the subject has been studied in detail for non-symmetrical HAWT aerofoils, always resulting in a very positive influence of turbulence on the stall of the aerofoils [Devinant et al., 2002, Amandolèse and Széchényi, 2004]. In Figure 1.27 it can be seen how the increase of turbulence from $I_u = 1.1\%$ to $I_u = 7.5\%$ not only raises the lift coefficient of the blade but also delays the stall angle.

However, when talking about VAWTs characterizing the static stall is not enough, as the variation of the angle of attack occurs at high rates, resulting in what is known as dynamic stall. This phenomena is characterized by the shedding and passage over the upper surface of the blade of a vortex-like disturbance [McCroskey, 1981]. The effect it has is an effective modification of the blade polar curves, defined by three parameters:

– frequency of oscillations, normally represented by the reduced frequency k (Eq. 1.13):

$$k = \frac{\omega c}{2U_b} \tag{1.13}$$

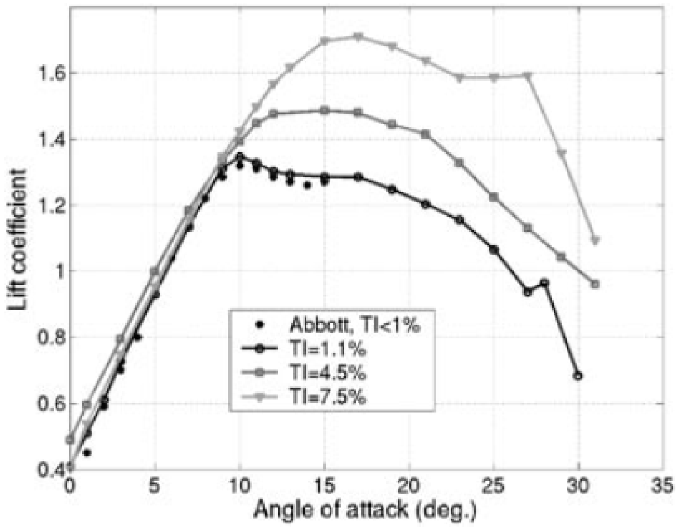

Figure 1.27: Effect of turbulence I_u in the lift coefficient C_L curves of a NACA 63_4_421 aerofoil, $\mathrm{Re}_c = 10^6$. [Amandolèse and Széchényi, 2004]

– mean angle α_0.

– amplitude of the movement α_1.

As seen in Fig. 1.28, also from [Amandolèse and Széchényi, 2004], dynamic stall boosts the maximum C_L and stall angle during the positive movement of the blade, while after stall the C_L value drops much more suddenly than in the static case, taking longer to return to the "original" values. That image also shows how this hysteresis is less pronounced when increasing the incoming turbulence.

This causes that in the areas where Re_c is low, and α high (see Fig. 1.25 and 1.26), the blade would go through a dynamic stall process as described in Fig. 1.29. Flow can be separated as early as $\theta = 100\,^\circ$, which constitutes a large loss of power in the upwind part of the rotation, where most of the energy is produced [Rezaeiha et al., 2018], with the extra difficulty of the recovery from the dynamic stall, which is slower than what the static curves indicate. Being able to reduce this separated flow zone should be one of the objectives of VAWT design.

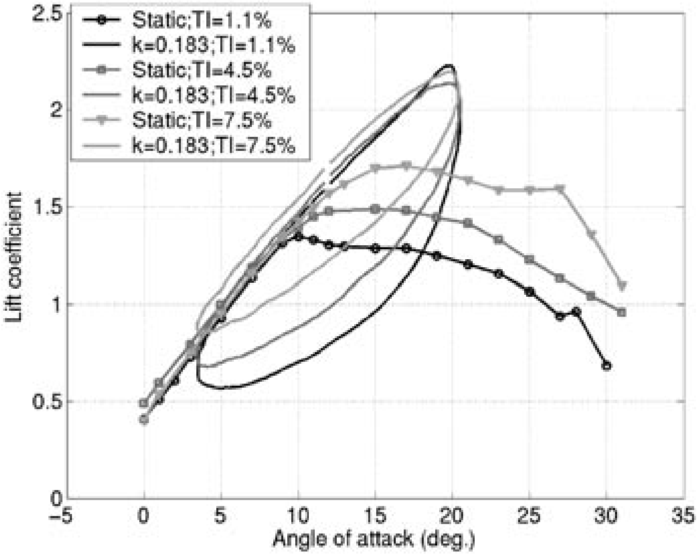

Figure 1.28: Influence of the turbulence level on the lift coefficient; a_0 =12 ° , a_1 = 8 ° , k = 0.183. NACA 63_4-421 aerofoil, $\mathrm{Re}_c = 10^6$. [Amandolèse and Széchényi, 2004]

1.3.3 Modelling and simulation of VAWTs from aerodynamic data

Extrapolation of airfoil polars into the turbine overall performance can be done through numerical modelling. Several numerical methods have been developed in order to predict the performance of VAWTs. The Single Stream-Tube model (SST) was developed by Templin in 1983. This 2D simple model extrapolates the aerodynamic coefficients of the blades into the aerodynamic forces on the whole curved-bladed Darrieus [Templin, 1974]. It is based in the actuator disk theory, assuming the induced velocity is constant along a streamtube crossing the diameter of the turbine. Fig. 1.30 shows its adaptation for a H-rotor, where all the sections have the same radius [Biadgo and Simonovic, 2012]

The code delivers reasonable results given its simplicity, although it fails to describe accurately the stall region and does not consider dynamic stall. Paraschivoiu described several of those more elaborated models, including the Multiple Streamtubes, vortex models, Double-Multiple Stream-

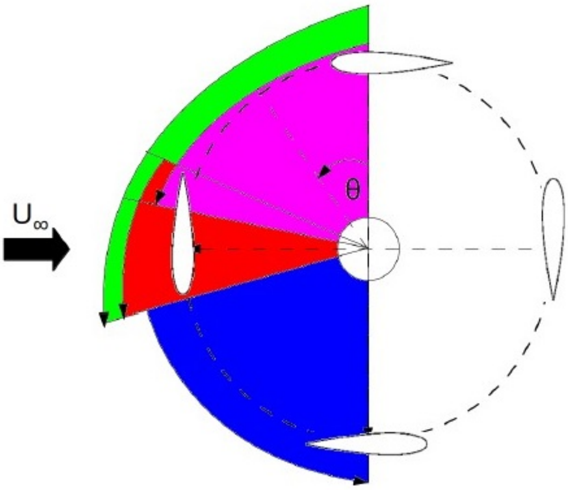

Figure 1.29: Dynamic stall regimes in the upwind part of the rotation. Dynamic stall development (green), trailing edge vortex shedding (magenta), leading edge vortex development (red) and separated flow (blue) [Dunne, 2016].

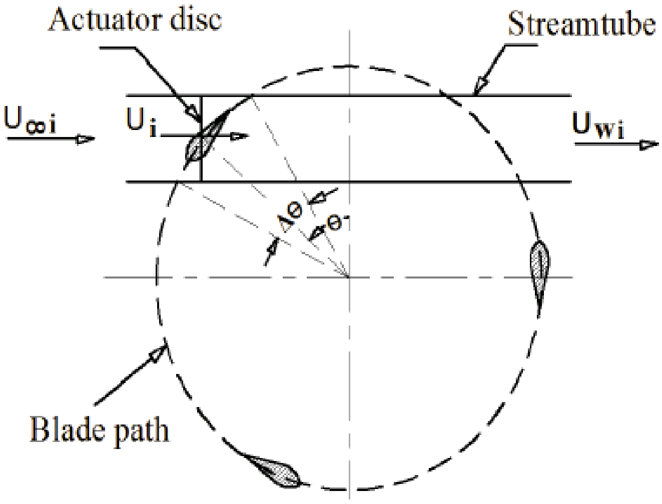

Figure 1.30: 2D schematic of the streamtube model [Biadgo and Simonovic, 2012]

tube and Dynamic-Stall modelling, and compared them to experimental data [Paraschivoiu, 2002]. Simão Ferreira compared some of those models on a test case featuring a 2-bladed H-Darrieus, concluding that the streamtube models are inaccurate in comparison with other methodologies as panel methods, actuator cylinder or vortex models [Ferreira et al., 2014].

In addition, dedicated numerical simulations using computational fluid dynamics (CFD) can also be carried out. This kind of simulations, if the proper levels of spatial and temporal refinement are provided [Balduzzi et al., 2016], recently showed to be able to accurately reproduce the aerodynamics of Darrieus blades [Bianchini et al., 2017a]. The computed flow fields allowed the identification of the main aerodynamic phenomena and flow macro-structures.

1.4 Research gap

The exploitation of small wind turbines for the urban environment is nowadays limited due to the complexity and multiple factors affecting urban winds, and therefore a thorough study of the UBL is necessary. Understanding the high turbulence present in the lower layers of the urban boundary layer, at building scale, and its effect into small VAWTs would increase its possibilities.

This technology, thanks to their omnidirectionality, low noise and aesthetic appearance, has emerged during the last decade as an alternative to conventional wind turbines to exploit the wind resource in urban environments. VAWT technology is still in the design phase, and several concepts and companies are trying to gain a share in the small wind turbine market. Among those designs, H-Darrieus, being efficient and simple, has proven the most promising according to the scientific community.

Its performance in skewed flows (another feature of urban winds) have been proven numerically and experimentally [Ferreira, 2009b], but there is not yet a conclusive study about the effect of turbulence on a H-Darrieus VAWT. Field studies do not show up to the moment conclusive results, and therefore testing in a controlled environment inside a wind tunnel is the chosen way of studying this effect.

The main goal of the study is, therefore, generating inside a wind tunnel urban-like turbulent conditions, and testing a H-Darrieus model to determine how turbulence intensity and integral length scale affect its performance.

And in order to go more in detail into the aerodynamics of the turbine, focus will be put in the individual effect of turbulence in the turbine blades, and how the choice in the aerofoil can improve the overall performance.

This thesis wants to set a reference in the way of evaluating the effect of turbulence in small wind turbines. Furthermore, the experimental data obtained of the full turbine and the individual blade can become very useful for validation of CFD and numerical codes, in order to expand the reach of this research.

Chapter 2

Facilities and measurement equipment

2.1 The facilities

During this study it was possible to perform wind tunnel testing in 3 different facilities. This was a huge opportunity as it allowed to compare and validate the results and methodology and evaluate the effect of blockage. All of them are of the Boundary Layer type, allowing the creation of the desired turbulence conditions upstream, but of different dimensions and characteristics. For more information about the wind tunnels refer the annex A.1.1.

2.1.1 CRIACIV wind tunnel

CRIACIV is an Inter-University Research Centre focused on the field of Building Aerodynamics and Wind Engineering, grouping eight Italian Universities. The Wind Engineering Laboratory is located in Prato, close to Florence, and it hosts an open-circuit boundary layer wind tunnel (Figure 2.1). The tunnel has a total length of about 22 m, including a nozzle at the inlet with a contraction ratio of 4.2 after the honeycomb and a T-diffuser at the outlet. The rectangular test section is 2.42 m wide and 1.60 m high. Air is aspired through a motor with a nominal power of 156 kW and the flow speed can be varied continuously up to 30 m/s adjusting, by means of an inverter, the rotational speed of the fan and the pitch angle of its ten blades. In absence of turbulence generating devices, the free-stream turbulence intensity is around 0.7%.

Figure 2.1: View of the CRIACIV wind tunnel with a turbulence grid installed.

2.1.2 VUB wind tunnel

The wind tunnel of the FLOW (Fluid Dynamic and Thermodynamics) research group is part of the Vrije Universiteit Brussel, in Belgium. The boundary layer wind tunnel has a length of 11 m that allows to develop stable turbulence intensity and length scale levels before the test section (Figure 2.2). The test section, with 1.04 m of height and 2 m width, permits testing scaled buildings and small wind turbines. Its maximum wind speed is 20 m/s and its base turbulence level is 0.5%.

Figure 2.2: View of the VUB wind tunnel with the VAWT prototype in its interior.

2.1.3 VKI L-1B wind tunnel

The VKI (Von Karman Institute) Wind Engineering facility L-1B consists of a specially designed test section interchangeable with that of the low speed wind tunnel L-1A and hence using the same return circuit, motor and power supply. The rectangular test section of L-1B is 2 m high, 3 m wide and 20 m long with a roughened floor to allow the growth of a turbulent boundary layer similar in nature to the lower part of the atmospheric neutral boundary layer.

Flow velocity can be varied between 2 and 50 m/s making it one of the most powerful facilities of this type as far as Reynolds number simulation is concerned. Also it is the largest wind tunnel that can be found in Belgium. At the end of the section a 2.6 m diameter turntable is provided for the investigation of building aerodynamics as a function of wind direction.

Figure 2.3: Interior of the VKI L1B wind tunnel, with the VAWT prototype mounted at the turntable.

2.2 Flow measurement equipment

2.2.1 Pitot tube

In all three wind tunnels the mean flow speed was monitored with a Pitot tube. At CRIACIV and VUB the pitot was connected to a sensor Setra AccuSense model ASL industrially calibrated, while in the VKI it was connected to a water manometer previously calibrated on site. The free stream wind speed was set placing the Pitot tube in the test section, before the turbine or the blade models were placed there. Due to the low frequency response of the Pitot tube, it was only used to control the mean wind speed.

2.2.2 Hot Wire Anemometer

Thanks to its high frequency response (up to 200 kHz) the hot wire anemometer could be used to monitor turbulence and obtain the frequency spectra of the measurements. Two different models of HWA were used in the campaign.

At CRIACIV, the spectral properties of the induced turbulence were determined through measurements with a Dantec single-component hot-wire probe 55P11 connected to a Dantec CTA 56C01 module and a 56C17 bridge.

At VUB the wind flow characteristics were measured with a compact Constant Temperature Hot-Wire Anemometer, model Dantec mini-CTA 54T42.

In both cases the time histories obtained from the hot-wire were acquired by a National Instruments Card and processed using Labview software to obtain the mean speed and turbulence levels. The calibration of the HWA was done using the wind speed given by the pitot tube as a reference.

At VKI, the turbulence conditions were obtained prior to this study by the center researchers, and are reported in [Buckingham, 2010].

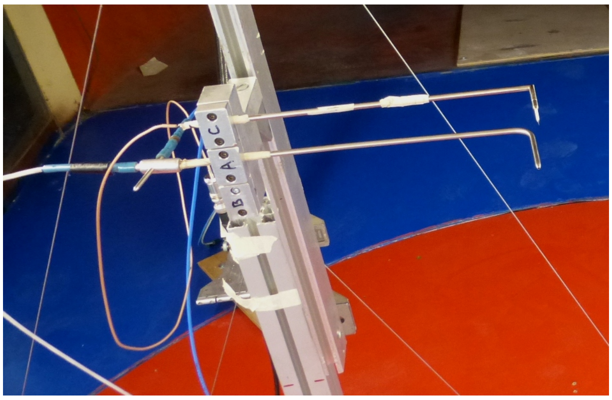

Figure 2.4: Hot wire anemometer (top) and Pitot tube (bottom) mounted on a probe support.

2.2.3 Traverse system

To scan the wake and obtain the vertical and horizontal wind profiles of the wind tunnel, a traverse system was designed and built.

At CRIACIV, the choice was a rig composed by a stiff aluminium arm mounted on an endless-screw activated with a stepper motor controlled through an Arduino-based algorithm. Three probes could be mounted on the rigid fork connected to the moving aluminium arm, one central Pitot tube, to measure the mean punctual flow speed, and two hot-wire probes for measuring the fluctuating component of longitudinal wind speed. In this way, an adequately refined wind and turbulent profile could be obtained for each tested configuration. The test rig and the probes are visible in Figure 2.5.

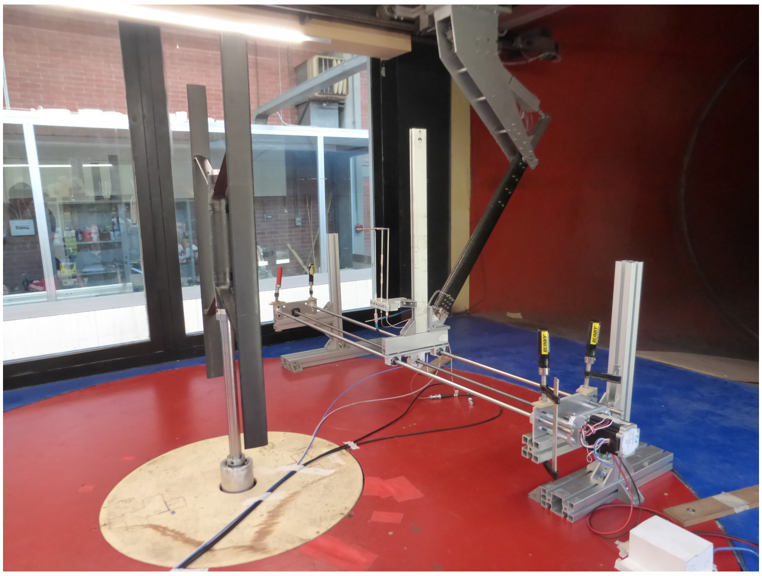

Figure 2.5: Traverse system in the CRIACIV wind tunnel behind the VAWT protoype.

At VUB, the traverse was built using aluminium profiles and a belt that moved a cart where the stepper motor was mounted and the hot wire anemometer attached. The system was also controlled by Arduino and can be observed in Fig 2.6.

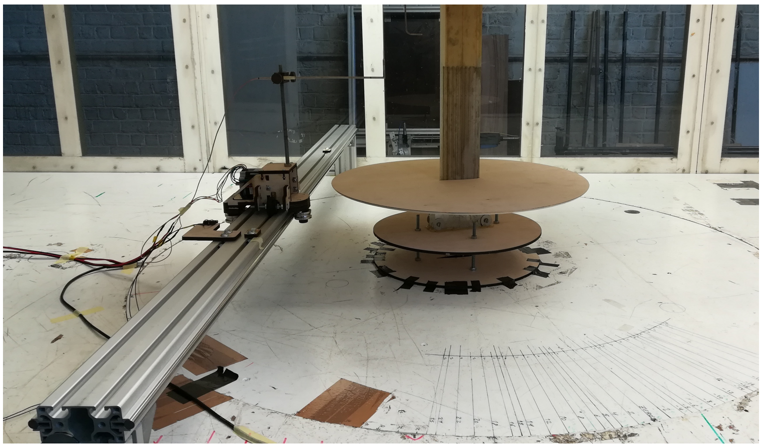

Figure 2.6: Traverse system in the VUB wind tunnel behind the blade model.

2.3 Turbine measurement equipment

2.3.1 Rotor

The rotor prototype used in this study was designed and manufactured by the FLOW group at the VUB. It is a two-blade H-type Darrieus turbine with a diameter D of 0.5 m. It has two NACA0018 blades with a 5 cm chord (c) and 0.8 m span (H) and two inclined struts per blade (see Figures 2.7 and 2.8). Due to the small size of the rotor, angular speeds (and thus centrifugal loads) were high in order to achieve the suitable Reynolds numbers on the blades. To ensure proper mechanical properties, the rotors were manufactured using carbon-epoxy composite. The VAWT rotor was connected via a torque sensor and a drive belt (with gear ratio 100/28) to a brushed-DC motor. This motor was used to drive the VAWT rotor during start-up, while it acted as a generator in normal operation. The electrical output of the motor was fed to a circuit of variable resistance for angular speed control.

2.3.2 Support structure

The turbine was supported by an aluminium modular frame already tested in other VAWT measurements, also developed at VUB before this study. This frame contains the measurement equipment of the turbine performance, and the motor/generator that actuates it. At the same time, this aluminium frame was attached to a second aluminium frame that was adapted at the

Figure 2.7: H-Darrieus VAWT prototype in the VUB wind tunnel.

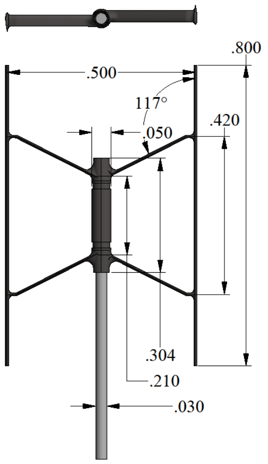

Figure 2.8: Dimensions in m of the VAWT used in the experiments.

geometry of each wind tunnel, and provided the stability to the structure, either with added weight or strapped to the wind tunnel structure. Figure 2.9 shows this support structure under the CRIACIV wind tunnel turntable. The small frame (top) subjects the turbine shaft and hosts the measuring equipment (Figure 2.10). The lower frame provided structural rigidity to the previous one, and was anchored to the floor via weights.

2.3.3 Other systems

The speed-up of the turbine (H-Darrieus has no self-start capacities) was done using an external power supply of 24 V until the turbine started lifting by itself. At this point the system was changed into generation mode. The electrical output of the motor was fed to a circuit of variable resistance for angular speed control (Figure 2.11). A torque sensor was used to measure the mechanical torque and angular speed (and thus mechanical power) of the VAWT. The torque sensor, drive belt, DC motor, and measurement equipment were housed inside an aluminium frame. The torque sensor was a Lorenz Messtechnik DR-3000 sensor with an accuracy of $2 \cdot 10^3$ Nm. It was fitted between two torsionally-stiff couplings to allow for possible misalignments. An encoder system (controlled by Arduino) was also placed in the shaft in order to have an external measurement of the rotation speed of

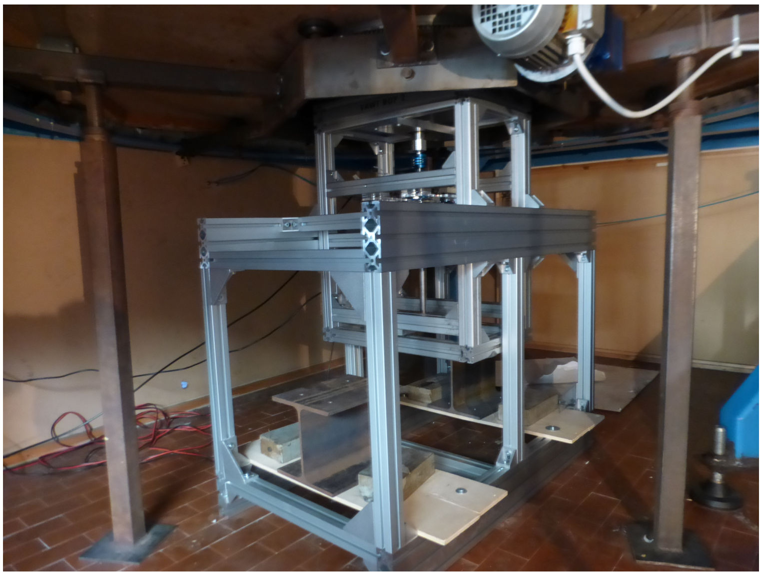

Figure 2.9: Turbine support structure under the CRIACIV wind tunnel test section. The two frames are visible, as well as the added weight to anchor it on the floor.

the turbine (Figure 2.10).

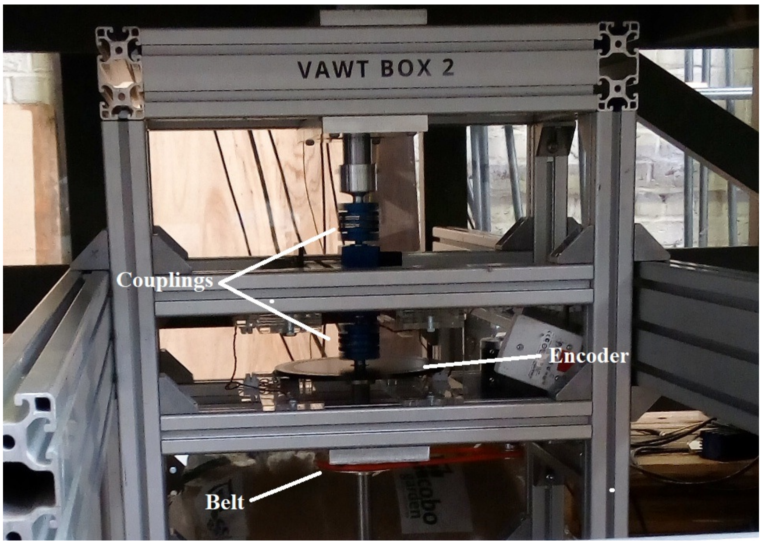

Figure 2.10: Image of the turbine measurement equipment (couplings, encoder, belt) placed inside the upper aluminium frame.

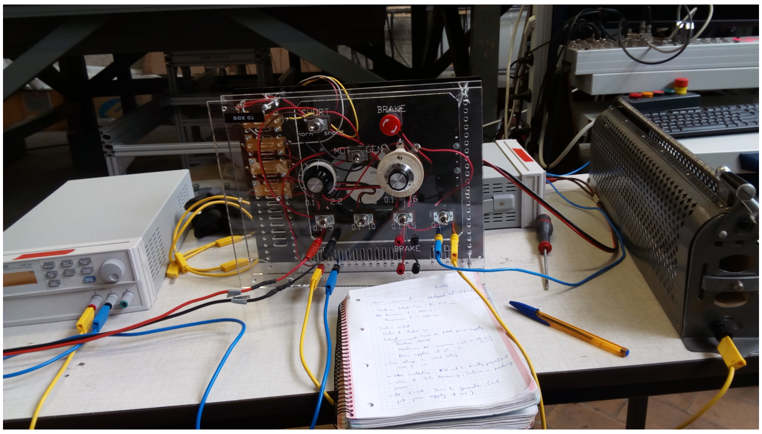

Figure 2.11: Systems used to control the rotational speed of the turbine. Power supply (left) control panel (centre) and variable resistor (right).

2.4 Airfoils measurement equipment

2.4.1 Blade with pressure taps

In order to obtain chord Reynolds numbers of 10^5 (a reasonably high value comparable to the operation of small wind tubines) within the wind speed range of the wind tunnel, a model was selected with a chord of 10 cm. The design and building of this model was done by a VUB Master student as part of his thesis [Van de Maele, 2018]. The location of the pressure tabs was chosen from literature [Barlow et al., 1999] (Table 2.1) and its position can be observed in Fig 2.12. To ensure the desired structural properties, the blade was made by laminating fiberglass, using an aluminium mould to obtain the desired shape. The mould was manufactured with a CNC-milling machine using CAD-drawing and CAM-software by Autodesk Inventor. The pressure tabs were drilled into a brass tube positioned underneath the surface of the blade (Fig. 2.13), and two rows of pressure tabs were drilled with to average out error measurements. After all tubes were positioned the model was filled with polyurethane foam.

Tap	1	2	3	4	5	6	7	8	9	10	11	12	13
x (cm)	0.125	0.250	0.5	1	1.5	2	3	4	5	6	7	8	9

Table 2.1: Positions of pressure taps along the chord of the aerofoil model.

Figure 2.12: Detail of the pressure taps drilled along the blade chord.

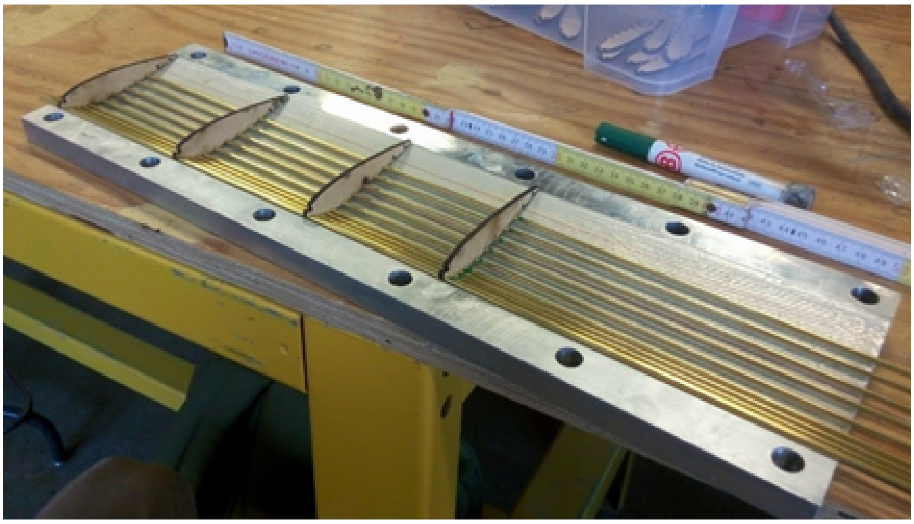

Figure 2.13: Positioning of the tubes with the aid of jigs.

The blade was clamped to an aluminium block for rigidity and end plates were added at the tips of the blade to avoid 3D effects. Fig. 2.14 gives a clear overview of all components. The pressure retrieved by the tubes connected to the pressure tabs was analysed by a Scanivalve pressure transducer system. This system can measure up to 64 channels, of which only 13 were used plus one for the static pressure in the free stream. It had a full scale range of 2.5 kPa, providing an accuracy of 0.15% of this range (approximately 3.7 Pa). The data acquisition was done used a software provided by the company, while the analysis of this data was done using Matlab.

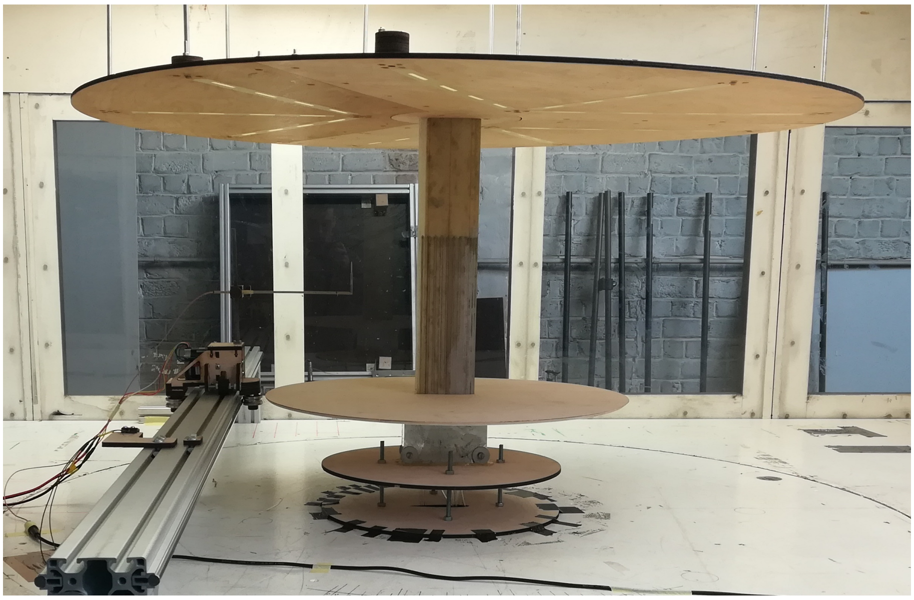

Figure 2.14: Airfoil model overview, with end plates and traversing system.

2.4.2 Model for the aerodynamic balance

The aerodynamic coefficients obtained from the pressure distributions were also benchmarked with measurements obtained with an aerodynamic balance. The balance used for the test was manufactured by ME-Messysteme GmbH. The limitations and precision of the balance in each direction are presented in Table 2.2.

	Fx	Fy	Fz	Mx	My	Mz
Nominal load	100 N	100 N	200 N	10 Nm	10 Nm	10 Nm
Measure Uncertainty	±0.2 N	±0.3 N	±0.5 N	±0.05 Nm	±0.05 Nm	±0.05 Nm

Table 2.2: Maximum loads and precision of the aerodynamic balance.

As the model equipped with the pressure taps could not be mounted on the aerodynamic balance, a second wind tunnel model was made. This time the construction process was simpler. Using the same NACA0018 mould, it was closed at one end and two threaded rods and a carbon fibre spar were centered to provide stiffness. Then the mould was filled with polyurethane which cured in 15 minutes. After the polyurethane was set, the moulds were opened and the blade was ready. A wooden adapter and a new end-plate were also build in order to fit the new model to the balance geometry. The whole system mounted in the VUB wind tunnel can be observed in Figure 2.15.

Figure 2.15: NACA0018 model for the aerodynamic balance mounted at VUB wind tunnel.

2.4.3 Model of a cambered aerofoil

A parallel campaign belonging to this project was done by testing in a similar way a cambered aerofoil proposed by Rainbird [Rainbird et al., 2015]. This aerofoil is a modification of a NACA0018 adapted to the virtual camber effect that the blade experiences while rotating in VAWTs of high c/R ratio (0.2 in the present case). As seen in Figure 2.16, the thickness of both profiles is the same, but the modified version adds up a bit of camber to the typical shape of a NACA0018.

A 20 cm chord model was built by a VUB Bachelor student Julen Echeverria by laser cutting and glueing together wooden aerofoil sections [Echeverria, 2018]. The model can be seen in figure Fig. 2.17.

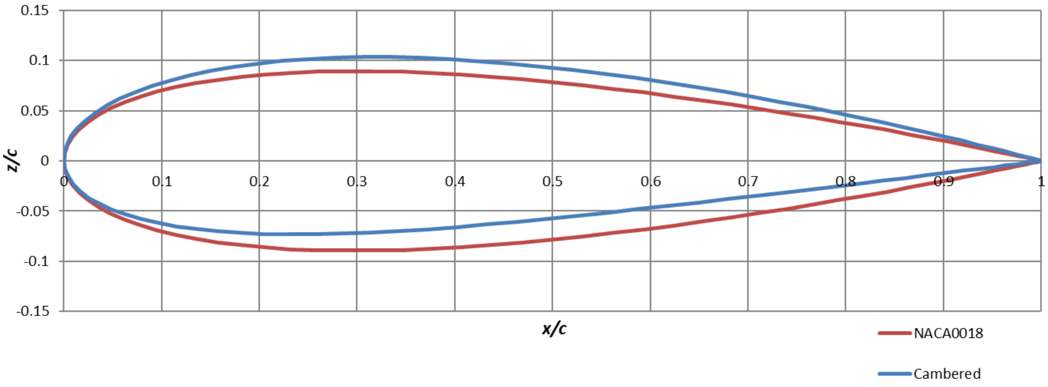

Figure 2.16: Relative size of the NACA0018 aerofoil and the cambered version developed by [Rainbird et al., 2015].

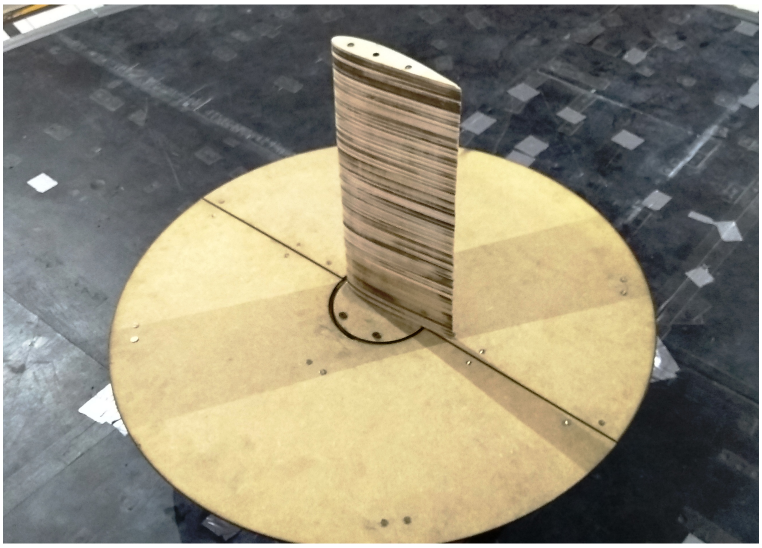

Figure 2.17: Chambered aerofoil model for the aerodynamic balance mounted at VKI wind tunnel.

2.4.4 End-plates

In blades with aspect ratio (H/c) lower than 10, as it is the case, tip vortexes decrease significantly the lift [Hand and Cashman, 2017]. End plates were used to limit these 3D effects, so the flow could be considered 2D for simplicity in the calculations. Apart, the end plate prevented interference created by the aluminium block and other structures below the profile. The criteria for the design of this end plate was that it should be bigger than

8 times the chord of the profile [Kubo and Kato, 1986]. Due to practical reasons the end plate was chosen to have a diameter of 70 cm as this was the maximum circle that could be cut from the wood provided at the FabLab workshop at VUB. Moreover, a larger end plate on the bottom would make it impossible to place the traverse system close enough to measure the wake at the desired distance of one chord from the blades trailing edge. Special attention was given to the edges of the end-plate. If they were left to be rectangular they would act as a flat plate perpendicular to an airflow. For this reason the edges were trimmed into a wedge shape. The effect of the end plate was quantified during the experimental campaigns.

2.5 Blockage corrections

2.5.1 Explanation of the problem

The effect of blockage is another of the topics that have gained attention in the last years. When the turbine model “blocks” a large part of the wind tunnel section, the flow around it is accelerated. That causes that performances measured in small wind tunnels are not realistic, higher than in real open air cases. Among others, Ross applied the available blockage corrections for bluff bodies into a Savonius drag-driven rotor [Ross and Altman, 2011]. Its effect for Darrieus turbines is still being discussed within the scientific community; Dossena defined an experimental correction that included thrust coefficient and tip-to-speed ratio [Dossena et al., 2015], while other researchers [Bianchini et al., 2011, Jeong et al., 2014] opted for more simplified approaches. It is generally accepted that corrections must be applied for solid blockages (ϵ) over 0.1 [Battisti et al., 2016], ϵ being the turbine frontal swept area $A_{VAWT} = 0.4$ m^2 divided by the wind tunnel frontal area in the test section A_{test} (Eq.2.1). Table 2.3 presents the values of blockage that the VAWT prototype will face in each of the wind tunnels in the study. It can be seen how only at VKI the blockage effect could be neglected.

$$\epsilon = \frac{A_{VAWT}}{A_{test}} \tag{2.1}$$

Wind tunnel	Width	Height	Test section	Blockage
CRIACIV	2.00 m	1.04 m	2.08 m^2	0.19
VUB	2.4 m	1.6 m	3.84 m^2	0.1
VKI	3 m	2 m	6 m^2	0.07

Table 2.3: Frontal areas of the test section and blockage ratios for the VAWT prototype for the 3 wind tunnels.

2.5.2 Available corrections in literature

As CRIACIV and VUB wind tunnels present levels of $\epsilon > 0.1$, blockage corrections must be applied in order to obtain realistic and comparable ratings. From the literature on the subject reviewed in Chapter 1, Dossena had the most thorough approach to VAWT blockage. However, their calculations include the thrust coefficient, value that was not measured during the present experiments [Dossena et al., 2015]. The correction proposed by Jeong was also unavailable because it was highly dependent on the configuration of the set-up, with the local velocity measured in a particular position [Jeong et al., 2014].

For the present study the work of Ross, who studied the blockage effect but for a Savonius rotor, has been taken as a reference [Ross and Altman, 2011]. The blockage correction is applied to the incident wind speed U to obtain a corrected U_c, which is then used to calculate the power coefficient and tip-speed-ratio. Using three scaled models in the same wind tunnel concluded that the correction of Maskell offered good agreement for this kind of turbines [Maskell, 1987]. Maskell's formula (Eq. 2.2), contains the parameter m defined for Savonius turbines (Figure 2.18), so its applicability to H-Darrieus (less solid) may be compromised.

$$\frac{U_c^2}{U^2} = \frac{1}{1 - m \cdot \epsilon} \tag{2.2}$$

On the other hand, the correction of Pope for wind tunnel models of “unusual shapes” [Pope and Harper, 1966], that was considered invalid for a Savonius [Ross and Altman, 2011], is often used in Darrieus studies [Bianchini et al., 2011] due to its simplicity

$$\frac{U_c}{U} = 1 + \frac{1}{4}\epsilon \tag{2.3}$$

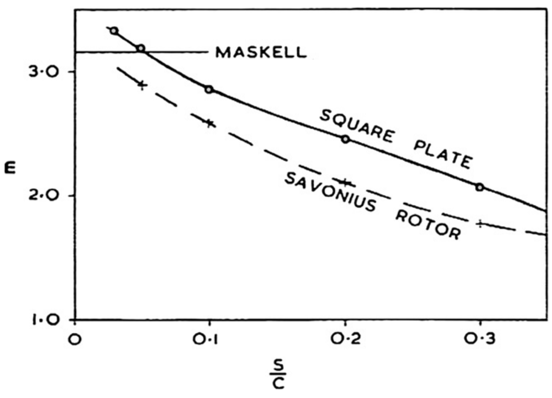

Figure 2.18: Flat plate and Savonius rotor relationship m vs S/C (ϵ in the present study), from [Ross and Altman, 2011].

Among those two formulas, Pope correction (Eq. 2.3) was the most suitable for the present study. In his study, Dossena states that this correction depends also on λ due to the change in the apparent solidity of the turbine ([Dossena et al., 2015]), however, measurements taken during this experiments reveal that this effect is of less than 0.5% of U within the λ range studied (see annex A.2.1).

2.6 Uncertainty quantification

2.6.1 Description of the procedure

Uncertainties are calculated following the recommendations of various references [Kirchner, 2001, Dénos, 2005, ITTC, 2008, Bachant and Wosnik, 2016]. The evaluation of the measurement uncertainty δ should consider both the systematic error δ_{sys} (product of the equipment and procedure limitations) and the random error δ_r, which is generally approximated using the standard deviation of the measurement (Eq. 2.4).

$$\delta = \delta_{sys} + \delta_r \tag{2.4}$$

δ_{sys} is normally provided by the equipment manufacturer, as in Table 2.2 for the aerodynamic balance or can be estimated in case of simpler equipment (0.5 K for a mercury thermometer that has markings for each degree). The standard deviation σ (used to calculate δ_r) is defined by Eq. 2.5

$$\sigma = \sqrt{\frac{\sum_i^N \left(x_i - \bar{x_i}\right)^2}{N-1}} \tag{2.5}$$

where N is the number of samples, x_i each measurement and $\bar{x_i}$ the average value. However, when calculating the standard deviation of a mean value, this factor is divided by the square root of the number of independent measurements N_i (Eq. 2.6). In this way, the random error of a mean value would be sufficiently reduced if enough samples are taken.

$$\sigma_{\bar{x_i}} = \frac{\sigma}{\sqrt{N_i}} \tag{2.6}$$

In the case that several (n) variables (x_i) affect one measurement (R) the uncertainties are calculated by the Gaussian error propagation method enounced in Eq. 2.7 and developed in detail in [ITTC, 2008].

$$\delta_R = \sqrt{\sum_i^n \left(\frac{\partial R}{\partial x_i}\delta_{x_i}\right)^2} \tag{2.7}$$

where $\partial R/\partial x_i$ is the partial derivative of the main variable R with respect to the contribution of the variable x_i, and δ_{x_i} is the uncertainty of this variable. This method is only applicable when all the component variables are uncorrelated with one another [Kirchner, 2001]. This is the case encountered in most of the error calculations within this study, but particularly in the calculation of the C_P error (Eq. 2.8) it should be checked that torque and rotational speed are not correlated.

2.6.2 Calculation of the uncertainty in the Power coefficient C_P

The power coefficient was already introduced in section 1.2. In these measurements, the power extracted by the turbine is measured through the torque-meters attached to the turbine shaft, and therefore calculated from torque Q and rotational speed ω (Eq. 2.8).

$$C_P = \frac{Q\omega}{\frac{1}{2}\rho A_{VAWT} U^3} \tag{2.8}$$

In order to be able to apply the Gaussian error propagation method, first it should be checked that Q and ω signals are uncorrelated. The correlation value, calculated using a Matlab function for all the samples analysed, was always $|\rho_{Q,\omega}| \ll 1$. As an example of this, Figure 2.19 presents the combined histogram of the two signals, for a measurement taken at $\lambda = 3$ with $U = 9$ m/s and $I_u = 9\%$. The resulting histograms show a Gaussian distribution for both variables, without any sign of dependency.

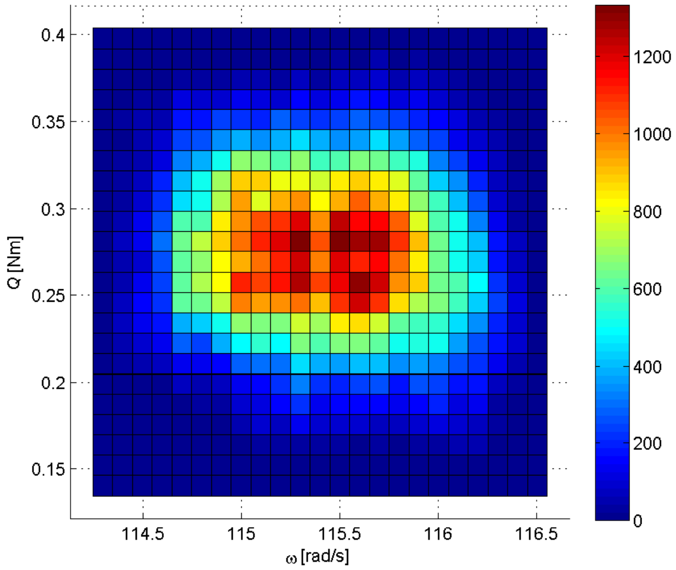

Figure 2.19: Combined histogram of the Q and ω signals at a measurement at medium λ with $U = 9$ m/s and $I_u = 9\%$.

After this verification, the procedure follows by introducing the uncertainty of each component variable into equation 2.7. Specifically, the sources of error for each variable are:

- Torque Q: the sensor accuracy is the main source of error. The random error is reduced as many samples are taken for each Q.
- Angular speed ω: Same as in torque.
- Density ρ: Density is calculated with the perfect gases law from the values of Pressure and Temperature. The accuracy in those measurements must be considered.

- Geometry D, H: If the measure is done accurately, their contribution in the error is small.
- Wind speed U: The first source of error in U comes from the anemometer calibration. A Hot Wire Anemometer is very precise, but the Pitot tube used to do the calibration is not so much, adding uncertainties to the measurement. The second source is the uniformity of the wind speed profile over the turbine swept area (called σ_u in Chapter 3).

Table 2.4 shows how the different parameters in Eq. 2.8 contribute to the uncertainty value of C_P in free stream and turbulent cases, for $U = 8$ m/s. Due to the long samples taken for the measurements, the uncertainty (in non-dimensional units) is mainly affected by the uncertainty in wind speed. It will be seen in Chapter 3 how the velocity profiles at high turbulence are less uniform, and therefore that would be the reason why uncertainties are higher are the incoming I_u is increased.

Parameter	**Contribution to C_P uncertainty**		
	$I_u = 0.5\%$	$I_u = 6.0\%$	$I_u = 9.6\%$
Q	2.12E-3	2.11E-3	2.21E-3
ω	4.37E-4	4.36E-4	4.56E-4
ρ	5.70E-5	4.74E-5	1.67E-4
D	6.88E-4	6.87E-4	7.18E-4
H	1.10E-3	1.10E-3	1.15E-3
U	3.98E-3	5.78E-3	7.08E-3
Total uncertainty	**4.71E-3**	**6.30E-3**	**7.55E-3**

Table 2.4: Contribution of the different parameters onto the C_P uncertainty, for different values of turbulence at the optimal performance point for $U = 8$ m/s.

Chapter 3

Generation of turbulence in the wind tunnel with passive grids

3.1 The use of grids to generate artificial turbulence

3.1.1 Passive grids

Squared turbulence grids have been used for decades to generate artificial turbulence inside wind tunnels. They have been known to provide quasi-isotropic, Reynolds number independent profiles, and allow to reach turbulence levels of $I_u > 15\%$ [Roach, 1986]. The turbulence intensity depends on the bar size b, and decreases with the distance x from the grid (turbulence decay). The empirical law proposed by Laneville describes accurately the I_u levels found downstream of the grid (Eq. 3.1) [Laneville, 1973]

$$I_u = 2.58 \left(\frac{x}{b}\right)^{-\frac{8}{9}} \tag{3.1}$$

The complication falls in recreating the length scales of this turbulence. In urban environments, the turbulence length scales are of the order of $L_{ux} \approx 1$ m [Dallman, 2013]. The size of the eddies depends on the bar size b, and the empirical law by Roach for L_{ux} is presented in Eq. 3.2 [Roach, 1986]:

$$L_{ux} = 0.2b \left(\frac{x}{b}\right)^{\frac{1}{2}} \tag{3.2}$$

It is true that those turbulent structures increase in length downstream, but also here there is a limitation due to the decay of turbulence intensity. Figure 3.1 shows a smoke visualization of laminar flow passing across a turbulence grid (photograph by Thomas Corke and Hassan Nagib, from van Dyke [Van Dyke, 1982]).

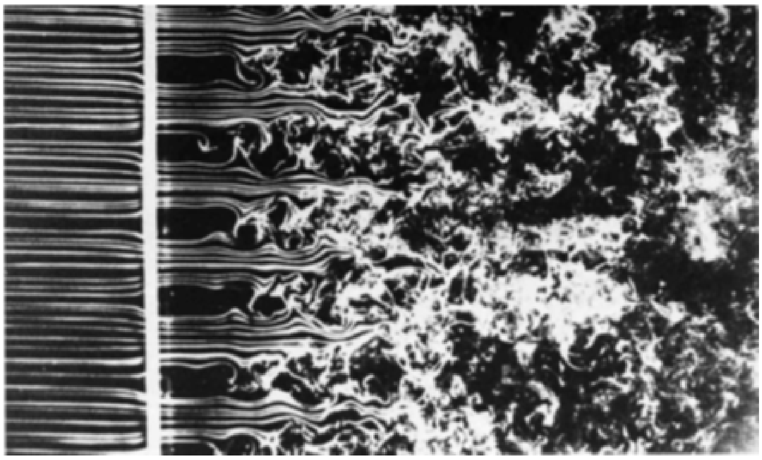

Figure 3.1: Smoke visualization of the flow passing through a turbulence grid (photograph by Thomas Corke and Hassan Nagib, from [Van Dyke, 1982].

After a careful study of literature [Laneville, 1973, Bearman and Morel, 1983, Vita et al., 2018] and previous studies at the University of Florence [Mannini et al., 2015], it is clear that the largest scales that could be generated would be in the order of $L_{ux} \approx 0.2$ m, by using large mesh sizes (M). This way, they would still be larger than the chord of the wind turbine blade, which is $c = 0.05$ m. According to Bearman, when $L_{ux} >> c$, the gross effect of turbulence can be estimated using a quasi-steady assumption [Bearman and Morel, 1983]. Though not exact, this assumption is considered as valid in this case.

The creation of a uniform profile of wind speed and turbulence was also pursued, in order to compare the results accurately against the free stream conditions. According to previous literature, the flow will be fully developed after a distance 5 times the mesh size of the grid M [Baines and Peterson,]. However, when using mesh sizes larger than 10% of the wind tunnel dimension, the wind profile is heavily unstable [Bearman and Morel, 1983], and small changes of geometry can lead to significant modifications in the flow. This is a condition that cannot be fulfilled and at the same time maintain the high values of L_{ux}. Therefore, a careful parametric study has been done to define the optimal grid geometry (Mesh size M and bar size b), to obtain the desired uniform profiles.

3.1.2 Other turbulence generation devices

In the experimental campaign carried out at VKI the objective was to test the turbine and the blades under logarithmic wind profiles, as the ones found close to the surface, and observe their effect on VAWT operation. To create them, not only a grid is necessary but also roughness elements that decrease the windspeed and increase turbulence and length scale near the floor. These elements (wooden barrier, plastic cups) can be seen at figures 1.11 and 3.2. The design and configuration of these elements was done prior by VKI students [Buckingham, 2010] and has been used in studies of wind turbine wakes before [Coudou et al., 2017].

As described in subsection 1.1.2, skewed flow and gusts also play an important role in urban winds. The first have been thoroughly studied in the past [Ferreira, 2009b], and it is generally done by inclining the axis of the VAWT. The study of the effect of gusts on VAWT has not been reported yet, but would require the use of active grid systems that allow controlling the turbulent inflow conditions in real time [Kröger et al., 2018]. The use of those dedicated set-ups was not viable for the present study.

Figure 3.2: Detail of the plastic cups placed on the floor of VKI wind tunnel to generate logarithmic wind profiles.

3.2 Design process of squared grids to obtain uniform profiles

3.2.1 Parametric study at the VUB wind tunnel

The starting point was a regular mesh of $M = 0.33$ m, with 6 cells horizontally and 3 vertically (wind tunnel test section is 2 x 1.04 m). The width of the bar is limited by the blockage it causes in the wind tunnel. From the thesis of Laneville an expression for the drag coefficient C_D is drawn (Eq. 3.3 [Laneville, 1973]).

$$C_D = \frac{\frac{b}{M}\left(2 - \frac{b}{M}\right)}{\left(1 - \frac{b}{M}\right)^4} \tag{3.3}$$

It can be seen that C_D increases drastically for values of $b/M > 0.25$. Therefore, a width slightly under this value is chosen. The grid is placed at around 4 m from the test section to obtain values of moderate turbulence. The grid is depicted in Figure 3.3.

Figure 3.3: Uniform grid with 6 x 3 cells.

For simplicity, the wind and turbulence profiles are only analysed in the vertical direction, which is the most challenging to obtain uniform profiles, as the size of the mesh is much larger than 10% of the wind tunnel height. Figure 3.4 shows the profiles of wind speed and turbulence created by the first grid, compared with the measurements taken with a clear wind tunnel. It can be seen that the profile obtained with the grid cannot be considered uniform at all, as the flow is clearly accelerated next to the walls. The uniformity of the wind profile is evaluated with the standard deviation σ_u. While the free stream velocity has a $\sigma_u = 0.05$ m/s (excluding floor and ceiling boundary layers), this value for the Grid 1 profile is $\sigma_u = 0.41$ m/s, clearly unacceptable for comparison. This can be caused by the fact that the 2 central bars create larger vortices than the ones in the walls (immersed in the boundary layer). This creates a bluff body effect in the wake of the grid. The good part of these results is that the turbulence profile is reasonably stable and its average value is $I_u = 7.89\%$, not far from the one predicted by literature.

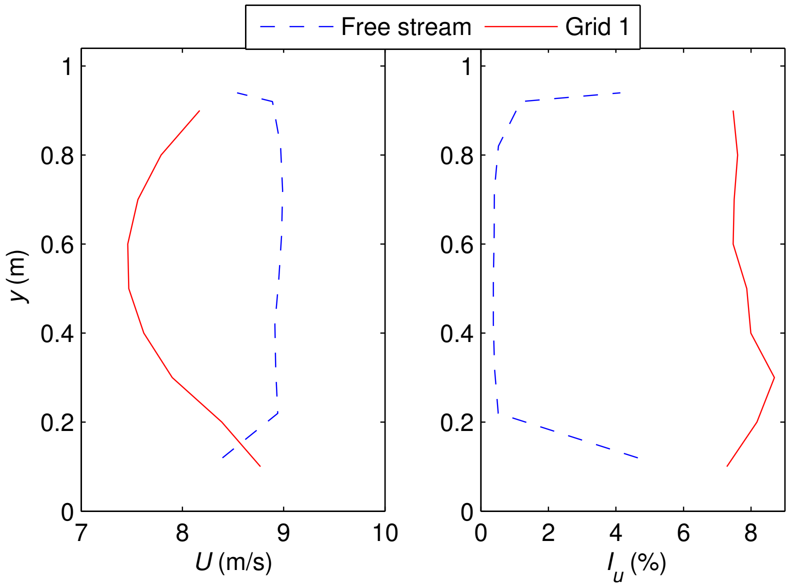

Figure 3.4: Wind speed and Turbulence intensity profiles obtained with free stream and Grid 1 at $x = 3.75$ m.

The solution to this was to reduce the space between the bars and the walls, to stop this acceleration (Figure 3.5). The grid, then, was modified several times, varying the mesh size M to select the best gap w next to the walls. In figure 3.6 the three grid modifications done after Grid 1 can be observed.

For an easier comparison, the profiles obtained with the different grids are normalized with the average values (excluding boundary layers), as the study searched the uniformity of the profile more than precise levels of wind speed or turbulence. It was predicted by literature and proved by upcoming results

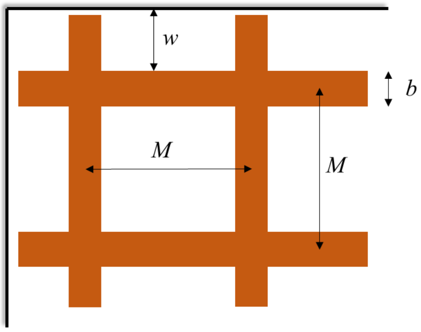

Figure 3.5: Schematic representation of the parameters used in the design of the grid.

Figure 3.6: Different modifications of the grid to obtain uniform flow. From left to right, grids 2 ($M = 0.33$ m), 3 ($M = 0.35$ m) and 4 ($M = 0.40$ m).

that the turbulence generated by squared-bars grids is not speed dependent. Figure 3.7 shows the comparison between the normalized profiles of wind speed and turbulence intensity obtained with the different grids. It can be seen that in Grid 2, reducing by half the gap to the wall, the accelerated flow is still found. On the other side, with Grid 4 the smallest gap near the walls causes the opposite effect, a jet. Grid 3 seems to be the intermediate point, although, as predicted in the literature, obtaining a uniform profile is highly complicated for these mesh sizes.

In fact, from a more extensive study it was proved that small changes in geometry (smaller than 1 cm) have large impact on the flow, and even a careful construction of the grid leads to asymmetries in the flow that cannot be easily solved. The conclusion is that an optimal flow is nearly impossible to achieve in these conditions, so the best approximation to the free stream flow must be chosen, to be able to compare successfully the turbine ratings in the various cases.

Table 3.1 summarizes the results of the preliminary study, compared with the free stream. The bar size b and the distance to the grid x are fixed.

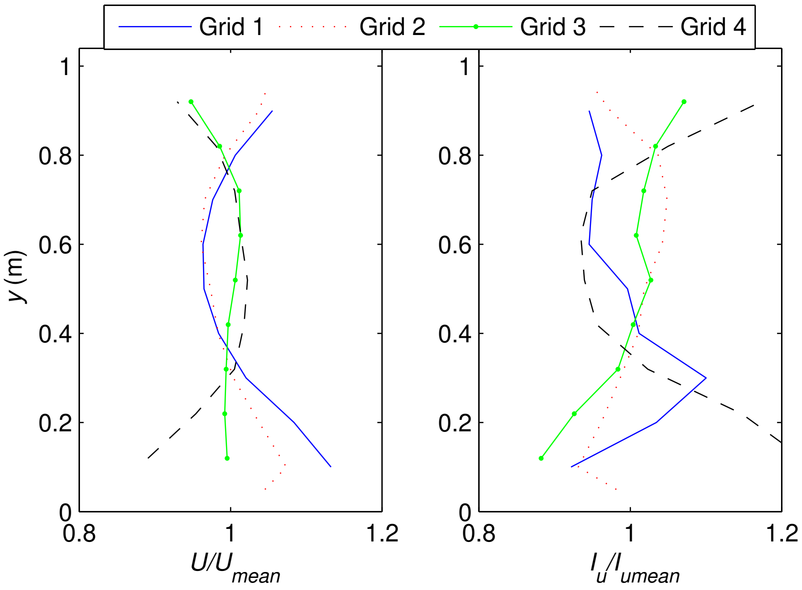

Figure 3.7: Normalized profiles obtained with the different modifications of the grid at $x = 3.75$ m.

Analysing the standard deviation of the profiles, it can be easily seen that the profile obtained with Grid 3 is the only one that can be compared with the free stream values. Even though the turbulence profile is not as good as the obtained with Grid 2, the uncertainty in wind speed is the main factor to consider when calculating turbine ratings, and its main source of error (as seen in section 2.6).

Grid muber	M (m)	b/M	w (m)	σ_u (m/s)	I_u mean (%)	σ_{Iu} (%)
Smooth flow	-	-	-	**0.05**	0.5	**0.05**
Grid 1	0.33	0.22	0	0.41	7.89	0.44
Grid 2	0.33	0.22	0.16	0.23	7.69	**0.24**
Grid 3	0.35	0.21	0.13	**0.09**	7.75	0.28
Grid4	0.4	0.18	0.08	0.21	9.34	0.74

Table 3.1: Summary of the parametric grid study.

3.2.2 Application of this study to the CRIACIV wind tunnel

A similar grid was designed for the CRIACIV wind tunnel (CRI 1 for simplicity) to generate the most similar turbulent conditions possible (Figure 3.8). A third grid of smaller mesh size has also been used in order to compare the results with turbulent flows of smaller integral length scale (CRI 2). This grid was built in CRIACIV for previous experiments [Mannini et al., 2015], and can be seen in Figure 3.9. The geometrical characteristics of each grid can be compared in Table 3.2. As it can be seen, in grid CRI 2 no optimization of the wall distance is needed as $M/H < 0.1$ [Bearman and Morel, 1983].

Figure 3.8: Grid 1 CRIACIV ($M = 0.35$ m).

Figure 3.9: Grid 2 CRIACIV ($M = 0.10$ m).

Grid	M (m)	b (m)	b/M	w (m)	M/H
VUB	0.35	0.072	0.21	0.13	0.34
CRI1	0.33	0.07	0.22	0.13	0.20
CRI2	0.01	0.025	0.25	0	0.06

Table 3.2: Geometrical characteristics of the grids used in the study.

3.3 Generation of different levels of turbulence and integral length scale

3.3.1 Conditions obtained at VUB

The wind speed of 9 m/s was chosen as a benchmark as it allowed the widest range of rotational speeds in the turbine prototype available. That would constitute an approximate turbine Reynolds number of:

$$\mathrm{Re}_D = \frac{\rho U D}{\mu} = 300,000 \tag{3.4}$$

In this case the number is expressed considering the turbine diameter D as a reference length. If we consider the definition of chord Reynolds number (Re_c) given by Eq. 1.10 in Chap. 1, that would result in a mean $\mathrm{Re}_c = 95{,}000$ at the optimal point of operation of the VAWT.

As explained in previous chapters, moving the aforementioned grids upstream and downstream along the wind tunnel, different values of I_u and L_{ux} could be obtained. Figure 3.10 shows the vertical profiles of wind speed, turbulence and length scales obtained at the VUB wind tunnel when placing the grid at different distances x. As it can be seen, going closer to the grid, the flow is more turbulent, L_{ux} is smaller and the profiles uniformity is lower. However, all the conditions depicted in Figure 3.10 are considered stable enough and within the desired range of the experiment. In order to maintain flow uniformity, the minimum distance at which the grid could be placed was $x = 3$ m.

Figure 3.11 represents the turbulence spectrum obtained at the test section centre with the grid at $x = 3$ m and $U = 9$ m/s, with values of $I_u = 9.5\%$ and $L_{ux} = 0.10$ m. The vertical axis presents the spectral density S_u non-dimensionalized with the fluctuations u value squared. The abscissa is the wave number $k = 2\pi f/U$. The data is collected with a HWA at a frequency $f = 500$ Hz and analysed using the Welch's power spectral density estimate. The spectrum is fitted to the formula for the Von Karman spectrum enounced in Eq. 1.5 [Burton et al., 2001] and the -5/3 slope (predicted by Kolmogorvov for the inertial sub-range) is presented in green [Jiménez, 2004]. The measured spectrum fits well with the Von Karman one and the Kolmogorov slope, with only small noise at high frequencies. This noise could not be completely removed from the signal, but appeared not to have

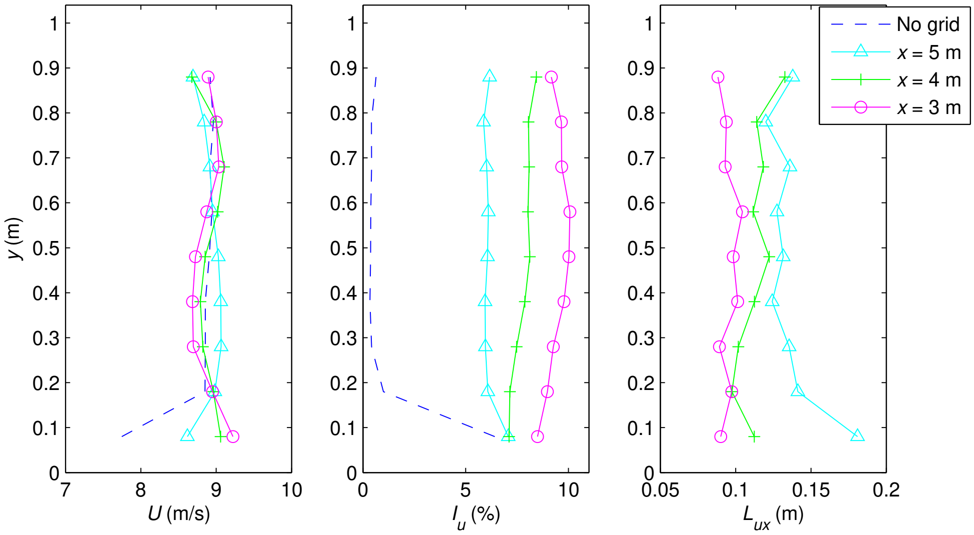

Figure 3.10: Vertical wind profiles obtained with Grid 1 at the VUB wind tunnel, measured at three distances downstream of the grid.

an important effect on the measurements.

3.3.2 Conditions obtained at CRIACIV

Figure 3.12 presents the wind profiles obtained with grid CRI 1. Here it was possible to approach the grid closer to the test section ($x = 2.1$ m), and it can be seen how I_u levels reached were higher, but at the cost of a less uniform wind profile highly affected by the grid bars. Being a larger wind tunnel, it was also possible to place the grid farther away reaching lower I_u and higher L_{ux}. However, for larger distances ($x > 7.6$ m), the wind profile did not vary much with further distance increase.

However, when using grids of different mesh and bar size (grid CRI 2), turbulence characteristics change. Figure 3.13 presents the wind profiles obtained with grid 2 at the CRIACIV wind tunnel. As it can be seen, the use of a smaller mesh creates very uniform profiles even at short distances ($x = 2.1$ m), but does not allow to achieve high values of I_u and L_{ux}. That precise profile will allow to evaluate the effect of L_{ux}, as it provides similar values of I_u as grid CRI 1 at $x = 7.6$ m ($\approx 5\%$), while the values of L_{ux} are much smaller ($\approx c$ in this case).

Figures 3.14 and 3.15 present the turbulence spectra at CRIACIV, where

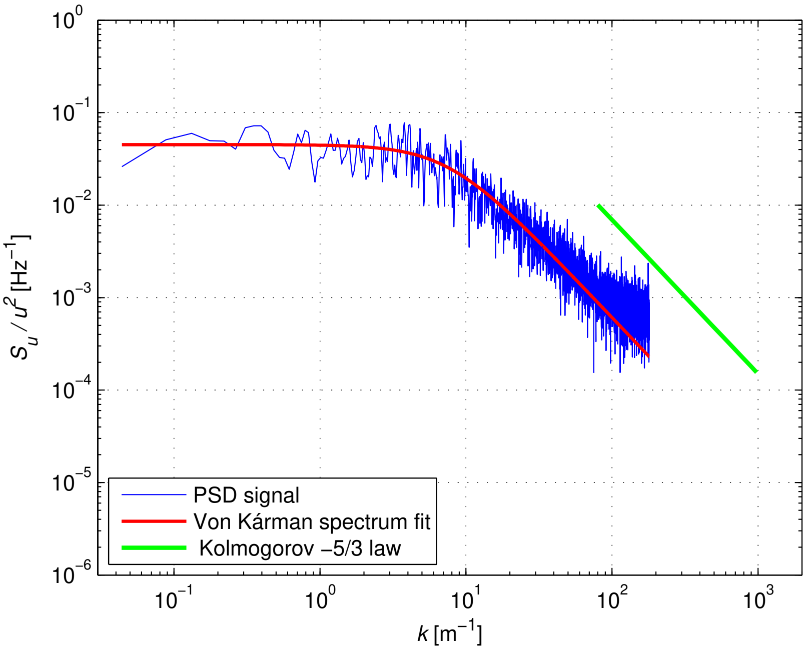

Figure 3.11: Turbulence spectrum obtained with the grid at $x = 3$m at the VUB wind tunnel (blue), fitted to Von Karman spectrum (red) and the Kolmogorov turbulence decay -5/3 law marked in green.

the sampling frequency was of 2000 Hz and therefore larger part of the spectrum could be retrieved. Both samples present a similar level of turbulence ($I_u \approx 5\%$), the first measurement was done with grid 1, and therefore a larger $L_{ux} = 0.18$ m, while the second figure comes from an experiment with grid 2, and has smaller $L_{ux} = 0.05$ m. This is visible by the different shape of the spectrum, but therefore in both cases the fit with the Von Karman spectrum and the Kolmogorov slope is accurate.

3.3.3 Comparison with literature

Figure 3.16 presents the average values of I_u (upper graph) and L_{ux} (lower) obtained with the different grid positions shown in the previous figures. The values are compared with the predictions made by Laneville (Equation 4 [Laneville, 1973]) and Roach (Equation 5 [Roach, 1986]). It can be seen how the trends were accurately predicted by the literature, especially in the I_u case, and that the laws only tend to underestimate I_u and L_{ux} for high values.

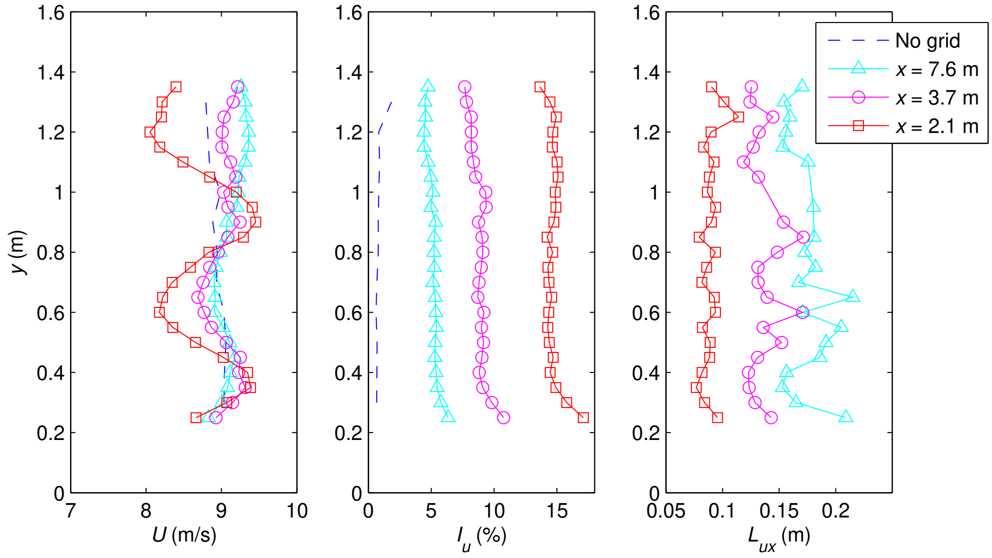

Figure 3.12: Vertical wind profiles obtained with Grid 1 at the CRIACIV wind tunnel, measured at three distances downstream of the grid.

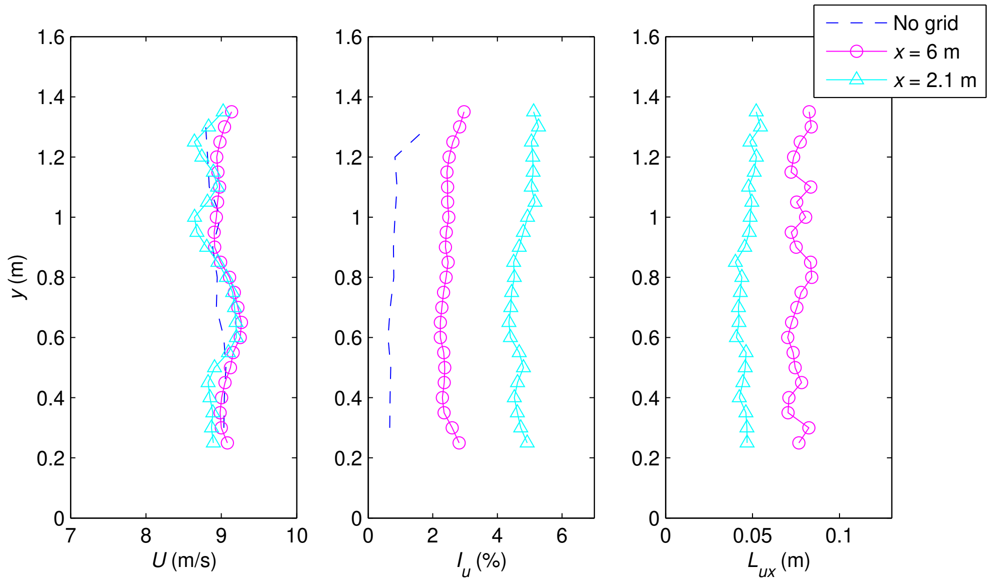

Figure 3.13: Vertical wind profiles obtained with Grid 2 at the CRIACIV wind tunnel, measured at two distances downstream of the grid.

This is understandable given that both empirical relations were developed

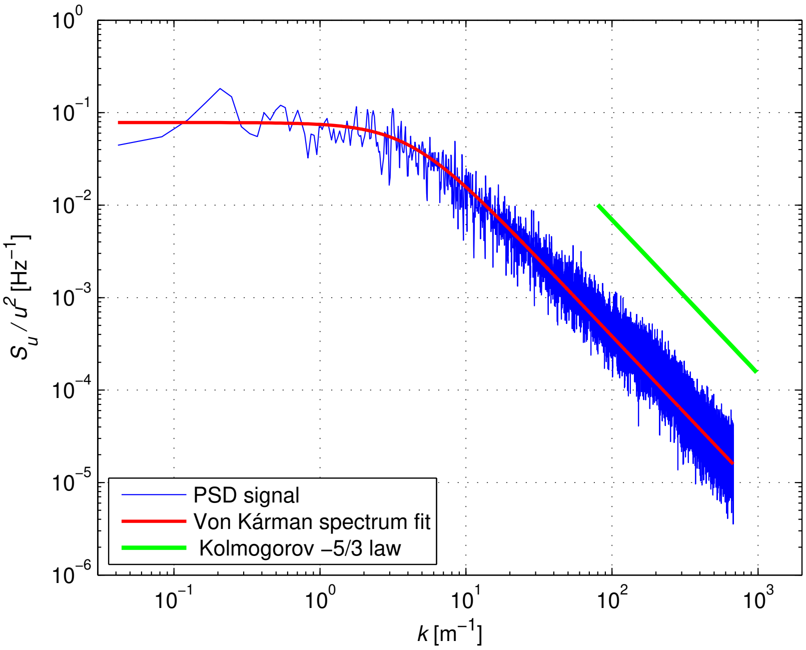

Figure 3.14: Turbulence spectrum obtained with the grid 1 at $x = 7$m at the CRIACIV wind tunnel (blue), fitted to Von Karman spectrum (red) and the Kolmogorov turbulence decay -5/3 law marked in green.

in wind tunnels smaller than the ones used in this study, therefore also the size of the grids was smaller (only comparable with CRIACIV grid 2, which is the most accurately predicted).

3.3.4 Conditions obtained at VKI

The campaign at VKI allowed to test turbine and blades under special turbulent conditions. Using pre-defined combinations of roughness elements, profiles with high I_u and L_{ux} in the lower area of the wind tunnel were generated [Buckingham, 2010]. As the models (blade and VAWT) were mounted in the lower area of the wind tunnel only the averages where $y < 1$ m is of interest. The profiles of U, I_u and L_{ux} can be appreciated at Figure 3.17. Those profiles where measured prior to the campaign by VKI students, and are more defined in the lower area of the wind tunnel as they were intended for scaled building aerodynamics.

Calculating the incoming wind speed U for C_P is tricky for logarithmic

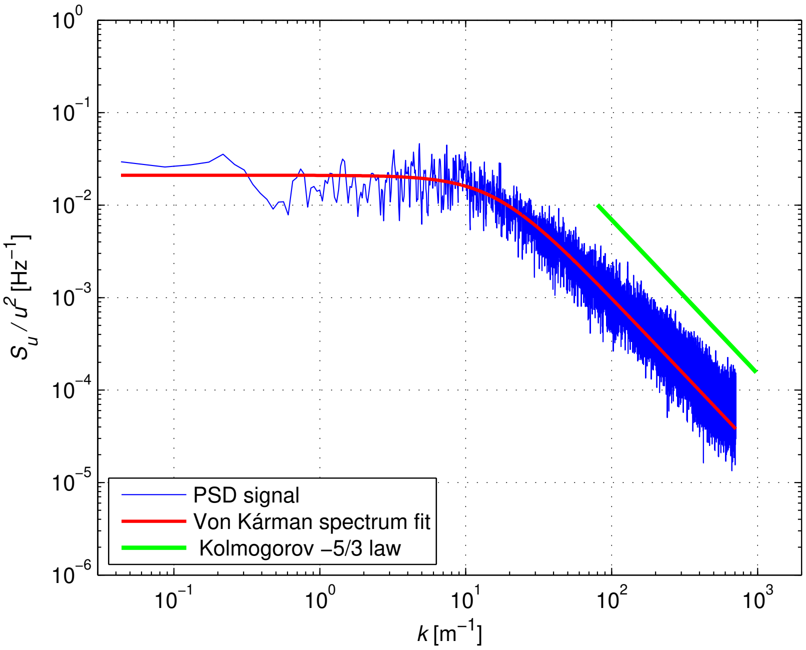

Figure 3.15: Turbulence spectrum obtained with the grid 2 at $x = 2$m at the CRIACIV wind tunnel (blue), fitted to Von Karman spectrum (red) and the Kolmogorov turbulence decay -5/3 law marked in green.

wind profiles. In this case, it was decided to use a cubic mean of the wind speed, as it is the direct effect it will have on C_P (Eq. 3.5):

$$U = \sqrt[3]{\frac{1}{N}\sum_{i}^{N} U_i^3} \tag{3.5}$$

where N is the number of sample heights and U_i the time-averaged wind speed in each of them. In the case of I_u values and L_{ux}, that mean was not necessary as the values were relatively uniform in the area of interest. The mean conditions are calculated in the span of the VAWT blades (from 10 to 90 cm from the ground), while I_u and L_{ux} are supposed to be speed-independent. For the blade aerodynamic tests (chapter 6) the profiles of interest went from 17 to 57 cm (40 cm blade span), and the mean was calculated with the squared version of the generalized mean presented in Eq. 3.5, as in this case U has a square relationship with C_L and C_D coefficients. The conditions for the VAWT and blade studies are presented in Table 3.3.

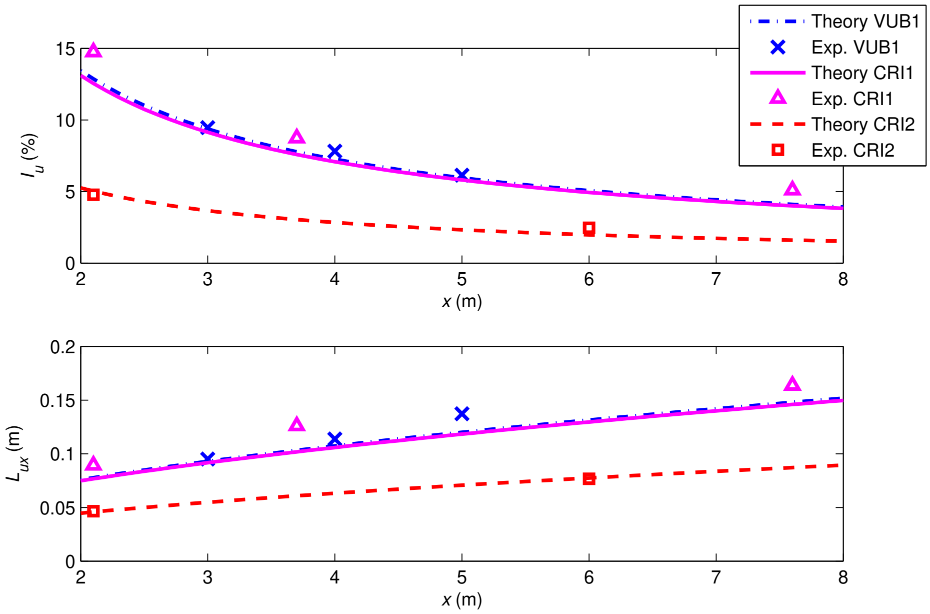

Figure 3.16: Comparison of the average I_u (up) and L_{ux} (down) values obtained with the different grids with the values predicted by literature [Roach, 1986, Laneville, 1973].

	U (m/s)	I_u (%)	L_{ux} (m)
VAWT study	10.87	9.65	0.38
Aerofoil study	10.35	10.7	0.42

Table 3.3: Calculated mean conditions within the blade span set in the VKI experiments.

3.4 Discussion of the results

This chapter was devoted to the modelling of urban flows inside the wind tunnel in preparation of VAWT testing. The challenge is that base turbulence in most wind tunnels is of the order of $I_u = 1\%$, much lower compared to the usual values in urban environments ($I_u > 10\%$). Luckily, the three wind tunnels available for measurements are of the boundary layer type, meaning that they have an empty space upstream the test chamber that allows the installation of turbulence generation devices.

In our case passive grids were the chosen device, as they allow to create

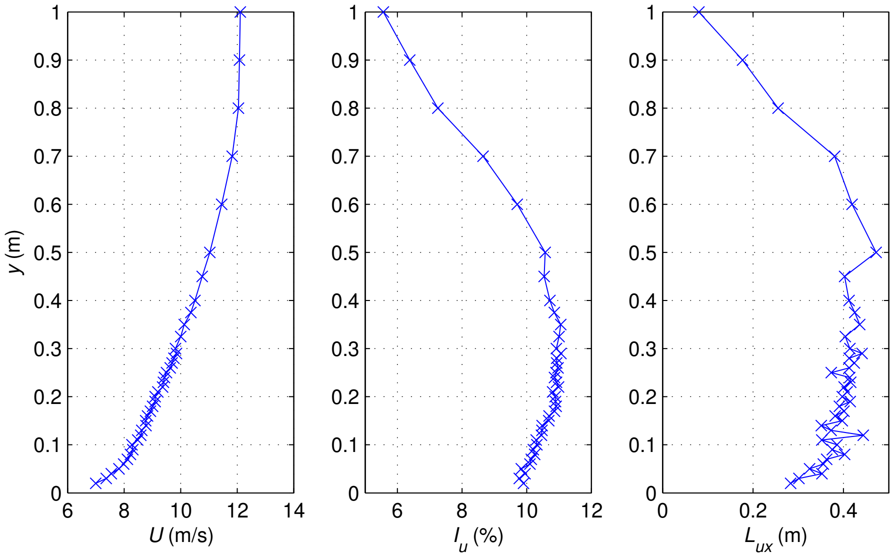

Figure 3.17: Wind profiles obtained at VKI wind tunnel.

isotropic, Reynolds number-independent turbulence up to levels of $I_u = 15\%$. The main problem encountered was that in order to generate relatively high levels of L_{ux} mesh and bar sizes had to be too large compared with the height of the wind tunnels. Due to that fact, wind speed profiles were very dependent of grid sizes, and small changes of cms in the grid geometry caused large differences in the wind speed profile.

A careful optimization of the grids performed at VUB wind tunnel resulted in grid wind profiles uniform enough to be compared with the smooth flow ones. The conclusions extracted from VUB were then applied to the larger CRIACIV wind tunnel, obtaining a set of wind profiles with a range of I_u from 1 to 15% and L_{ux} from 4 to 19 cm. The empirical relations of Laneville for I_u and Roach for L_{ux} proved to predict those values very accurately. The turbulence spectra measured fit well with the Von Karman prediction, and also respected the Kolmogorov -5/3 law for the inertial subrange.

The tests at VKI were done with particular wind condition of shear flows with large values of I_u and L_{ux} due to the in-home turbulence generation devices. The study of skewed flow and gusts was left outside of this project but they could be considered for future work on the topic.

Chapter 4

Testing the effect of turbulence on VAWT performance

4.1 Power curves parametric study

In this chapter, the VAWT prototype was tested under the turbulence conditions exposed in Chapter 3. The goal of this parametric study was to isolate the effect on turbine performance of three features of the flow: Reynolds number (or wind speed), Turbulence intensity I_u and integral length scale L_{ux}. Repeating the tests at CRIACIV and VUB wind tunnels (of different sizes) serves as validation of the conclusions as well as to evaluate the blockage corrections proposed at section 2.5. The main indicator for turbine performance is the non-dimensional Power Coefficient (C_P, Eq. 4.1), that is plotted against the tip-speed-ratio (λ, Eq. 4.2), as was introduced in section 1.2.

$$C_P = \frac{Q\omega}{\frac{1}{2}\rho A U^3} \tag{4.1}$$

$$\lambda = \frac{\omega R}{U} \tag{4.2}$$

Each measurement was taken only when the turbine ω remained stable within a range of ± 2 rad/s during 60 s to avoid transient effects and reduce the random error in the mean values of Q and ω, as explained in section 2.6.

4.1.1 Reynolds number effect and blockage corrections

To evaluate the effect of the Reynolds number (via the change in U) only the measurements in smooth flow (no grid) were considered. Apart from the benchmark speed, power curves were also measured at $U = 8$ m/s (Re = 267,000) and $U = 10$ m/s (Re = 333,000) to provide an indication of the Reynolds number effect. Those value of Re are calculated with D as a reference length (Equation 3.4). However, for studies focusing on the aerofoil aerodynamics, Reynolds number is often referred to the chord of the blades c. In this case, the effective U is the one perceived by the blades and changes on the blade position and the rotational speed. For simplicity and according to references, Re_c is calculated as in Eq. 4.3. As the rotational speed (and therefore λ) changes to obtain every curve, the values of Re_c would be different for each measurement. To have an indication of this parameter for the present measurements, Table 4.1 shows the values of Re_c for each flow condition, at $\lambda = 2.5$ (low ω), $\lambda = 3.5$ (high ω) and $\lambda = 3$ (around the maximum efficiency point).

$$\mathrm{Re}_c = \frac{\rho \lambda U c}{\mu} \tag{4.3}$$

U	**Re**	Re_c **($\lambda = 2.5$)**	Re_c **($\lambda = 3$)**	Re_c **($\lambda = 3.5$)**
8 m/s	**267,000**	66,667	80,000	93,333
9 m/s	**300,000**	75,000	90,000	105,000
10 m/s	**333,000**	83,000	100,000	116,000

Table 4.1: Values of chord Reynolds numbers at different λ for each condition of U in the measurements.

Previous experiments in H-Darrieus [Paraschivoiu, 2002, Howell et al., 2010, Miau, 2012] already detected a considerable raise of performance due to the wind speed increase. This increase is also shown in Figures 4.1a) and b) as the power curve is shifted up when increasing wind speed.

Figure 4.1a) shows the power curves measured in both wind tunnels, for 3 different Reynolds numbers. As explained in previous sections, high blockage modifies the incident wind speed condition, altering turbine ratings. This can be observed in Figure 4.1.a) as values of C_P and λ at VUB wind tunnel (where the correction factor ϵ is larger) are significantly higher. Due to that effect (acceleration of the flow due to blockage) power curves at Re = 267,000 could be only retrieved at VUB but not at CRIACIV.

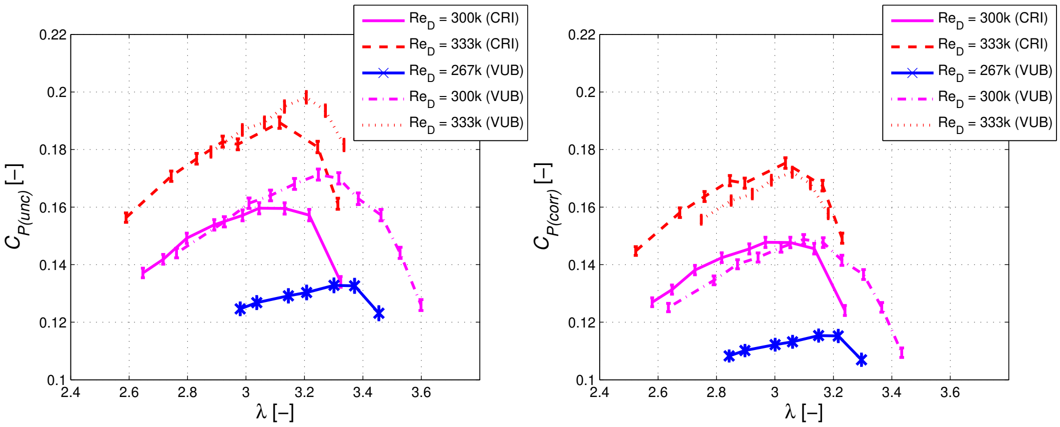

(a) (b)

Figure 4.1: Power curves obtained under different Reynolds number. Uncorrected power curves measured at CRIACIV and VUB wind tunnels (a), and values corrected for blockage using Pope's formula [Pope and Harper, 1966] (b).

In Figure 4.1.b) the Pope's blockage correction [Pope and Harper, 1966] (see section 2.5) is already applied, and it can be seen how the curves coming from both wind tunnels look much more similar. The only remarkable difference is the values at high λ at Re=300,000, but overall it is shown that Pope's correction can be applied to H-Darrieus reasonably. Paying special attention to the optimal operational conditions, the maximum C_P from both wind tunnels converge accurately, which can be seen at Table 4.2. In it, also the C_{Pmax} values measured and corrected are presented, adding also the Maskell correction [Maskell, 1987]. The values are benchmarked with the max C_P measured during another campaign with the same prototype in the large Politecnico di Milano (PoliMi) wind tunnel, were the blockage ratio was only 0.9% [Vergaerde et al., 2018], and therefore, according to the literature no correction is needed [Dossena et al., 2015]. Those tests were done under low turbulence conditions, therefore only those results are analysed.

It becomes clear that the Maskell correction (designed for a Savonius VAWT) highly overestimates the effect of blockage, and therefore is not valid for an H-Darrieus turbine, more porousto the incoming wind. On the

Wind tunnel	ϵ	Re	I_u (%)	C_{Pmax} meas	C_{Pmax} Maskell	C_{Pmax} Pope
CRIACIV	0.10	300,000	0.7	0.160	0.101	0.148
VUB	0.19	300,000	0.5	0.171	0.079	0.149
CRIACIV	0.10	333,000	0.7	0.191	0.120	0.175
VUB	0.19	333,000	0.5	0.198	0.091	0.172
PoliMi	0.01	333,000	2.0	**0.170**	0.163	0.169

Table 4.2: C_{Pmax} values obtained in the various experiments at low turbulence, and the result of applying the blockage corrections presented in section 2.5.

other hand, the Pope correction delivers very satisfactory results in these cases, resulting in small differences ($< 4\%$) between the measurements in the different wind tunnels. What becomes clear too from figure 4.1 and table 4.2 is that the performance of the VAWTs is highly overestimated in small wind tunnels, and therefore Pope's blockage correction is applied to all further data.

Blockage also has an influence on the value of λ due to its inverse proportionality to U. While the λ at the optimal point of operation coincides for Re = 333,000, but not as precisely for Re = 300,000. It is also interesting to point out how this λ_{opt} decreases slightly as Re increases. This effect, although small (from $\lambda = 3.2$ to $\lambda = 3.05$) is linked to the higher angles of attack experienced by the blades at lower λ, which causes dynamic stall [Hohman et al., 2018]. Also, at high Re, the aerofoil is better equipped to cope with stall angles as aerodynamic lift is higher [Amandolèse and Széchényi, 2004].

4.1.2 Turbulence Intensity effect

To compare the power curves obtained under various turbulent conditions, only the measurement obtained with similar grids (VUB grid and CRIACIV grid 1) are plotted. Figure 4.2 presents the values obtained at CRIACIV wind tunnel at Re = 300,000 (a) and Re = 333,000 (b). Figure 4.3 shows the results from VUB wind tunnel.

The main effect of I_u that can be observed in all 4 graphs is a performance increase, as the power curves are shifted up as turbulence rises. The difference between smooth and turbulent flow is larger for low λ, which sug-

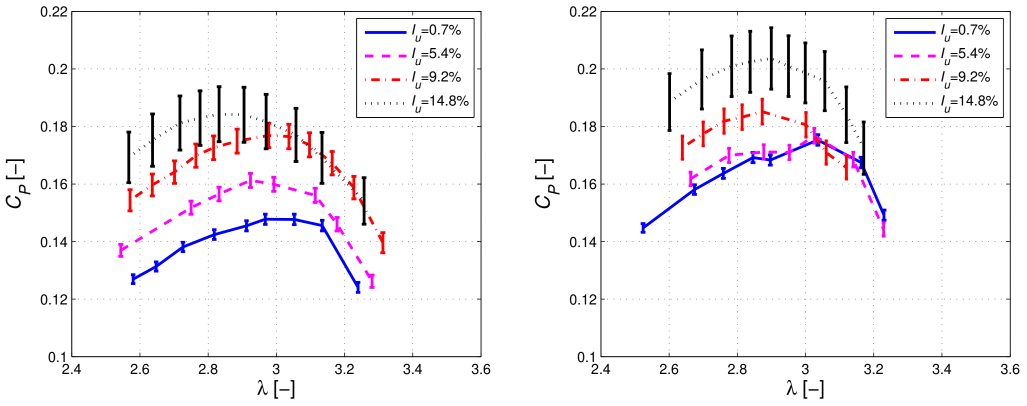

(a) (b)

Figure 4.2: Corrected power curves obtained under different turbulence levels at the CRIACIV wind tunnel, at a Re = 300,000 (a), and Re = 330,000 (b).

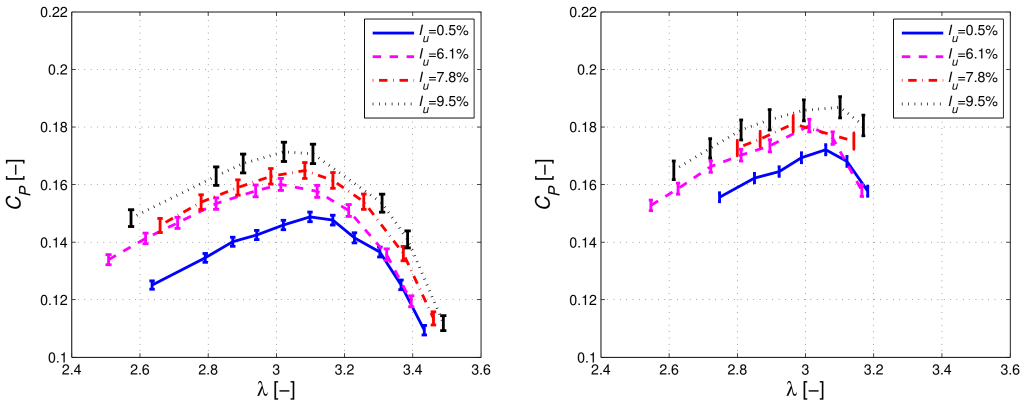

(a) (b)

Figure 4.3: Corrected power curves obtained under different turbulence levels at the VUB wind tunnel, at a Re = 300,000 (a), and Re = 330,000 (b).

gests that it can be related with aerofoil performance. In fact, for low λ the incidence angle of the blades is larger [Paraschivoiu, 2002], so the blade can suffer stall in some part of the rotation. And it has been reported in several studies [Amandolèse and Széchényi, 2004, Devinant et al., 2002, Maldonado et al., 2015] that turbulent flow improves the static and dynamic stall conditions of the aerofoils.

Another contribution to this performance increase is that turbulent flow is more energetic than smooth flow, as the available power depends directly on U^3 (Eq. 1.7). With the same mean wind speed, turbulent flow will have slightly higher power derived from instantaneous higher speeds. Figure 4.4.a shows this fact, by plotting the histogram of the wind power available from the wind speed signal measured at $U = 9$ m/s, at two different turbulent conditions. As seen, the wind at low turbulence has a very narrow power distribution. Meanwhile, when the flow turbulence is increased that distribution is widened (the turbulent case distribution is scaled up 10 times for visualization purposes). The contribution from the high energy winds makes that the average incoming power in the turbulent case is slightly larger (2% approximately, the mean values are represented by the discontinuous lines). However, this effect only accounts for a small part of the C_P increase, as it can be seen in Fig. 4.4.b, where the histogram of the power extracted at the optimal point of operation of the turbine is represented. The power increase registered in this case is around 21%, therefore the main reason of this power boost resides more in the turbine aerodynamics than in the power available. A more detailed explanation of this issue is presented in annex A.2.2.

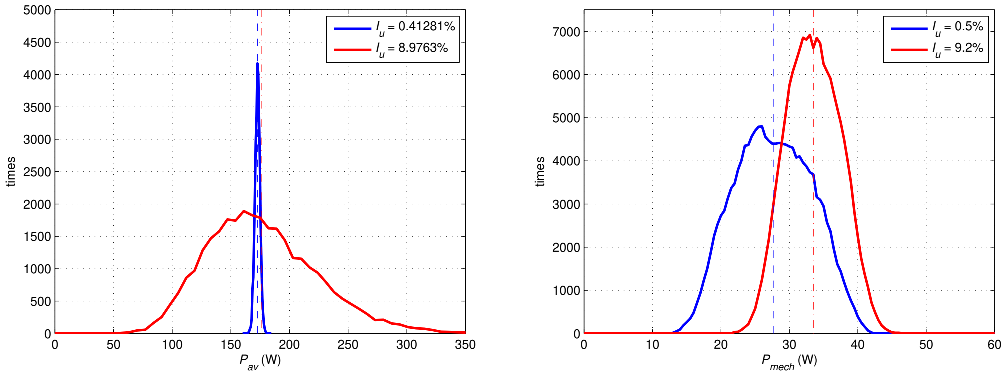

(a) (b)

Figure 4.4: Histograms of the instantaneous wind power available signal at low and high turbulence (amplified 10 times) at $U = 9$ m/s (a), and of the mechanical power extracted by the turbine under those conditions (b).

Comparing the curves under different Reynolds numbers it is clear that the difference between low and high turbulence is lower when Reynolds numbers increase. In fact, there are some points in Figure 4.3.b where the C_P

under smooth flow is similar to some of the low turbulence cases. That could suggest that the effect of turbulence is more evident for low Re. As well as with Reynolds number, also in this case when C_P increases the optimal λ shifts slightly to the left. This effect is also small but could also be related with the stall behaviour of the blades, as under turbulence the blade improves its performance under the high angles of attack present at lowerλ [Amandolèse and Széchényi, 2004]. Overall, it can be concluded that the effect of turbulence can be equivalent to the Re effect, causing an earlier transition to a turbulent boundary layer on the blade: this occurs both when Re increases and/or when I_u increases and results in higher C_P and lower optimal λ.

Finally, it is interesting to explain why the error bars are larger for high turbulence cases, especially in the CRIACIV case (Figure 4.2). Looking at Figure 4.4.b this error source cannot be found in the variability on the power signal. In fact, it is caused because the main contribution to uncertainties is the error in the incoming wind speed (see section 2.6). As it can be seen in the wind profiles obtained with the different grids (Figures 3.10 and 3.12), the uniformity of the wind profiles at high turbulence is lower than in the cases with low I_u, meaning more uncertainty in the incoming U. Nonetheless, even considering the error bars, the trends indicated in previous paragraphs are still clear.

4.1.3 Integral length scale effect

The effect of L_{ux} is evaluated by plotting the power curves from 4 experiments done at CRIACIV wind tunnel using the 2 different grids (see Figure 4.5) at Re = 300,000 (a) and Re = 333,000 (b). The curves in smooth flow ($I_u = 0.7\%$) are compared with one pair of measurements with similar turbulence level ($I_u \approx 5\%$) and different L_{ux} (0.18 m and 0.05 m), and one pair with similar L_{ux} (0.08-0.09 m) and very different I_u (14.8% and 2.5%).

The interpretation of the previous results is different from one figure to another, suggesting Re may have an important influence. Studying the curves obtained under $I_u \approx 5\%$ in Figure 4.5.a (Re = 300,000) the effect of L_{ux} appears only for high λ, while for low λ the curves coincide. The curve with $I_u = 2.5\%$ shows that already with low turbulence, its effects (increase of C_P and decrease of optimal λ) can be appreciated. However, when Re is increased (Figure 4.5.b, Re = 333,000) those effects disappear, as the curves

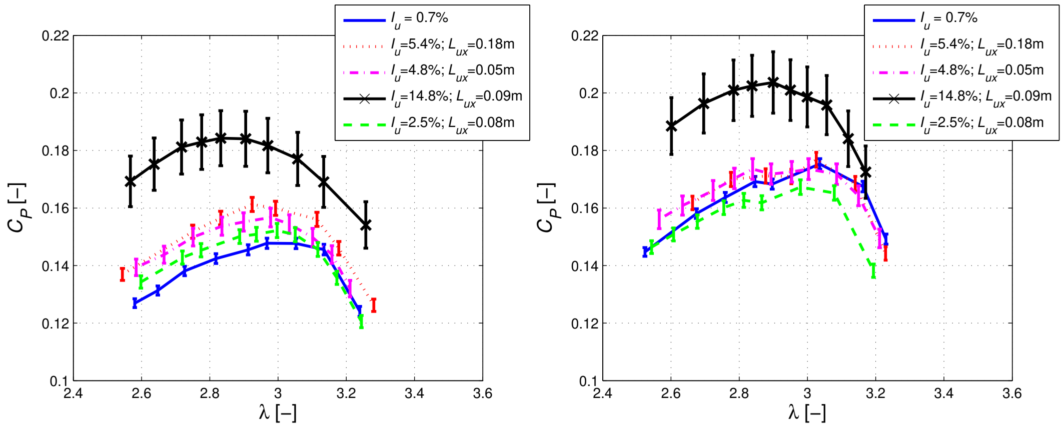

(a)

(b)

Figure 4.5: Power curves obtained under different turbulence and integral length scale levels at the CRIACIV wind at a Re = 300,000 (a), and Re = 330,000 (b).

of $I_u \approx 5\%$ present a behaviour similar to smooth flow for medium and high λ, and the one with $I_u = 2.5\%$ has a maximum C_P lower than the smooth flow case. In this case, the beforementioned effects of turbulence are only evident for large I_u. Above all, in general it is quite clear that the effect of L_{ux} in the power curves is not very relevant compared to that of turbulence seen in the previous section.

4.2 Analysis of the maximum C_P

The previous chapters analysed the influence of Re, I_u and L_{ux} independently in the power curves. To study the mutual influence among the three parameters only the peak C_P of each curve is represented (C_{Pmax}). In order to double-check the accuracy of Pope's blockage correction the values are benchmarked with the C_{Pmax} measured during another campaign with the same prototype in the large Politecnico di Milano (PoliMi) wind tunnel, where the blockage ratio was only 0.9% [Vergaerde et al., 2018], and therefore, according to the literature no correction is needed [Battisti et al., 2016].

Figure 4.6 shows the maximum C_P of all the curves previously presented, applying the aforementioned correction, plotted against the turbulence intensity at each measurement. The values appear to be distributed among three groups, each depending of a Reynolds number, with no remarkable difference between the data coming from both wind tunnels. Also, the value from PoliMi wind tunnel seems to fit in the trends observed for the similar Re. Data suggest a linear increase of C_{Pmax} with I_u, therefore these trend lines can be defined by Equation 4.4, where C_{Pmax0} represents the C_{Pmax} value at $I_u = 0\%$ and S the slope of the function.

$$C_{Pmax} = C_{Pmax0} + S \cdot I_u \tag{4.4}$$

This graph reveals that the influence of turbulence is definitely positive for the turbine peak performance, as there is a positive quasi-linear dependency between C_{Pmax} and I_u, at least in the range studied. This is exposed in Table 4.3, where the parameters of each line are presented, as well as the coefficient of determination R^2 of this linear fit. It is clearly visible how the slope S of the line decreases significantly as Re rises, meaning that the rotor is less sensitive to turbulence as Re increases. At the same time, the data also tells that the difference of performance between the three Re levels is lower as I_u increases. This effect is observed at all turbulence levels for the lower Re (267,000 and 300,000) while at Re = 333,000 the effect is only clear when $I_u > 5\%$ and at lower levels of turbulence the linear trend seems to flatter. This fact is expressed in the lower coefficient of determination R^2 obtained for that Re case.

Re	C_{Pmax}	slope S	R^2
267,000	0,113	0,0036	0,986
300,000	0,146	0,0027	0,960
333,000	0,167	0,0022	0,869

Table 4.3: Parameters of the trend lines obtained for the relation C_{Pmax} - I_u at each Reynolds number.

A similar reasoning can be done with the influence of Re in the power curves. Figure 4.7 shows the maximum C_P of all the curves previously presented, applying the aforementioned correction, plotted against the Reynolds number of the incoming flow at each measurement. The values are grouped among the measurement with similar values of turbulence (I_u ± 1%), as in

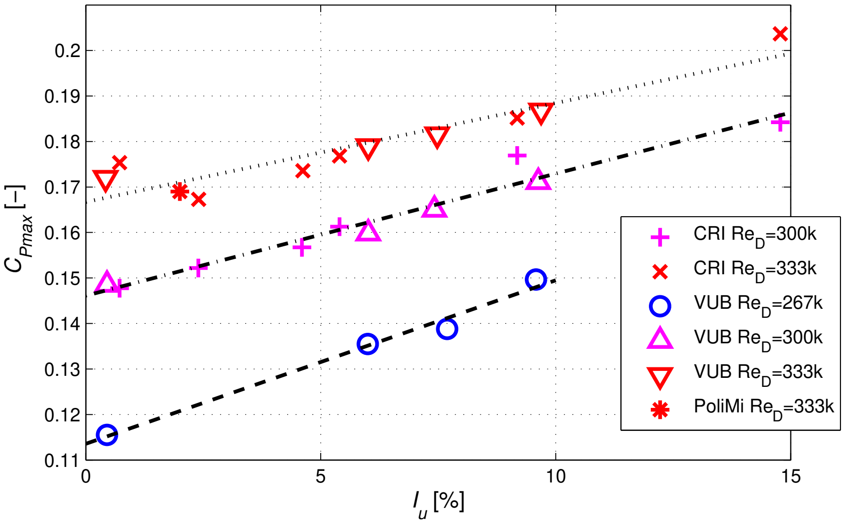

Figure 4.6: Maximum C_P obtained in the different experiments, applying in all cases Pope's correction. The trendlines show the linear fit for the experiments done at each Reynolds number.

the previous figure it was seen that there was no remarkable difference between the data coming from both wind tunnels. As in the I_u case, the trend lines can be defined by the linear equation Equation 4.5, where S_2 is the slope of the function and C_0 a constant.

$$C_{Pmax} = C_0 + S_2 \cdot \mathrm{Re} \tag{4.5}$$

In this case, trend lines are only calculated for the I_u groups with more than three measurements for statistical accuracy, which are $I_u = 0\%$, 5% and 9%. As for turbulence, the effect of Reynolds number is also positive for the turbine peak performance, as there is a positive quasi-linear dependency between C_{Pmax} and Re, at least in the range studied. This is exposed in Table 4.4, where the parameters of each line are presented, as well as the coefficient of determination R^2 of this linear fit. Parallelly to Figure 4.6, here it can be seen how the effects of Re and I_u are reduced as both factors increase, which is clear as the slope S_2 is lower for the higher I_u. The main difference between the two figures, is that in Figure 4.7 the three trends seemed to continue after the range studied ($I_u > 15\%$), while in Figure 15 the trends seem to converge not far after the maximum Re studied (Re ≈

350,000). This fact is relevant, and it means that, even turbulence and Re have both a positive effect in C_{Pmax}, while Re still increases C_{Pmax} for values of $I_u > 15\%$, when Re $> 400{,}000$, it seems the turbulence would not affect the C_{Pmax} values anymore. Assuming an optimal $\lambda = 3$, this would be translated to a $\mathrm{Re}_c > 120{,}000$.

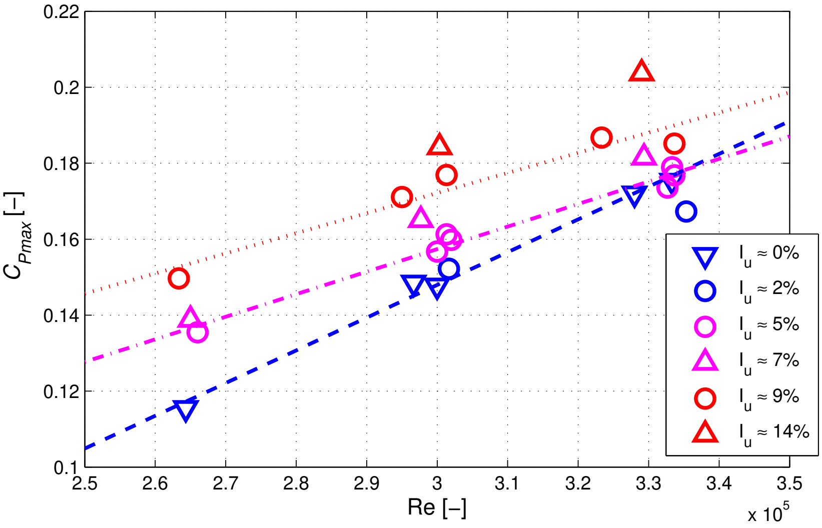

Figure 4.7: Maximum C_P obtained in the different experiments in function of Re, applying in all cases Pope's correction. The trendlines show the linear fit for the experiments done at similar turbulence numbers.

I_u ($\pm$ 1%)	C_0	slope S_2	R^2
0%	-0,111	$8,62 \cdot 10^{-7}$	0,993
5%	-0,021	$5,94 \cdot 10^{-7}$	0,980
9%	0,133	$5,29 \cdot 10^{-7}$	0,937

Table 4.4: Parameters of the trendlines obtained for the relation C_{Pmax} - I_u for each turbulence level.

In Figure 4.8 this process is repeated for L_{ux}. Here the values are grouped according to their Reynolds number and divided among three values of I_u: low ($2\% < I_u < 6$ %), medium ($6\% < I_u < 9\%$) and high ($I_u > 9\%$). The values of free stream are not represented here as the turbulence content was too high to calculate L_{ux}. But in this case no clear trends are observed; the points with higher C_{Pmax} are all related with high Re (red points) and high I_u, and no apparent effect of L_{ux} is observed. Therefore, no linear trends or whatsoever are calculated for this case.

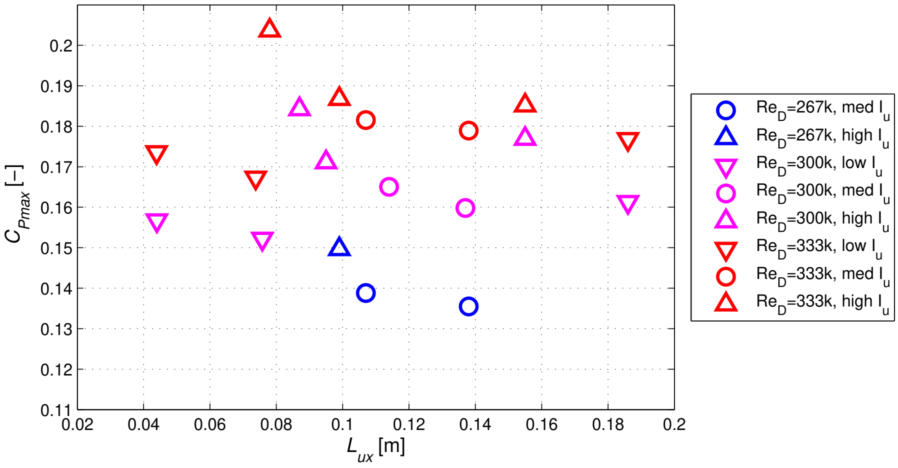

Figure 4.8: Maximum C_P obtained in the different experiments in function of L_{ux}, applying in all cases Pope's correction. The values are grouped according to their Reynolds number and approximate level of I_u.

4.3 VAWT tests at VKI

A short campaign of testing was done also with the in-house turbulent conditions at VKI (subsection 3.3.4). The large size of the wind tunnel allows to generate heavily sheared flows with high levels of I_u and specially L_{ux} that could not be reached in middle-sized wind tunnels as the VUB one or the CRIACIV (Fig. 4.9).

However, several problems arose when testing the VAWT prototype at VKI. First, the wind profile generated with the pre-defined conditions delivered a mean U in the span of the rotor of 10.87 m/s, much higher than the previous wind curves, where the maximum U is 10 m/s. That was why the wind tunnel speed had to be reduced. But when experiments where reproduced at Re of the range of 300,000, the turbine experienced abnormally high levels of vibrations that could not be reduced in the days of the campaign. Figures 4.10 a and b show the time histories of the recorded ω and Q in the

Figure 4.9: VAWT model placed in the VKI wind tunnel test section. The cups for generating the in-house turbulence profiles are seen in the background.

VAWT power curves from the VKI experiments (a) and a case with similar U and I_u from the VUB wind tunnel measurements (b). The VKI graph shows a lot more of variations in the Q measure from the torque-meters, and also a more limited range of ω where the turbine could be operated.

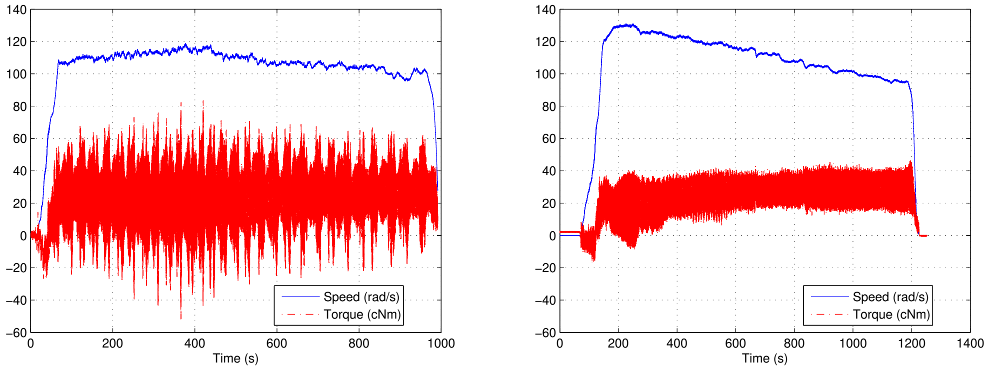

(a) (b)

Figure 4.10: Examples of time histories of the ω and torque measurements from experiments at VKI (a) and VUB (b)

Those difficulties in the operation of the turbine were translated onto the impossibility of retrieving reliable power curves. The rotational speed could not be maintained in the ranges set in section 4.1 to obtain stable conditions, and even without that, the recorded C_P was inferior to 0.14 (way lower than in the other measurements). One could think that this fact was due to the wind shear, or the increased L_{ux}; however that effect could not be detected in the blade aerodynamics under this condition, studied in section 6.3. The loss of power due to the increased vibrations is, therefore, the main candidate for this poor performance of the VAWT at VKI. In fact, due to physical constraints, the support box had to be attached on the structure of the wind tunnel (see Figure 4.11) instead of directly on the ground, as it was in the other wind tunnels (Fig 2.9). At the VKI case, then, the turbine was not isolated from the wind tunnel vibrations, and those could have affected its operation.

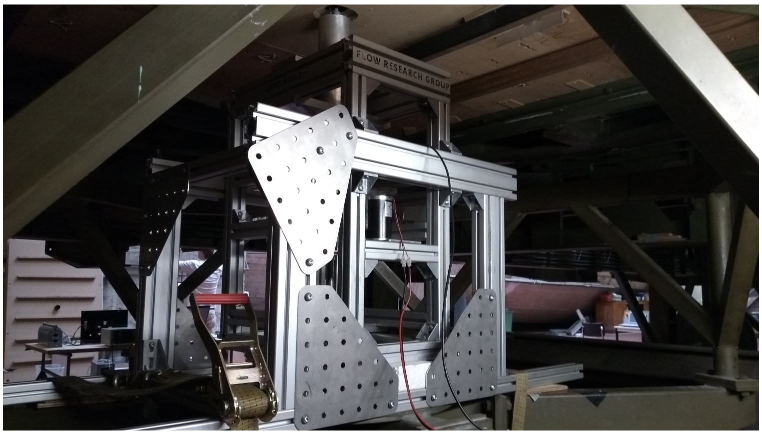

Figure 4.11: VAWT support structure placed under the VKI wind tunnel test section. The box was fixed to the wind tunnel beams by straps.

4.4 Comparison with numerical results

Within the scope of the Aeolus4Future project, the PhD student Abdolrahim Rezaeiha from Eindhoven University of Technology performed a study similar to the present, but using Computational Fluid Dynamics. By modelling a VAWT slightly larger than the one in this project ($H = 1$ m, $D = 1$ m) he also studied the impact of turbulence on the VAWT power curves. It was considered meaningful for this study to compare with A. Rezaeiha CFD results [Rezaeiha et al., 2018] before drawing the conclusions of this chapter. The power curves in their study were obtained at higher Re_c (103,000 to

214,000) and are presented in Figure 4.12. Their study considered incoming turbulence values from 0 to 30%, while L_{ux} was fixed at 1 m.

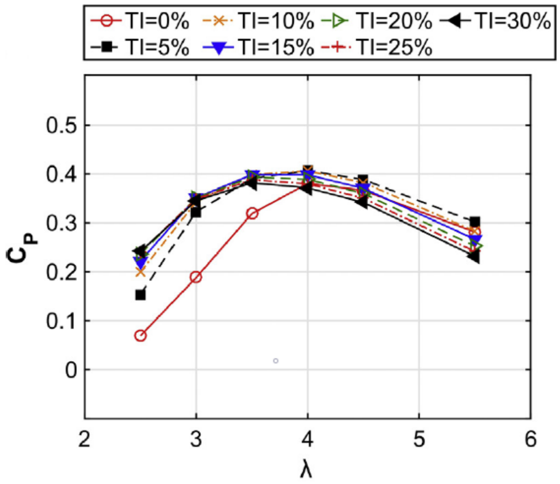

Figure 4.12: Power curves for different I_u obtained in the numerical study by A. Rezaeiha [Rezaeiha et al., 2018].

There are two main differences between their curves and our experimental results. The first is the C_P levels obtained; in their 2-D CFD simulations, neither the mechanical losses, the drag caused by the struts nor the tip effects were calculated, therefore the overall power coefficient is much higher. The higher Re_c also contributes to this difference, as well as to the higher λ_{opt}. Apart, comparing our C_P values with literature, they are already rather low due to the reduced size of the rotor (SANDIA's prototype tests reached $C_P > 0.3$ [Paraschivoiu, 2002]). Another reason for the overall low efficiency of our experimental data is the lack of a tracking system (like a MPPT) that allows the turbine to remain automatically at its best operative point.

The second difference is that the impact of turbulence on C_{Pmax} calculated by A. Rezaeiha is much more limited, and only evident for the I_u = 0% case. In fact, for high λ they even show that that further increases of turbulence over 15% actually decrease performance, which they relate to increased skin friction. This difference in behaviour could be explained by the higher Re_c in the CFD simulations, as in section 4.2 it was already suggested that the I_u effect seemed to fade for $\mathrm{Re}_c > 120{,}000$.

According to Rezaeiha et al., the impact of turbulence is only positive for low λ, which they also relate with the promotion of laminar-to-turbulent transition and a considerable delay in stall on the blades [Rezaeiha et al., 2018]. To illustrate this fact, Figure 4.13 presents the C_P - I_u relation not only for λ_{opt} (as it was done in section 4.2), but also for lower and higher λ levels. The results from A. Rezaeiha simulations and from our experiments are plotted together, normalizing the C_P with the highest value in each set of results.

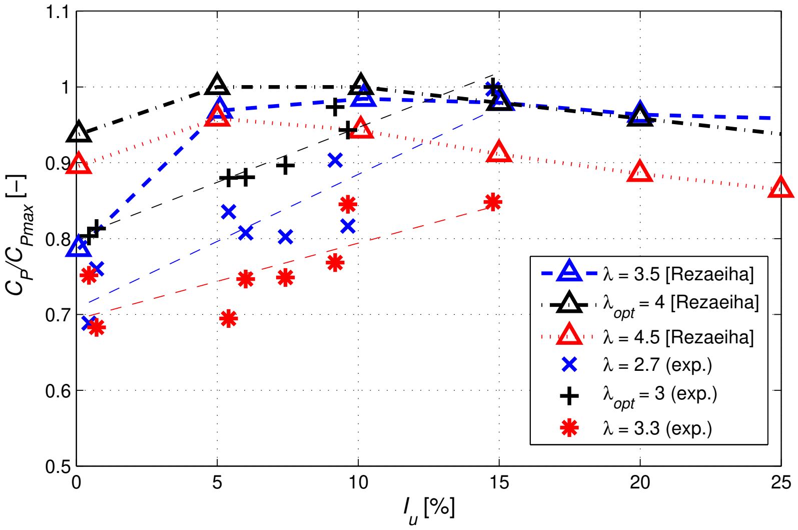

Figure 4.13: C_P/C_{Pmax} - I_u curves at different λ from the numerical study by A. Rezaeiha [Rezaeiha et al., 2018] and from our experiments (with linear trends).

The two sets of results agree in the fact that increasing λ reduces the effect of turbulence, and at the experimental results it can be observed how at $\lambda = 3.3$ C_P stops increasing at $I_u = 15\%$. While the CFD simulations indicate that the optimal I_u operation point it is between 5 and 10%, this is not found in the experiments, as C_{max} is registered at the maximum $I_u = 15\%$. This difference indicates that there could be an optimal operation I_u value depending on Re. Further testing with a larger prototype is advised in order to study this fact.

4.5 Discussion of the results

As a conclusion, the experimental results have found a significant, linear increase of the H-Darrieus performance with turbulence intensity I_u for low Reynolds numbers. This effect has been proved upon the same turbine in two different wind tunnels. This fact can be justified by several reasons:

- Stall of the blades: turbulence has been proven to enhance transition on the flow over the blade, which causes a significant delay on the stall in blades. This could be an important advantage in H-Darrieus, where the blade is stalled in an important part of the rotation, especially at low λ [Paraschivoiu, 2002, Amandolèse and Széchényi, 2004].
- Lower losses due to the shaft: In low Re, increased turbulence also reduces the drag in cylinders, which in this case will supposes less losses due to the turbine shaft. This fact has been proven lately both experimentally (see chapter 5) and numerically [Rezaeiha et al., 2017].
- Faster wake recovery: Turbulent flow also might enhance wake recovery, decreasing the influence of the upstream blade in the downstream one. This fact, suggested by Dabiri [Dabiri, 2011] has been also measured in this same prototype (chapter 5).

The comparison with numerical studies performed at higher Re suggests that this positive effect of I_u could fade for higher values of turbulence and Re. The measurements on a third wind tunnel (VKI) were compromised due to excessive vibrations on the turbine structure. That stresses the fact that a careful structural study of the turbine, and successful isolation from external vibrations, is compulsory in order to operate efficiently a VAWT.

Chapter 5

Measurement of a VAWT wake under turbulent flow

5.1 Objectives of the experiment

The scope of the present study is to expand the knowledge on the effect of turbulence on a Darrieus VAWT, with special focus on the near wake of the turbine, which was recently shown to be of particular interest to understand the origin of flow macro-structures related with the blade-flow mutual interaction [Bianchini et al., 2017b]. Regarding the effect of turbulence on the wake, a previous study [Peng and Lam, 2016] on a 5-bladed rotor detected large asymmetries and differences in the wake from smooth to turbulent flow. A study on a 3-bladed Darrieus under smooth flow and ABL flow [Hohman et al., 2018] did not register a great effect on the wake, but suggested that turbulence decreases the strength of the dynamic stall and enhances the momentum recovery in the turbine wakes, as had been recorded for open terrain measurements [Dabiri, 2011].

With the set-up previously described at CRIACIV wind tunnel, the two-bladed H-Darrieus rotor was exposed to different turbulence conditions, and the near-wake characteristics were measured with the traverse system presented in Figure 2.5. That system, described at subsection 2.2.3, allowed to scan the turbine wake at a downstream distance of $x = 1.5R$ (37.5 cm). Two horizontal velocity profiles were measured, one at height $0.5H$ (midplane of the rotor) and one at $0.86H$ (to avoid the influence of the shaft or tip effects in the wake) (see Figure 5.1).

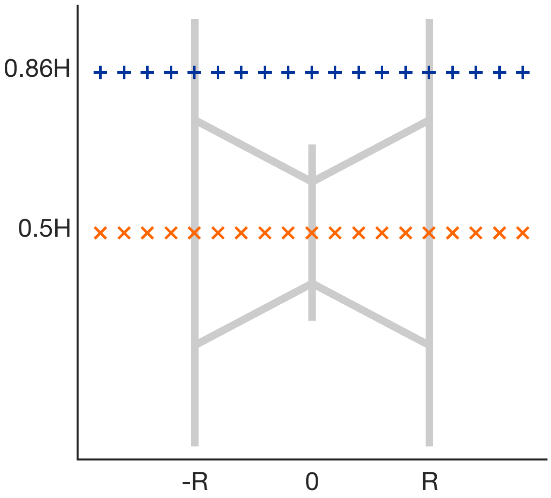

Figure 5.1: Positions of the two measured velocity profiles 0.75D behind the rotor [Vergaerde et al., 2019].

The incoming wind speed was set at $U = 9$ m/s during all tests, and the rotational speed was maintained at $\lambda = 3$ as it was the best operational point for the VAWT prototype, resulting in a mean chord-based Reynolds number of around 90,000. Experiments were carried out in four different turbulence conditions to discriminate the effect of I_u and L_{ux} (Table 5.1). Grid CRI 1 was used to create medium and high turbulence levels while one test was also done with smaller grid CRI 2 in order to get an impression of the effect of L_{ux}.

Condition	**Grid**	**grid distance x**	**mean I_u**	**mean L_{ux}**
Smooth flow	none	-	0.7%	-
Low I_u	CRI 1	7.6 m	5.4%	0.18 m
High I_u	CRI 1	3.75 m	9.2%	0.15 m
Low I_u, low L_{ux}	CRI 2	2.1 m	4.6%	0.04 m

Table 5.1: Description of the different tests conditions in which the VAWT wake was measured.

As comparison and validation, this work was done parallelly to the team led by Prof. Ferrara of the Dept. of Industrial Engineering at the University of Florence, who at their time were studying the turbine wake and flow field using numerical simulations. Since direct spatially-resolved and comprehensive maps of the flow field (e.g. with particle image velocimetry) were not available, dedicated numerical simulations using U-RANS computational fluid dynamics (CFD) were carried out to identify of the main aerodynamic phenomena and flow macro-structures, whose traces are registered in the wake. This kind of simulations, if the proper levels of spatial and temporal refinement are provided [Balduzzi et al., 2016], recently showed to be able to accurately reproduce the aerodynamics of Darrieus blades [Bianchini et al., 2017a].

Those simulations were carried using the commercial software ANSYS FLUENT, using the k-ω SST model for turbulence closure, and coupled with the Enhanced Wall Treatment embedded in the FLUENT code for the computation of the boundary layer in the near-wall regions. The coupled algorithm was chosen for pressure-velocity coupling, and the 2nd order upwind scheme was adopted for both RANS and turbulence equations. Inlet air conditions were the same as monitored during the experimental tests. To simulate the rotation of the turbine, the sliding mesh technique was employed. The mesh was of unstructured and hybrid type, with triangular elements in the core flow region, and an O-grid made of quads in the boundary layer. The expansion ratio for the growth of elements starting from the surface was kept below 1.1 to achieve good mesh quality, ensuring a y+ constantly < 1. The airfoil surface was discretized with 1400 nodes. In order to limit the Courant Number in proximity of the blades, an angular timestep of 0.25° was used for the tip-speed ratios in the left-hand side of the curve, increasing to 0.40° in the right-hand side. The required number of revolutions to achieve a periodic solution was variable between 15 and 25 revolutions.

5.2 Study of effect of turbulence on the VAWT wake

5.2.1 Mean wind speed profiles

One of the main focus of the study of the turbine wakes is the wake recovery, or how the wind speed behind the wake returns o the free stream values. This is a key aspect for wind farms, where as fast the wake recovery, the closer together we could place the turbines and increase the overall power density of the installation [Dabiri, 2011]. In this study, the wake profiles could only be taken at the near wake ($x = 1.5R$) due to time and space limitations. The results are presented in terms of normalised velocity with the unperturbed velocity (Figure 5.2), at the mid plane of the VAWT (a) and near the upper tip of the blades where the effect of the shaft is reduced (b). The velocity deficit is represented for each turbulence condition explained in Table 5.1, and the arrow shows the incoming wind speed and the turbine sense of rotation to distinguish the advancing and retreating blades.

In general, the effect of turbulence is not so evident in the wake shape; it seems to result only in a reduced speed deficit. In Figure 5.2.a) the lowest velocity is registered behind the shaft, where the wind speed in smooth flow drops to the 20% of the free stream, while in the high turbulence case the wind speed only drops to 30% of it. The intermediate turbulence cases appear in the middle. This would seem in conflict with the higher energy extraction made by the rotor, but can be explained if one considers that the turbulent flow is thought to promote a faster dissipation of the wake itself due to the more intense mixing with the surrounding wind stream, a fact that has been measured in several VAWT experiments [Peng and Lam, 2016,Hohman et al., 2018] and has been also detected in HAWT [Porté-Agel et al., 2019]. In fact, the numerical simulations of Rezaeiha et al. show both the increase in turbine performance and faster wake recovery for incoming turbulent flow [Rezaeiha et al., 2018]. As in previous analyses, there is no evident effect of the free stream L_{ux}.

Figure 5.2.b) presents a similar behaviour of the wind flow regarding the incoming turbulence. However, due to the absence of the shaft in this position, the velocity deficit is not so pronounced: the minimum U values appear between 30 and 40% of the free stream speed. In both cases, the wake is more pronounced towards the right side, where the blade is facing the flow. The measurement uncertainty, considering random and propagation errors (as calculated in section 2.6), is about 4% of the free stream wind speed, and it is not presented in these graphs for clarity.

In Figure 5.3 the experimental values for the smooth flow case are also compared to CFD simulation results of this same prototype [Carbó Molina et al., 2018]. The wake shape was also compared with data from the most similar experiment found in literature. Tescione et al. performed PIV measurements at $1.5R$ downstream of a 2-blade NACA0018 H-Darrieus at

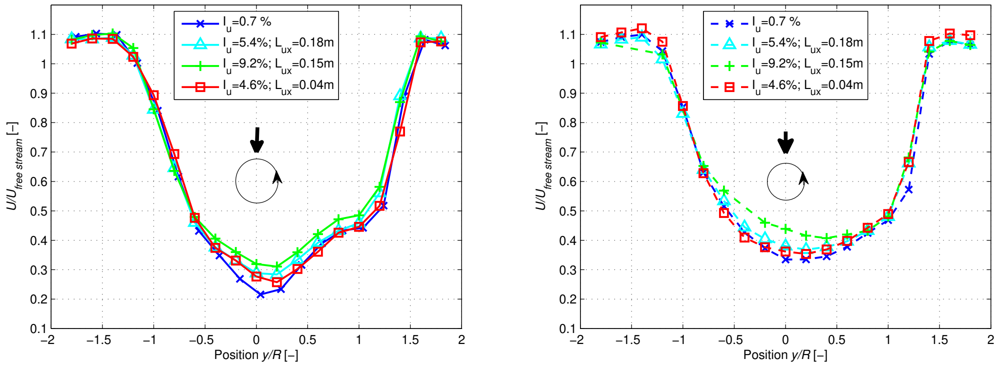

(a) (b)

Figure 5.2: Horizontal normalized wind speed in the wake of the VAWT under different turbulence conditions, taken at $y = 0.5H$ (mid-plane of the rotor, a) and $y = 0.86H$ (b).

similar Reynolds numbers but higher λ (4.5 versus the present value of 3.05) [Tescione et al., 2014]. This difference might explain the more pronounced wake shape for low λ, also observed in other studies [Bianchini et al., 2017b]. The radial extension of the wake and the velocity levels downstream of the turbine are anyhow in fair agreement.

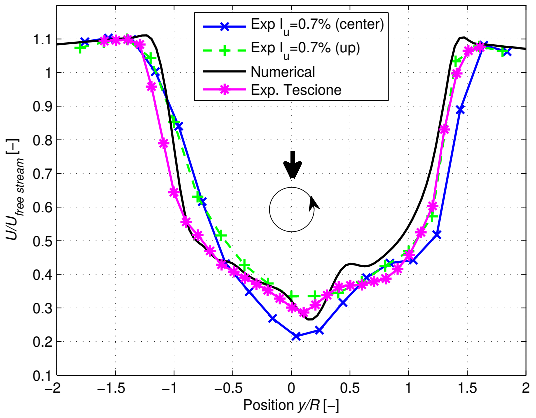

Figure 5.3: Comparison of the experimental and numerical wake wind speed, with experiments from Tescione et al. [Tescione et al., 2014].

5.2.2 Turbulence intensity and unsteadiness

Turbulence intensity (Eq. 1.1) gives a value for the variability of the speed signal in the wake. It indicates the interaction of the wake with the smooth flow, and the obstacles present (shaft, blades) but it can also help identifying the areas where stall phenomenon happen. Figure 5.4 describes the turbulence intensity measured at different levels of turbulence, at height $0.5H$ (a) and $0.86H$ (b) of the rotor. Measurement uncertainties for I_u values are of the order of 0.3%.

Apart from a shift towards positive y/R (visible also in Figure 5.2) due to the deflection of the wake, 3 different zones in the wake can be identified. The more important peak is at y/R = -1, turbulence coming from the retreating blade, and at y/R =1.5 an equivalent peak, but narrower, comes from the advancing blade. A spectral analysis of the velocities revealed that the standard deviation originates from harmonic variations at 1P and 2P frequencies. Although vorticity could not be measured in our setup, the presence of harmonic components in the wake are quite suggestive of the occurrence of dynamic stall. The fact that those external I_u peaks at the sides of the wake are more pronounced for high incoming turbulence, also means that in those regions energy exchange is higher, which can result in faster wake recovery.

An increase near $x/R = 0.5$ is specially visible in Figure 5.4.a), which is coming from the wake of the shaft and is not as evident in Figure 5.4.b) outside its influence. An interesting fact about this central turbulence peak in the mid-plane is that it appear to be dimmed with the increase of the incoming turbulence, suggesting that the shaft effect is reduced with I_u, a fact already proved numerically [Rezaeiha et al., 2017].

Figure 5.5 compares the smooth flow measurements with the computational simulations from [Carbó Molina et al., 2018], which were simulated in 2D considering the shaft, therefore comparable with the central profile. As one may notice, the shape of the turbulence distribution is correctly predicted by the numerical calculations, with one large peak at $-R$, a lower one at $+1.4R$ (edges of the wake), and a third one representing the wake of the shaft.

In those simulations carried out by the team of Prof. Ferrara, also the vorticity maps were simulated. Figure 5.6 represents the non-dimensional vorticity (Eq. 5.1) field when the blade is at the azimuthal position of 160°.

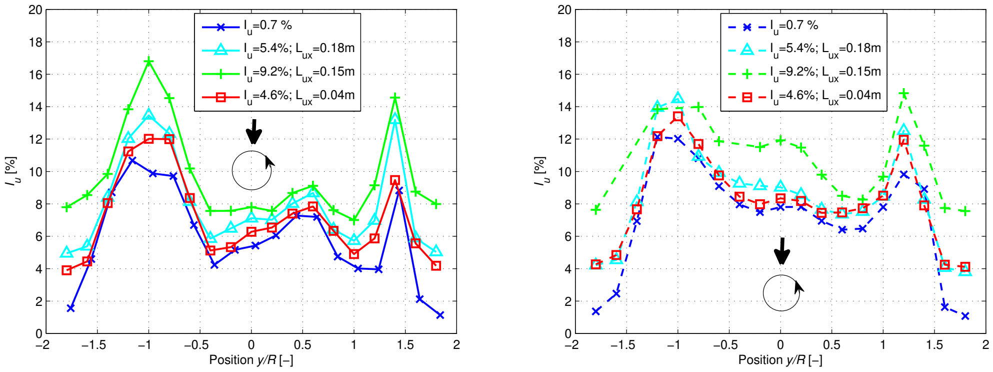

(a) (b)

Figure 5.4: Turbulence intensity measured in the near wake under different turbulence conditions, taken at $y = 0.5H$ (mid-plane of the rotor, a) and $y = 0.86H$ (b).

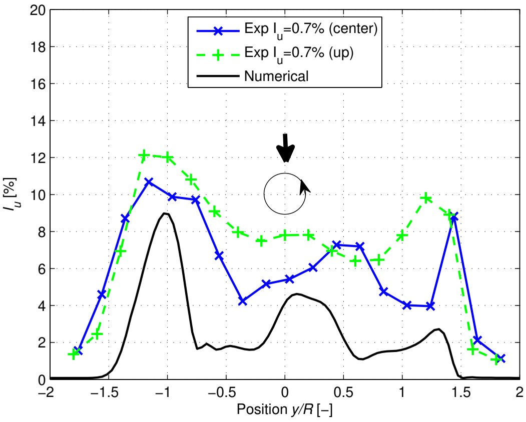

Figure 5.5: Turbulence intensity measured in the near wake at smooth flow ($I_u = 0.7\%$), compared with the numerical simulations from [Carbó Molina et al., 2018].

At this position the incidence is very low so no separation should be expected (in a static case). But the flow is still strongly detached, implying that the blade is suffering from dynamic stall.

$$\Omega^* = \frac{\frac{\mathrm{d}U_y}{\mathrm{d}x} - \frac{\mathrm{d}U_x}{\mathrm{d}y}}{U \cdot c} \tag{5.1}$$

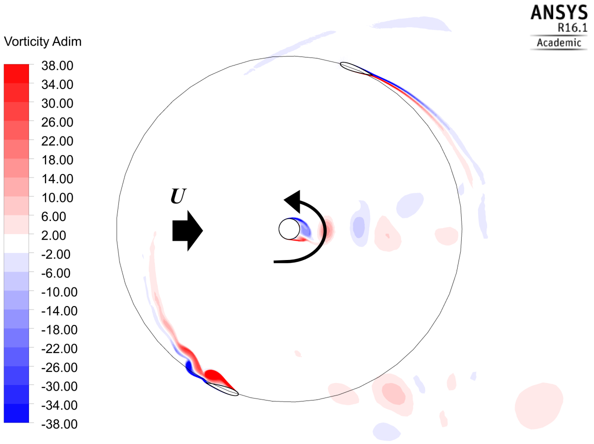

Figure 5.6: CFD simulation of the vorticity field when the blade is at the azimuthal position of 160 ° , from [Carbó Molina et al., 2018].

Based on these insights, it can be hypothesized that the main reason why macro-turbulence has a positive impact on the performance of a H-Darrieus VAWT is the improvement of the boundary layer stability on the aerofoils, leading to a delayed onset of stall conditions (in terms of azimuthal position along the revolution) and then to different shed vorticity downstream. In particular, the increase of the turbulence intensity in the wake is less intense for the high-turbulence case in comparison to the mean turbulence levels, even if experiments clearly highlighted that, when increasing the free stream turbulence, the graph is basically shifted upwards (the free stream turbulence is not modelled numerically).

To complete the analysis, the concept of periodic unsteadiness (I_{per}), originally described in [Bianchini et al., 2017b], was used. The I_{per} tries to identify those flow structures that are mostly periodic during the revolution, i.e. directly correlated to specific positions of the blade. The phase-resolved velocity (U_{per}), Eq. 5.2) is the ensemble average among values acquired at the same phase for all the different revolutions, purged by the time-mean value.

$$U_{per}(\theta, y) = \frac{\sum_i^{N_b}(U(\theta, i, y) - U_{mean}(y))}{N_b} \tag{5.2}$$

where y is the position in the wake, θ the phase and N_b the number of blade passings. I_{per} gives, then, the information of the wake character as the root mean square of that value (Eq. 5.3):

$$I_{per}(y) = \sqrt{\frac{\sum_{\theta}^{N_p}(U_{per}(\theta, y))^2}{N_p}} \tag{5.3}$$

where N_p is the number of phases θ. Figure 5.7 shows the difficulty of phase-resolving experimental data where rpm was not perfectly constant, but two regions of high periodic unsteadiness are clearly identifiable (for all levels of turbulence) between $1R$ and $1.5R$ at both sides of the wake. The numerical simulations show good agreement with the experimental data, and for high λ higher values appear towards the external boundaries of the wake [Bianchini et al., 2017b], not due to vortices but to flow variability in the shear layer between the turbine wake and the undisturbed flow. The variability of I_{per} for increased levels of turbulence further corroborates the hypothesis that the oncoming turbulence strongly impacts the location of stall on the aerofoils, and then on the vortical structures that are detached from the aerofoils and convected downstream.

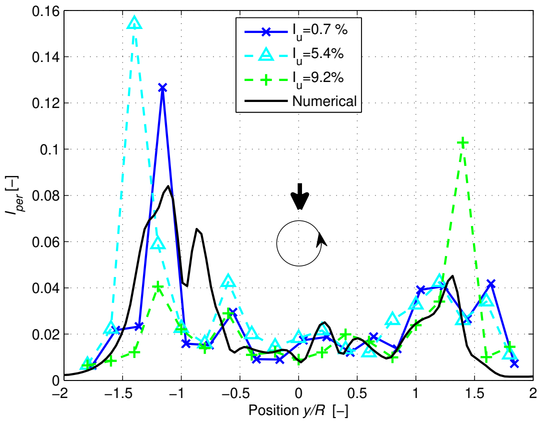

Figure 5.7: Wake periodic unsteadiness calculated from the experimental data at different I_u, compared with numerical simulations from [Carbó Molina et al., 2018].

5.3 Spectral analysis of the turbine wake

A spectrogram of the wake velocity data is also presented to try to provide more information of the VAWT wake and the influence that turbulence has in it. The results are shown in a 3D graph, where the two horizontal axes represent the different measurement positions along the wake (y/R) and the frequencies from 0 Hz until 40 Hz (which is a little higher than the double of the VAWT rotation frequency, approximately 17.7 Hz at $\lambda = 3$). The power spectral density (PSD) of the longitudinal wind speed signal obtained with the *fft* Matlab function is presented in the vertical axis. The results show only until twice the rotation frequency as no relevant information appeared at higher f. Figures 5.8 and 5.9 show the spectrograms for all the measurements taken under smooth flow ($I_u = 0.7\%$) at the mid plane of the rotor and near the top tip.

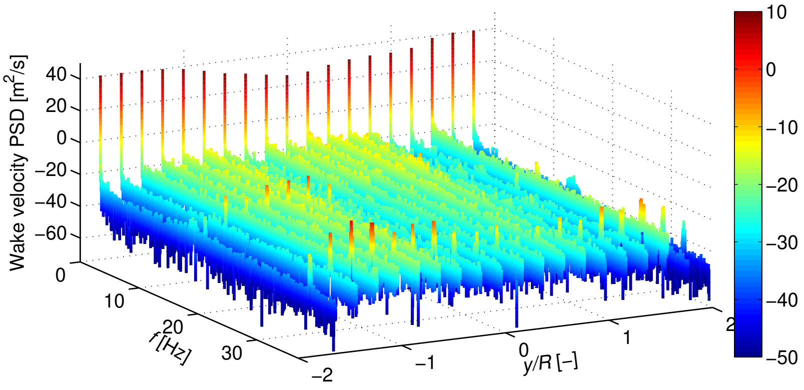

Figure 5.8: Spectrogram of the longitudinal wind velocity measured in each wake position, for a $I_u = 0.7\%$ and at $z = 0.5H$.

The first look at the spectrograms reveal that the blade passage (twice the rotation frequency, at around 36 Hz) is clearly visible for all crosswise locations, which is consistent with the previous studies in literature [Brochier et al., 1986, Araya et al., 2017] that indicate that the blade passage creates a periodic disturbance everywhere, specially in the near wake, which is the present case. In both graphs also a small peak is visible in the left side (retreating blade) at approximately 18 Hz, which corresponds to the turbine rotation frequency. This indicates an asymmetry between the two rotor blades, a fact that has been measured also experimentally during the prototype testing phase, as described in [Vergaerde et al., 2019]. The asymmetric peak could be related stronger stall vortexes occurring in one of the two blades.

Between the two profiles, the main difference is that the flow is slightly

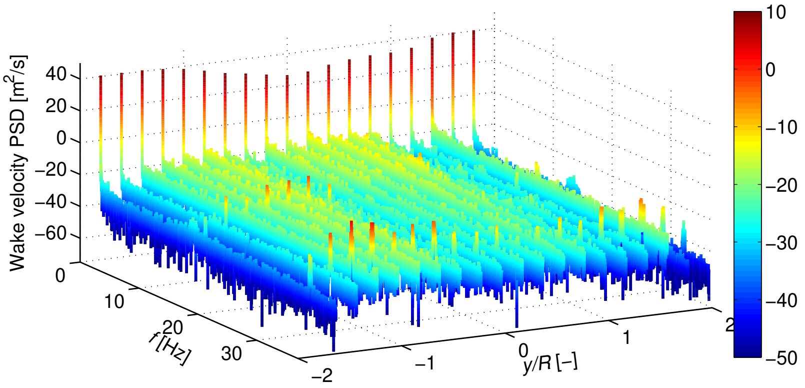

Figure 5.9: Spectrogram of the longitudinal wind velocity measured in each wake position, for a $I_u = 0.7\%$ and at $z = 0.86H$.

more energetic in the upper measurement (Figure 5.9), a fact that could be identified already in Figure 5.5, as I_u is slightly higher in the upper position. It is also interesting to point out how the DC signal (at $f = 0$ Hz) corresponds to the U wake profiles presented in subsection 5.2.1.

Figures 5.10 and 5.11 show the same measurements taken at the mid-plane of the rotors but for the cases of medium ($I_u = 5.4\%$) and high ($I_u = 9.2\%$) turbulence. Apart form the higher energetic content, the fact that draws more the attention is that for high turbulence the peak at 18 Hz that represented the blade asymmetry is not visible. That would mean that with higher levels of incoming turbulence, the stall conditions of the two blades are the same. As it will be discussed in the upcoming Chapter 6, for high levels of incoming I_u it is possible that the blade does not enter in stall at any point of the rotation, which would explain why the asymmetry in the blade stall is only present for low turbulence flows.

5.4 Discussion of the results

The study of the near wake ($1.5R$ downstream the turbine) in turbulent conditions tried to find an explanation for this performance rise, and to increase the understanding of the inner flow physics. Wind speed measurements showed faster wake recovery for turbulent flows, as the wind speed drop was 10% lower than in smooth flow. The shape of the wake in that position

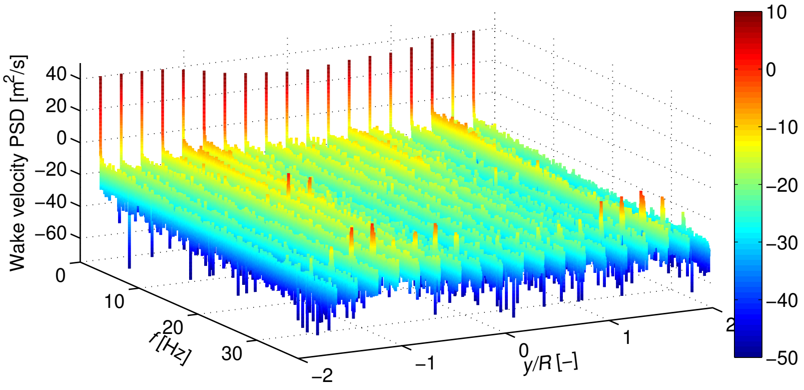

Figure 5.10: Spectrogram of the longitudinal wind velocity measured in each wake position, for a $I_u = 5.4\%$ and at $z = 0.50H$.

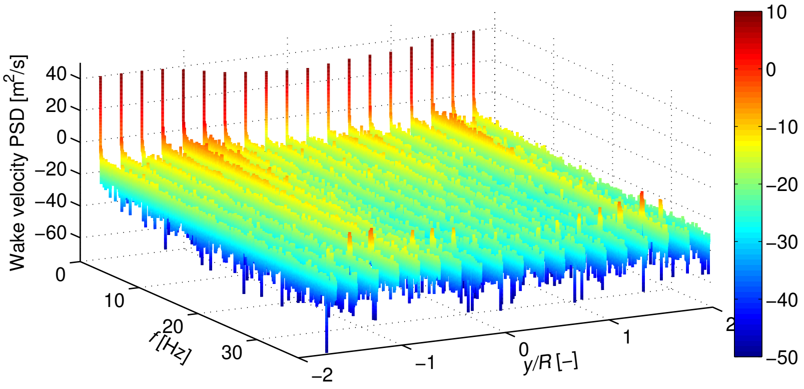

Figure 5.11: Spectrogram of the longitudinal wind velocity measured in each wake position, for a $I_u = 9.2\%$ and at $z = 0.50H$.

did not show large differences from smooth to turbulent flows. Upon examination of the turbulence intensity profiles in the wake, it was also noticed that the effect of the shaft wake is minimized by the turbulence increase, probably reducing the detriment of the turbine performance related to it. Moreover, the results of dedicated unsteady CFD simulations highlighted that the peaks in the turbulence intensity are directly related with the alternate passage of high vorticity zones. These are in turn generated by: 1) the vortex shedding of the central tower (central peak); 2) the passage of macro vortices that are detached from the aerofoils as soon as they undergo deep stall conditions (higher peak at negative y/R); 3) the shed vorticity coming from the flow reattachment on the aerofoils as soon as the incidence angle starts decreasing again in the downwind region (peak at positive y/R). To conclude, the present study confirmed that VAWTs tend to perform better in turbulent flows, both for turbine production and wake recovery. These experiments, combined with the additional information coming from CFD simulations, provide innovative and valuable data to understand their operation. Future work will be devoted to testing the rotor at other Reynolds numbers and tip-speed ratios in order to increase the knowledge on how the flow interacts with the blades; more wake distances will also studied in order to acquire useful information of practical use in designing VAWT array configurations for urban roofs.

Chapter 6

Aerofoil testing and characterization for urban VAWT

6.1 Objectives of the measurement campaign

The study on the near wake revealed that turbulence promoted faster wake recovery and reduced the losses caused by the shaft. However, the main candidate to justify the performance increase is the impact of turbulent flows on the stall of the blades [Paraschivoiu, 2002]. Hoffman in 1991 already detected positive influence of turbulence in the lift curve of a symmetric NACA0015 aerofoil [Hoffmann, 1991]. And the subject has been studied in detail for non-symmetrical HAWT aerofoils, always resulting in a very positive influence of turbulence on the stall of the aerofoils [Devinant et al., 2002, Amandolèse and Széchényi, 2004]. But no one up to the moment combined the characteristics of the aerofoils with the overall VAWT performance measured under different turbulence flows. The objective of this chapter is to study the effect of turbulence on different VAWT aerofoils, and extrapolate this to the behaviour of the whole turbine.

Here, as the blade is the element of interest, the parameter to describe the incident wind will be Re_c. As seen in previous chapters, Re_c in the VAWT prototype used is of the order of 10^5. That is low compared with the commercial VAWTs built in the past, as FloWind (Figure 1.16), where Re_c was of the order of $3 \cdot 10^6$ [Miller et al., 2018]. However, smaller wind turbines present lower values, comparable to the ones of the prototype: in the 2m-SANDIA prototype Re_c reached values of 2 - 3 $\cdot 10^5$ [Paraschivoiu, 2002].

The angles of attack were chosen from the typical values subjected by the blade during a rotation, as in Fig. 1.26. VUB Grid 1 allowed to generate medium and high turbulence to evaluate the effect of I_u in the VUB wind tunnel, as explained in chapter 3. While the tests at VKI where performed with the pre-determined conditions described in subsection 3.3.4. Figure 6.1 presents those wind profiles. As the blade prototypes where shorter than the whole turbine, only the height from 0.1 to 0.5 m approximately are of interest. The wind speeds U where adjusted in each test to be able to compare the curves at similar Reynolds numbers.

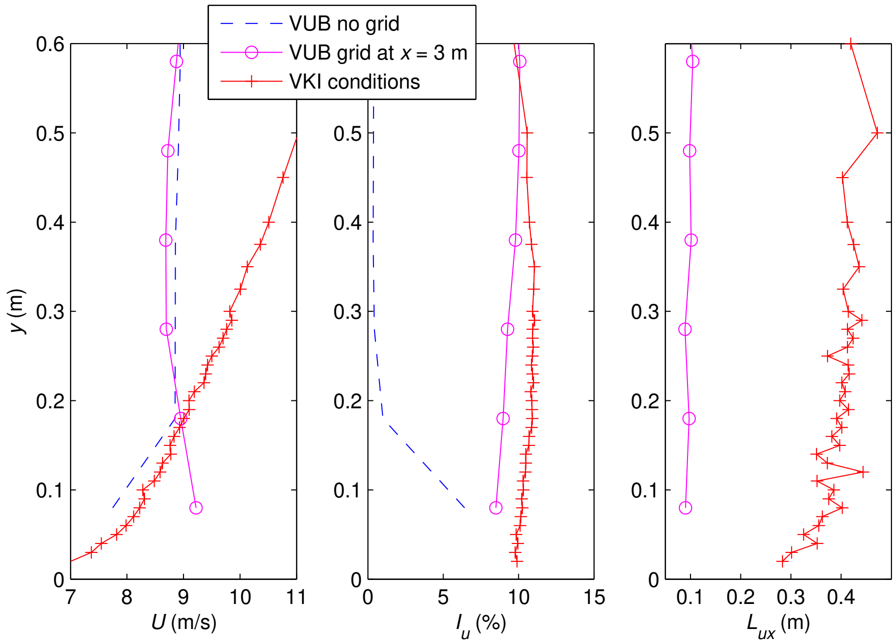

Figure 6.1: Examples of wind profiles under which the aerofoil studies where subjected.

6.2 NACA0018 blade with pressure taps

6.2.1 Calculation of aerodynamic coefficients

The first blade built was the NACA0018 with pressure taps (described in subsection 2.4.1). The 13 tabs along the surface measured a pressure that was compared with the static one coming from a Pitot tube. The differential pressure obtained was used to calculate the pressure coefficient C_p for each position along the blade chord (Equation 6.1):

$$C_p = \frac{p - p_0}{\frac{1}{2}\rho U^2} \tag{6.1}$$

Where $p - p_0$ is the pressure difference registered in each of the blade taps. Assuming 2D flow (excluding tip effects, this can be assumed in a H-Darrieus as the section is constant) the normal force (perpendicular to blade chord) coefficient was calculated by integrating the difference between the C_p in the upper and lower part of the blade (Equation 6.2):

$$C_N = -\int_0^1 (C_{p,up} - C_{p,low}) d(x/c) \tag{6.2}$$

Supposing low angles of attack ($\alpha < 20^\circ$) and $C_L > C_D$, the lift coefficient C_L could be approximated by (Eq. 6.3):

$$C_L = C_N \cos\alpha \tag{6.3}$$

Drag was calculated by the wake survey method, or scanning transversally the wind speed U in the wake of the profile. This method, based in the integral momentum conservation, permits calculating the forces acting on a body from their reactions on the flow. The model is limited due to its assumptions of constant static pressure and negligible turbulent and viscous stresses, but it simplicity makes it useful in this preliminary study. The formulation from Jones (Equation 6.4) was used [Schlichting, 1979]:

$$D = \int \rho U(y)(U - U(y))dy \tag{6.4}$$

And from there the drag coefficient was calculated (Equation 6.5)

$$C_D = \frac{D}{\frac{1}{2}\rho c U^2} \tag{6.5}$$

6.2.2 Pressure distributions measured along the blade

The results from the pressure distributions along the blade show how much are they influenced by the free stream turbulence. Fig. 6.2, Fig. 6.3 and Fig. 6.4 present the normalized mean pressure distribution along the blade at $\alpha = 8^\circ$, $\alpha = 14^\circ$ and $\alpha = 20^\circ$. The C_p values are inverted so the suction side distribution appears at the top. At 8°, before stall, it can be seen how the distribution is similar in the 3 cases, just with slightly higher suction in the low turbulence case. Fig. 6.3 at 14° shows how the blade at low turbulence is completely stalled, while, in this case, the two turbulent cases are still lifting (even more than at $\alpha = 8^\circ$), and nearly with exact values between them. At 20°, in all three conditions the blade appears stalled, except for the high turbulence case, where near the leading edge there is still some suction in the upper part of the blade. Even if the difference is small, in this figure it can also be appreciated how towards the trailing edge as I_u increases pressure rises slightly, suggesting pressure recovery is also enhanced by turbulence. Therefore, it can be concluded that the effect of I_u is that, instead of a sudden detachment of the flow in all the blade, in turbulent flow the detachment occurs progressively from the trailing to the leading edge as α increases. Those results show perfect agreement with the C_L and C_D values in Fig. 6.5 and Fig. 6.6. For simplicity, only some error bars are presented to give an indication of the uncertainties (combining the σ of the signal and the experimental errors, as explained in section 2.6).

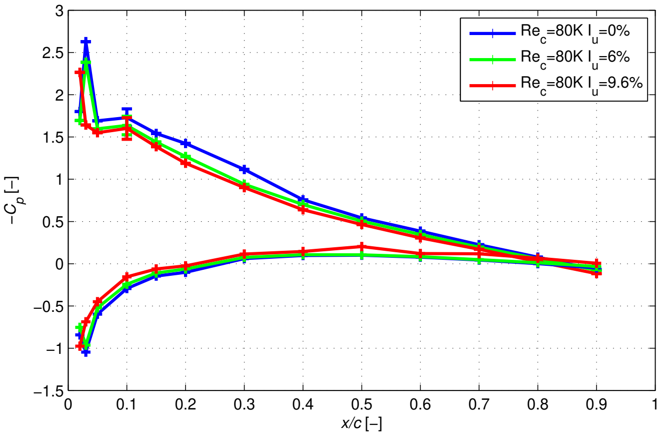

Figure 6.2: C_p coefficients measured along the chord with different I_u conditions at $\alpha = 8^\circ$.

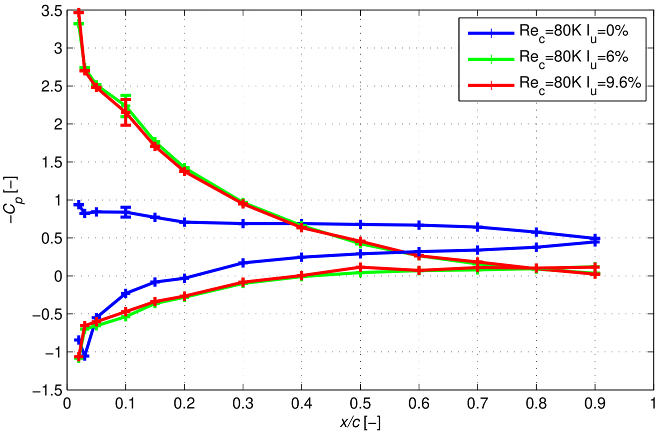

Figure 6.3: C_p coefficients measured along the chord with different I_u conditions at $\alpha = 14^\circ$.

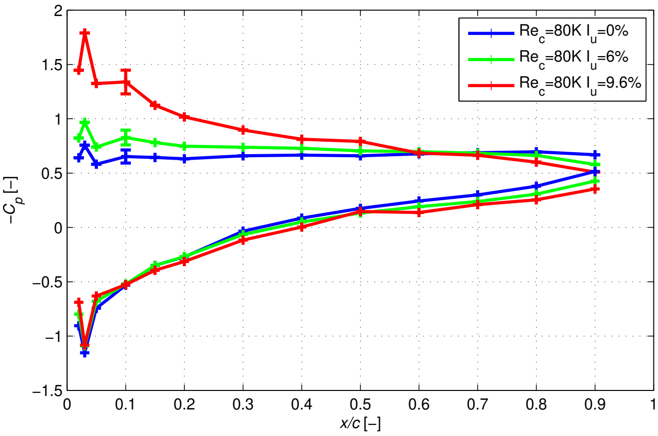

Figure 6.4: C_p coefficients measured along the chord with different I_u conditions at $\alpha = 20^\circ$.

6.2.3 Polar curves obtained

Fig. 6.5 and Fig. 6.6 present the C_L and C_D curves obtained with the different Reynolds numbers and turbulence conditions, compared with literature data collected in the SANDIA project [Sheldahl and Klimas, 1981] in a low-turbulence wind tunnel facility. It can be seen how the lift curve obtained at $I_u = 0.5\%$ coincides with the literature one for angles of attack lower that 12°, while afterwards the registered lift value is significantly higher than in literature. Considering the drag coefficient, the values obtained with the wake survey method are also quite accurate for angles before stall, while considerably higher than the ones from literature for high α, which can be explained by the difference in the experimental methodology. The Jones method is of limited use for stall conditions as neglects viscous and turbulence effects, while the measurements in [Sheldahl and Klimas, 1981] were performed with an aerodynamic balance. However, the focus of this study was to compare between the different turbulence levels, and in those cases all measurements have been obtained with the same methodology. Examples of the error bars for each curve at $\mathrm{Re}_c = 80 \cdot 10^3$ are also presented.

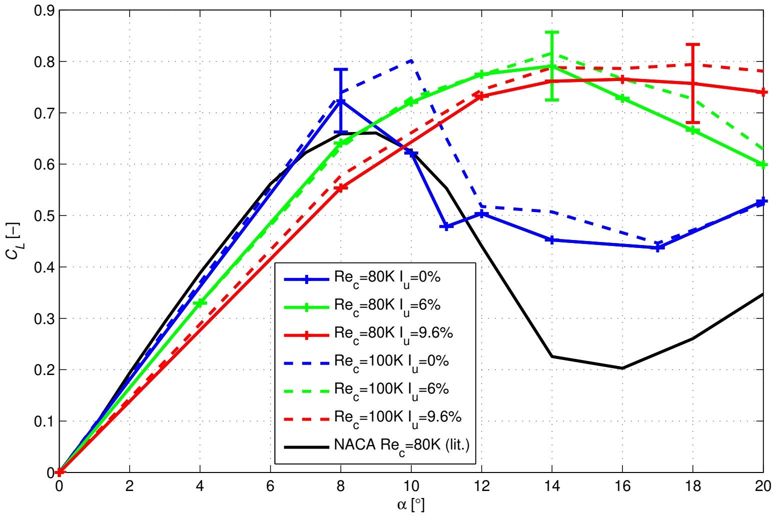

Figure 6.5: C_L - α curves obtained with different Re_c and I_u conditions, compared with literature data [Sheldahl and Klimas, 1981].

When comparing between the different flow conditions, it can be appreciated how Re_c exerts a positive effect both in C_L and C_D, however it is only considerable with the low turbulence case (minimum in the others). On the other hand, the effect of I_u in the polar curves is evident: the effect of turbulence is basically a large delay of the stall, as predicted in literature [Paraschivoiu, 2002, Amandolèse and Széchényi, 2004]. When increasing the turbulence, the stall is later and smoother, while the maximum values

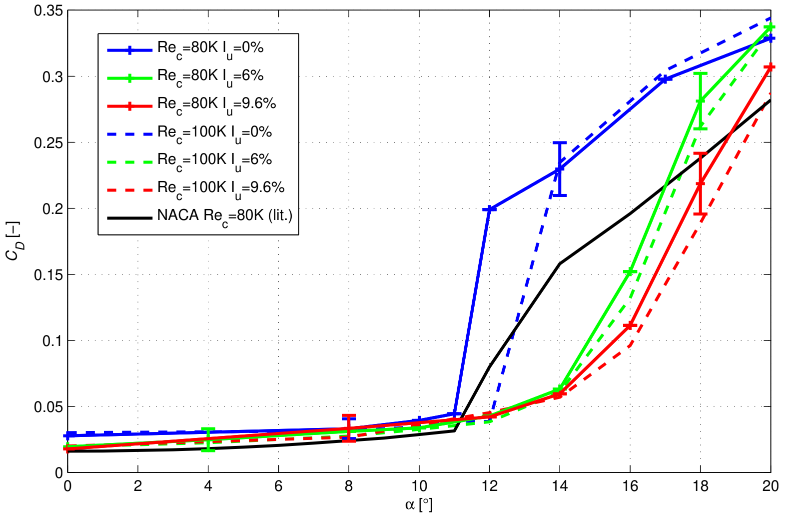

Figure 6.6: C_D - α curves obtained with different Re_c and I_u conditions, compared with literature data [Sheldahl and Klimas, 1981].

of C_L remain generally constant (but occur also at higher α) .

It is interesting to note, however, how in the linear C_L - α phase the slope is higher in the low I_u case. This results in slightly higher values of C_L at low angles of attack, and can be also appreciated in Figure 6.2 where the suction force is slightly larger in the smooth flow pressure distribution. This effect, also measured in other experiments (see Figure 6.12) has been also detected by P. Devinant, who relates it with the boundary layer thickness, which is larger in turbulent flow [Devinant et al., 2002]. However, this slope effect is not measured in other studies [Hoffmann, 1991, Amandolèse and Széchényi, 2004]. Further research on this phenomenon should be done in order to explain this effect, that could be of importance especially at the operation at large λ, where the range of α is more reduced. A dedicated set-up must be developed with this goal paying special attention to increase the precision at low α, where the aerodynamic forces are smaller.

6.3 Measurements with the aerodynamic balance

6.3.1 NACA0018 solid blade

Testing blades with the aerodynamic balance is significantly faster, as the wake survey method is not necessary anymore. In this way, more tests can be performed in less time, but the pressure distribution along the blade is not known. The first campaign done with the model described in subsection 2.4.2 was to validate the results obtained with the tapered blade. As the set-up was already installed, it was decided to corroborate some hypothesis like the effect of the end-plates (mitigation of tip effect) and the blockage caused by the traverse system.

Figure 6.7 shows the $C_L - \alpha$ curves obtained at different Re_c with the smooth flow ($I_u = 0.5\%$) at the VUB wind tunnel, both with aerodynamic balance and the blade with pressure taps. The results are compared with data from [Sheldahl and Klimas, 1981] and [Jacobs and Sherman, 1937]. The results from the two methods are reasonably similar, especially regarding the stall angles and the C_L after stall. The aerodynamic balance seems to overestimate slightly the values of C_L. The reasons could be the differences in the surface finishing, the lack of precision of the pressure method (equations 6.2 and 6.3 are approximations) or the disturbance of the pressure holes on the flow. Sadly, neither the two curves from literature agree in the C_{Lmax} value, so it is difficult to give a definitive explanation of this difference.

The same results are presented for C_D in Figure 6.8. Here only [Sheldahl and Klimas, 1981] had values of the drag after stall, so they are the only presented. The values before stall are consistent between the two methods. After stall, however, the two methods diverge, even though in both cases it is clear that Re_c delays the stall angle. The aerodynamic balance model stalls 2 degrees before the values registered with the wake survey. This is possibly caused by some misalignment in the axis and differences in the surface finish. At the end, as seen before, these blades enter in very sudden stall in absence of turbulence and small differences in the set-up can cause it. In the post-stall zone, the aerodynamic balance presents better agreement with literature. As stated in the previous section, the wake survey method is not as precise for highly turbulent flows as the present after stall. Also, it is important to note that, due to the balance precision mentioned in table 2.2,

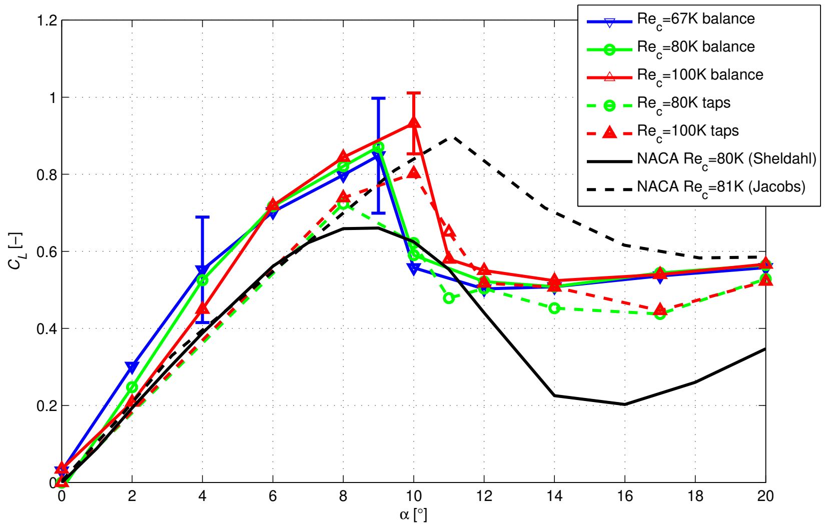

Figure 6.7: C_L - α curves obtained with different Re_c with the aerodynamic balance, pressure taps blade and data from literature [Sheldahl and Klimas, 1981, Jacobs and Sherman, 1937].

errors in this measurement where of the order of 0.05 (which is the 200% of the value at C_{D0}). This fact could not be improved as this model was too small for the balance available. However, as D increased this relative error was reduced.

The set-up was also used to measure the influence of removing the top end-plate (visible at Fig. 2.14) in order to compare the results with the ones obtained at VKI tunnel, where no top end-plate could be installed due to logistic reasons. As seen in subsection 2.4.4 in blades like these ones with aspect ratio $H/c < 10$, the 3D effects are not at all negligible. Figure 6.9 shows the polar curves obtained at similar Re_c with and without using the top end-plate. It can be seen how the effect is not negligible at all. In Fig. 6.9.a it is visible how before stall the blade with end-plate lifts significantly more, a fact that can be explained because the effective surface of the blade becomes smaller due to tip losses. However, it also stalls slightly sooner; the induced α caused by the tip vortex reduces the effective α, which can explain both effects. At the C_D graph (figure 6.9.b) it can also be seen how before stall the performance of the blade with end-plate is better, but after stall its drag is superior than in the absence of the plate, when the a small part of

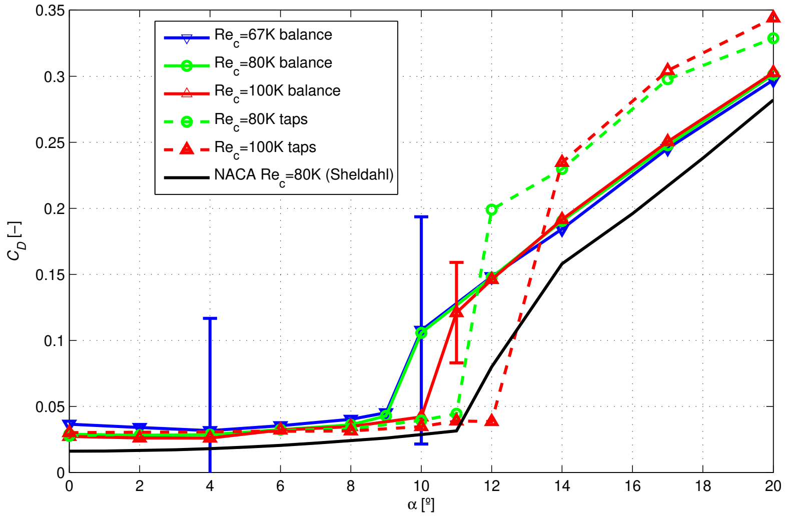

Figure 6.8: C_D - α curves obtained with different Re$_c$ with the aerodynamic balance, pressure taps blade and data from literature [Sheldahl and Klimas, 1981].

the flow is able to escape over the tip. This fact can be observed in figure 6.10 where a smoke generator was used for visualization of the flow around the blade tip.

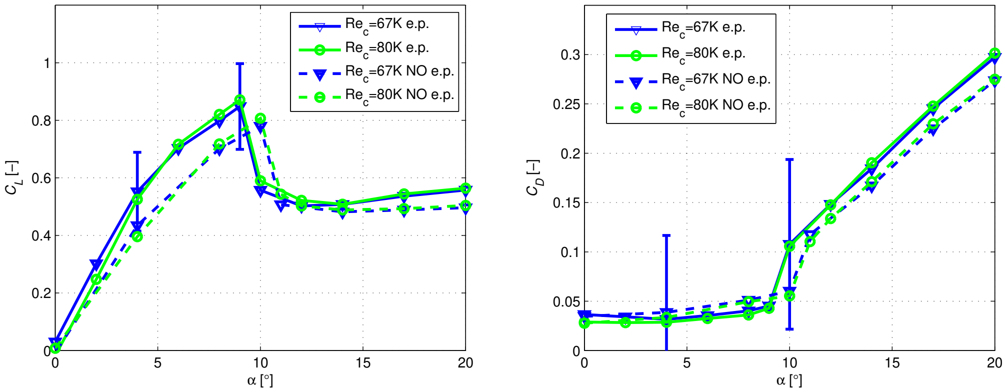

(a) (b)

Figure 6.9: C_L - α (a) and C_D - α (b) of a NACA0018 blade obtained at different Re$_c$ with and without end-plates.

When the aerofoil characteristics were measured with the balance, the cart that moves the hotwire was not behind the model (while it was with the pressure taps model in order to register the wake). As observed with the use of flow visualization (Fig 6.11) it can be seen that the cart has a large influence on the flow, so that could also justify the difference in slope.

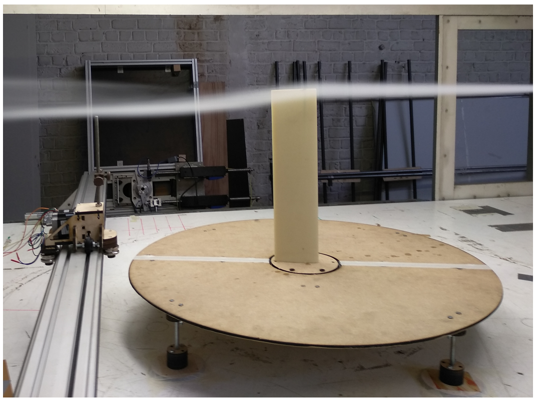

Figure 6.10: Smoke visualisation of the effect of the tip of the blade.

Figure 6.11: Smoke visualisation of blockage caused by the traverse cart.

6.3.2 Cambered aerofoil measurements

The measurements with the aerodynamic balance were repeated with the cambered aerofoil model at VUB (see subsection 2.4.3). As the blade had a $c = 20$cm (instead of 10 cm), wind speeds had to be adapted to be able to compare with similar Reynolds numbers. Due to the different manufacturing process this model had a more rough finishing, so that is a factor that must be taken in mind when comparing the performance of one model and the other. Figure 6.12 presents the values of C_L obtained with the cambered model, compared with the NACA0018 evaluated at last section. The effect of the cambered blade is a significant increase of C_L in the positive range of α in exchange of losing lift and stalling earlier in the negative angles. The effect of turbulence is also very positive in the case of this blade (see the difference between the two curves at $\mathrm{Re}_c = 80{,}000$). The results obtained with the cambered blade also show relatively good agreement with the design data from [Bianchini et al., 2015].

In the C_D curves (Figure 6.13) apart from the beforementioned delay of stall, it is obvious that in this case the cambered aerofoil produces more

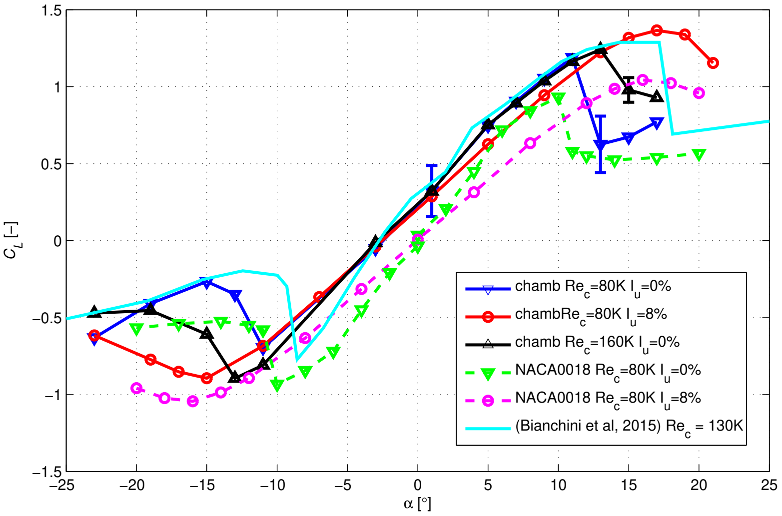

Figure 6.12: C_L - α curves obtained at different Re_c and I_u levels with the NACA0018 and the cambered blade, compared with data from literature [Bianchini et al., 2015].

drag than the NACA0018. This fact can be caused by the fact of the rough finishing of the blade, but also because the shape of this cambered aerofoil is not as optimized as the NACA0018. The drag values also present good agreement with literature, although in this case the data for low angles of attack is uncertain due to the reduced precision of the balance for those small loads, as mentioned in Figure 6.8.

6.4 Aerofoil tests at VKI (shear flow)

The main goal of the tests at VKI was to observe the effect of shear flow and large L_{ux} in the performance of the turbine and blades. At section 4.3 it was described how the excessive vibrations encountered made impossible to operate the VAWT in optimal conditions. This is not as critical for a static blade and the balance that was isolated from those vibrations. As the wind conditions were fixed (as described in Figure 3.17 and Table 3.3), extra tests had to be done at VUB (without end-plate) in order to compare the results.

The curves obtained with the NACA0018 blade are presented in Figure 6.14. At this low $\mathrm{Re}_c = 67{,}000$, the effect of turbulence is very marked, with

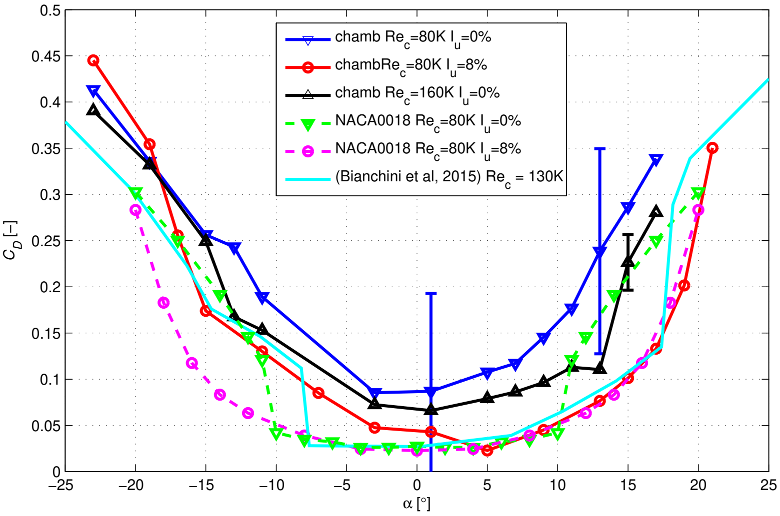

Figure 6.13: C_D - α curves obtained at different Re_c and I_u levels with the NACA0018 and the cambered blade, compared with data from literature [Bianchini et al., 2015].

a significant increase of C_{Lmax} and delay of stall. What can be read from Figure 6.14.a is that at these Re_c turbulence is the most driving factor, as the curves with enhanced turbulence look very similar, while the one from VUB in smooth flow offers poor C_L values in comparison. In Figure 6.14.b, the drag is slightly different: in this case the curve coming from the shear flow at VKI results in a higher C_D after stall.

Figures 6.15 and 6.16 show the same measurements but for the cambered blade. As its chord is double, also it is the Re_c. Now the effect of I_u is not as drastic, but still important. As in figure 6.14 the C_L curves of the two turbulent cases look very similar while the C_D registered under shear flow at VKI is slightly higher. Specially in Figure6.15 it is important to note the that in this case (contrary to what happened in Figure 6.12) specially the slope of the C_L curves does not agree much with the one from literature. This is why in this graph the experimental curves (both at VKI and VUB) where obtained without the end-plates, registering then a lower C_L slope, in accordance with what was measured in Figure 6.9.

Overall it seems that the effect of a logarithmic and a uniform wind profile on the aerodynamics of a NACA0018 blade is quite similar, as far as their

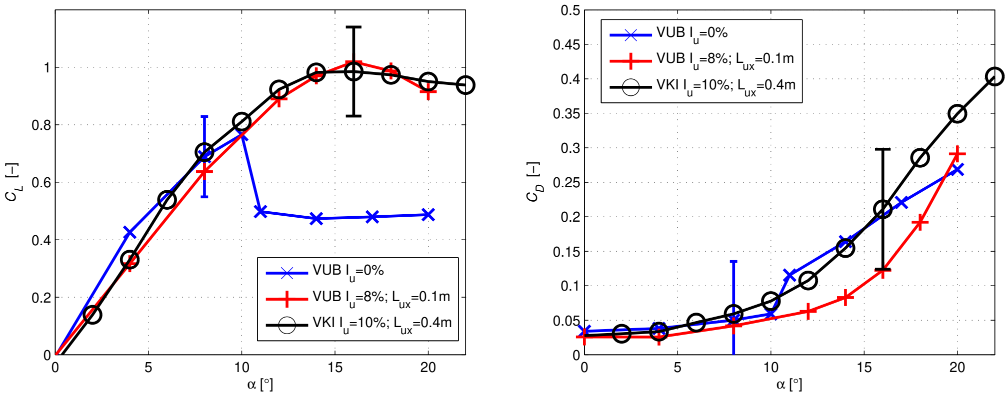

(a) (b)

Figure 6.14: C_L - α (a) and C_D - α (b) of a NACA0018 blade obtained at Re_c = 67,000 with different flow conditions.

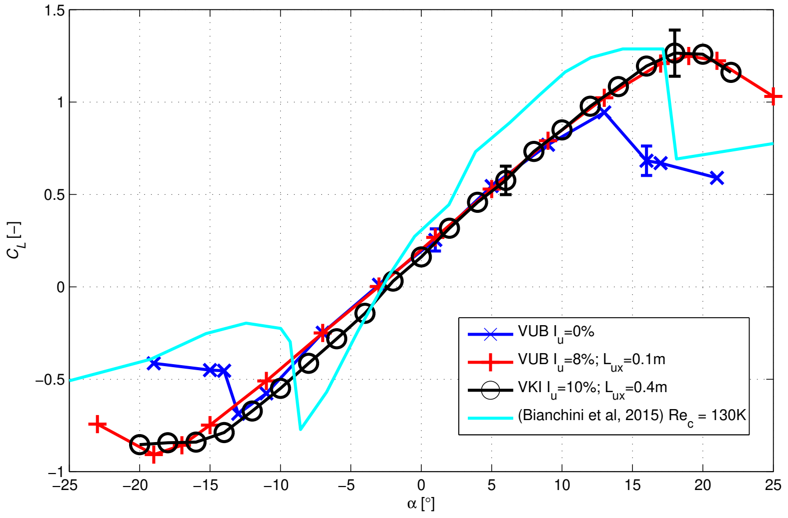

Figure 6.15: C_L - α curves of the cambered blade obtained at Re_c = 135,000 with different flow conditions, compared with data from literature [Bianchini et al., 2015]

Re_c and I_u are the same. This fact appears to be in contrast with the results from section 4.3, suggesting that the inability to operate the VAWT in the flow of VKI was only a set-up defect, but not an aerodynamic one.

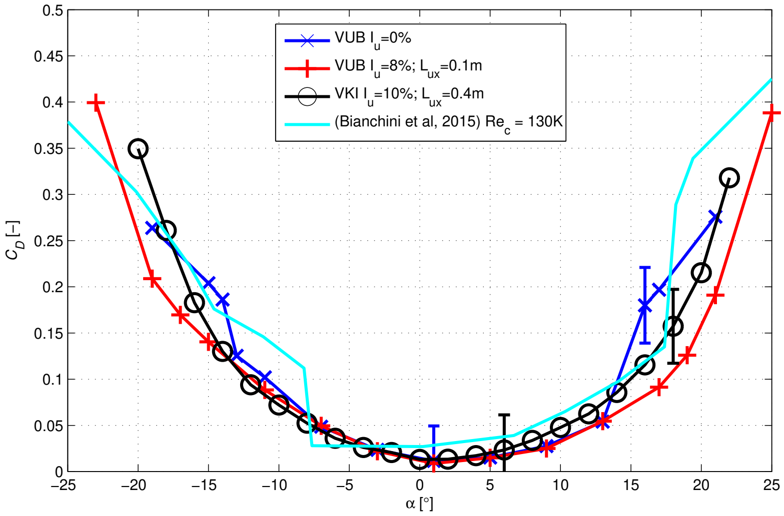

Figure 6.16: C_D - α curves of the cambered blade obtained at $\mathrm{Re}_c = 135{,}000$ with different flow conditions, compared with data from literature [Bianchini et al., 2015]

6.5 Towards an optimisation method for VAWT blades

6.5.1 An approximation using the Single StreamTube model

The experimental procedure to obtain the aerofoil polar curves is less complex and costly than measuring the performance of the overall turbine. Therefore, this process could be used to optimise the blades for its use in turbulent environments before building a VAWT prototype. Aerodynamic models of the VAWT could be used to extrapolate the values from aerofoil polars to turbine C_P-λ curves, as explained in subsection 1.3.3. In a first approximation of the problem, the Single StreamTube model (SST) was used [Paraschivoiu, 2002, Biadgo and Simonovic, 2012].

The results observed in Fig. 6.17 are only a first approximation of the potential of the technique. The $C_P - \lambda$ values predicted from the polars obtained with the tapered blade model at different turbulence levels are presented. It is clear that the curve for smooth flow decays too fast when encountering blade stall, while in the turbulent cases stall does not occur at any moment and the curves are much less pronounced. However, even with the simplicity of the model, it is remarkable how the optimal λ is accurately predicted: around 3.2, and slightly lower as turbulence is increased.

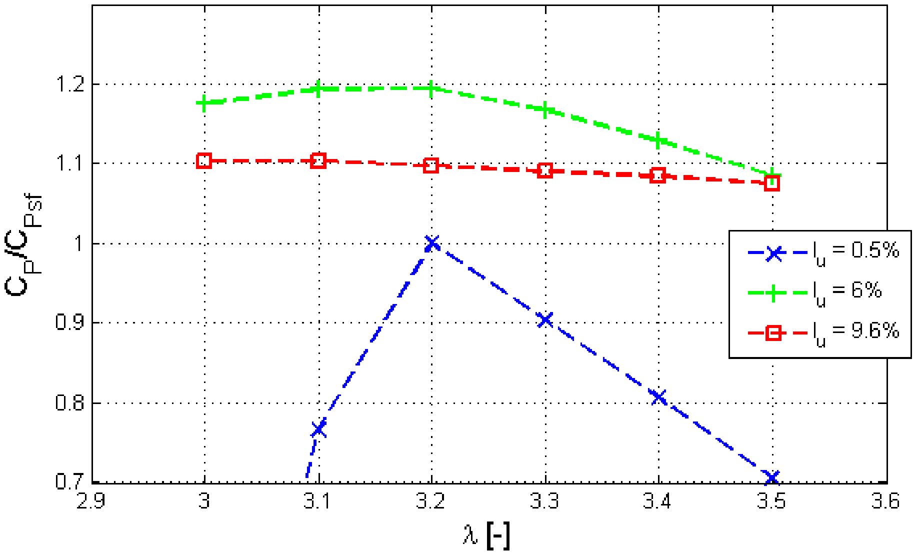

Figure 6.17: Power curves (normalized with the max. C_P in smooth flow) obtained by introducing C_L and C_D curves in the SST model.

The increase of peak performance is detected for the medium turbulence case but the highest turbulence case presents intermediate values. The reason of this difference for high turbulence can be found in the limitations of the model, which does not consider dynamic stall nor the effect of the shaft, two factors in which it was proven that the increase of turbulence had a positive influence in VAWT performance [Paraschivoiu, 2002, Carbó Molina et al., 2018, Amandolèse and Széchényi, 2004]. Therefore, a logical continuation of this study would be to improve the modelling technique to be able to predict accurately the performance of a VAWT for high turbulent cases.

6.5.2 Considerations about dynamic stall

It is clear, then, that dynamic stall has to be taken in consideration for this future study. Developing a moving set-up to replicate the oscillating movement of the wake as in [Amandolèse and Széchényi, 2004] could have been a valuable addition for this study, but it was not possible in this case. However, applying the data from literature to this specific case could help having an idea about how this chapter findings translate to the real operation of the VAWT blades. In subsection 1.3.2 the general characteristics of dynamic stall were presented. The reference case and its extrapolation to dynamic stall are presented in Table 6.1.

VAWT characteristics		**VAWT conditions**		**Aerofoil conditions**	
VAWT	H-Darrieus	ρ	1.2 kg/m^3	U_{blade} range	18.9 - 36.9 m/s
H	0.8 m	μ	$1.8 \cdot 10^{-5}$	U_{blade} mean	28 m/s
D	0.5 m	U	9 m/s	Re_c range	63,000 - 123,000
c	0.05 m	λ	3.1	Re_c mean	94,000
Aerofoil	NACA0018/ cambered	ω	111 rad/s	k mean	0.0986

Table 6.1: Conditions of the VAWT reference case, physical values reached in the turbine and the blades.

From the simulations of this same VAWT at low incoming turbulence described in chapter 5 and published at [Carbó Molina et al., 2018, Balduzzi et al., 2019], the angles of attack expected by the blade in a rotation are presented in figure 6.18. The maximum angle of attack (occurring approximately at an azymuthal position of $\theta = 120^\circ$) is slightly higher than 20° in the case of low λ, an incidence at which the blade is stalled in most of the conditions previously studied. At high λ, however, the maximum α is around 14°.

From literature it can be seen how at these Re_c, α ranges and k values the dynamic stall angle occurs 2 or 3 degrees later than the static one, with significant hysteresis [McCroskey, 1981, Amandolèse and Széchényi, 2004]. That means that in these conditions the blade would enter in dynamic stall in the low turbulence at low λ, but at high. In fact, from the CFD simulations of the instantaneous torque along the rotation it can be observed how at $\lambda = 2.6$ the blade enters sudden stall over $\theta = 90^\circ$ (Fig. 6.19), while at $\lambda = 3.3$ the blade operates smoothly in all the upwind part of the rotation.

This dynamic stall at low λ will not happen for highly turbulent flows (see Figures 6.5 or 6.12), where the stall is delayed 4 to 6°, and therefore would fall outside the operating conditions of the blade. Seeing that, the idea must be to maximize the power extracted from the wind in the upwind

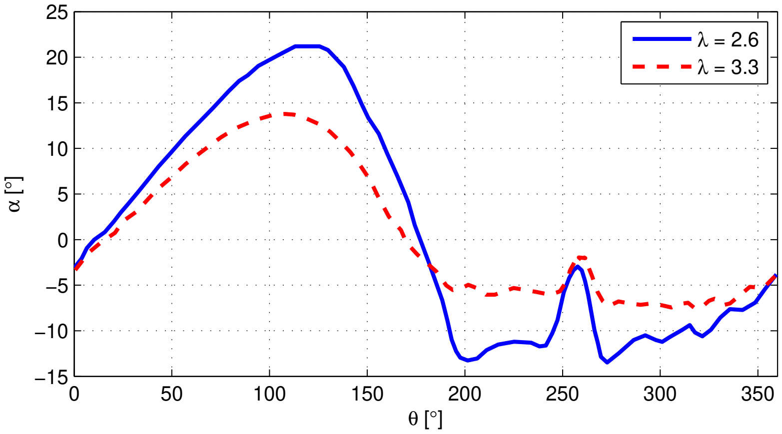

Figure 6.18: Averaged angle of attack at each azymuthal position at different λ with low incoming turbulence [Balduzzi et al., 2019].

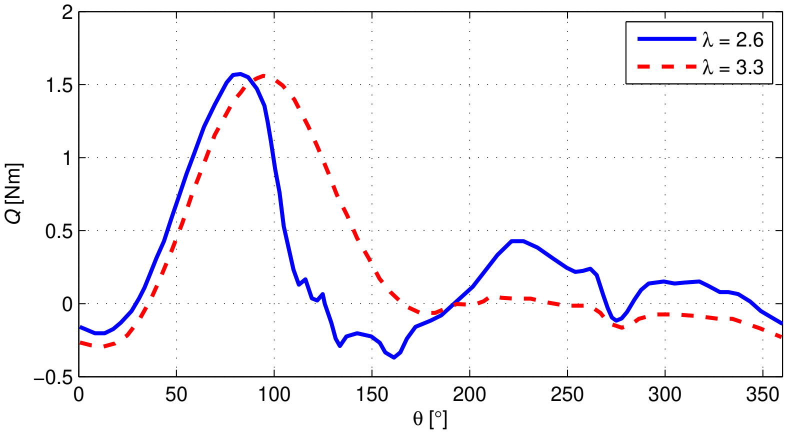

Figure 6.19: Averaged value of torque for each azymuthal position at different λ with low incoming turbulence [Balduzzi et al., 2019].

quarter of the rotation ($45^\circ < \theta < 135^\circ$) where more than 50% of the power is extracted [Rezaeiha et al., 2018]. To operate at the maximum possible C_L in this region, where angles of attack vary between 10 and 20°, it could be a very good idea to use of cambered aerofoil (see Fig. 6.15) which increases the performance in the positive angles of attack in exchange of losing some properties in the negative part of the rotation.

6.6 Discussion of the results

The goal of this study was to relate the results previously obtained in VAWT testing to the blade aerodynamics, which would allow to optimize VAWTs for turbulent flows.

Three blade models were tested, a symmetric NACA0018 provided with pressure taps that allowed to measure the pressure distribution along it, and two solid models for tests on aerodynamic balance. The models were subjected to the same angles of attack and Reynolds numbers that would be found in normal VAWT operation, while turbulence intensity and integral length scale are kept at levels similar to those found in urban environments, as in previous chapters.

When comparing between the different flow conditions, it can be appreciated how Re_c exerts a positive effect both in C_L and C_D, however it is only considerable with the low turbulence case (minimum in the others). On the other hand, the effect of I_u in the polar curves is evident. Although there is a slightly higher C_L slope for small angles in the low turbulence case, it can be appreciated how the effect of turbulence is basically a large delay of the stall, as predicted in literature. When increasing the turbulence, the stall is later and smoother, while the maximum values of C_L remain generally constant (but occur also at higher α).

The pressure distributions also showed that as turbulence increase this stall is much less pronounced, with the detachment of the flow occurring progressively towards the leading edge as α increases. On the other hand, for low angles of attack C_L was slightly higher at low turbulence, while its maximum value overall was similar in all turbulent cases (just happening at different α). C_D curves obtained with the wake survey method tended to overestimate the values from literature, a fact that can be caused by the different methodology and due to the roughness of the model. In general the stall angles were correctly predicted, and it was found that the maximum values of C_D (after stall) were also similar between all turbulent cases. It is also worth noticing that the effect of Reynolds number was lower as turbulence increases.

The tests done with the aerodynamic balance, even producing less precise measurements for low C_D, were much less time-consuming, and allowed to perform several validations in the set-up. The effect of the end-plates was measured, showing that the end-plate restrains tip losses, that can mean a 10% drop C_L. On the other hand, the end-plate also produces the stall around 1 ° earlier.

With the aerodynamic balance also a 20 cm chord model with cambered aerofoil was built. This modification was proposed in literature in order to counter the effect of flow curvature on the H-VAWT blades. The cambered blade produced similar results as the NACA0018 with regard to turbulence, only producing higher drag probably due to surface finishing. The particularity of the cambered aerofoil is that it allowed to produce higher C_L and stall angle in the positive α in exchange of losing properties in the negative angles of attack. This fact could provide a significant advantage when harvesting the more energetic wind in the upstream part of the rotation.

This model and the NACA0018 were also tested in the VKI wind tunnel to evaluate the differences of the blade performance under shear flow with large I_u and L_{ux}. Contrary to what happened in Chapter 4, here the testing could be done without problems, and it resulted that the effect of the shear flow was small, and the mean values of Re_c and I_u determined the shape of the polar curves.

Even when the aerofoil curves suggested a substantial increase of performance with turbulence (as measured with the turbine prototype in previous work), the first try to model this performance numerically was not successful. Introducing the experimental polar curves into a Single Streamtube code detected the rise of C_{Pmax} for medium turbulence increases (I_u from 0.5% to 6%), but was not able to describe accurately the case with higher turbulence. The influence of dynamic stall and the turbine shaft, that were not considered but in which turbulence exerts a significant effect, are the main suspects for this discrepancy.

Chapter 7

Conclusions

7.1 Summary of contribution

The main goal of this study was to understand the effect of turbulence on the performance and operation of small VAWTs. High levels of turbulence are one of the main characteristics of urban flows, and VAWTs are the technology with most potential to be used in the energy harvesting from wind inside urban environments. However, up to date those installations have supposed mostly failures due to their poor energy yields, caused by deficient location and poor understanding of urban flows.

Due to the complexity and unpredictability of turbulent flows, right now the best options to model them are using CFD or wind tunnel testing, being the later the one chosen for this study. After a detailed literature survey in both VAWT technology and urban flows, three phases of the experimental research were defined:

1. Creation of turbulent flows of urban characteristics inside the wind tunnel.
2. Effect of turbulence on a VAWT prototype.
3. Effect of turbulence on an individual VAWT blade.

The first part was devoted to studying the turbulence generation devices for wind tunnels. Turbulence flows can have multiple characteristics, but it was chosen to start with uniform wind profiles of isotropic turbulence, in order to compare the effect of smooth and turbulent flows on the VAWT performance. The first phase of the research, therefore, was devoted to optimize turbulence passive grids to obtain the desired levels of turbulence intensity and integral length scales. The conclusions where then applied to both wind tunnels (VUB and CRIACIV) where the research have been carried out. The non-uniformity of the wind speed profile resulted to be the main source of error in the measurements, even though anemometer calibration and torque sensor accuracy have also significant influence.

Once the desired turbulence conditions inside the wind tunnel were obtained, a H-Darrieus VAWT prototype was tested with the objective of retrieving its power curves under the effect of different levels of turbulence. A large effect of turbulence was detected, and the conclusions were corroborated by repeating the tests in the two wind tunnels. That possibility also allowed to evaluate various corrections for wind tunnel blockage, and their applicability in turbulent flows. With the same set-up the effect of turbulence on the near-wake conditions was also studied.

The study on the VAWT revealed that most of the effect of turbulence could be explained by the effect on the blade aerodynamics. Because of that, the last part of the research was devoted to study the effect of turbulence on the individual blades. With the same turbulence generation set-up, several models of blade were tested individually. The pressure distribution over the blade and the aerodynamic forces were studied, and in fact turbulence was revealed to have a large influence on blade aerodynamics, especially in stall conditions. Tests were repeated for different flow conditions and a model with another aerofoil was also built in order to provide a simplified set-up to optimize VAWT aerofoils for its use in highly turbulent environments.

7.2 Main conclusions

1. The recreation of urban turbulent flows inside a medium-sized wind tunnel using passive squared grids is possible regarding turbulence intensity levels, while integral length scale can only be approximated.

2. The values of integral length scale [Roach, 1986] and turbulence intensity [Laneville, 1973] generated by passive squared grids are successfully predicted by literature.

3. The main complication when using passive grids is that when the mesh

size is more than 10% of the wind tunnel size, the profile is very unstable, highly depending on small changes in grid geometry. It is possible to obtain uniform profiles by adjusting grid spaces next to the walls.

4. In the Reynolds number range studied (Re 267,000 to 333,000) turbulence intensity (I_u) has a very positive effect in VAWT performance, registering power increases up to 20% from smooth (I_u =0.5%) to turbulent (I_u = 15%) flows.
5. This effect is more evident for lower Re and lower rotational speeds, and some results suggest that this effect could start to fade at larger Reynolds numbers (Re > 400,000). Integral length scales, on the other hand, did not prove to have a significant effect in the range studied (1 to 3 times the blade chord).
6. Blockage effect proved to very important in the wind tunnels tested (Blockage ratio 10 and 19%), and Pope correction [Pope and Harper, 1966], even with its simplicity, provided accurate corrections also for turbulent flows.
7. The structure of the VAWT needs to be as isolated as possible from external vibrations, as they affect drastically the turbine operation by complicating its control and decreasing its performance.
8. Wind speed measurements showed faster wake recovery for turbulent flows, as the wind speed drop was 10% lower than in smooth flow. The shape of the wake in that position did not show large differences from smooth to turbulent flows.
9. Upon examination of the turbulence intensity profiles in the wake, it was also noticed that the effect of the shaft wake is minimized by the turbulence increase, probably reducing the detriment of the turbine performance related to it.
10. Blade lift curves obtained showed that the main effect of turbulence is an increase of the stall angle at the range of Reynolds numbers that were tested in this study.
11. The pressure distributions also showed that as turbulence increase this stall is much less pronounced, with the detachment of the flow occurring progressively towards the leading edge as the angle of attack

increases. On the other hand, for low angles of attack lift was slightly higher at low turbulence, while its maximum value overall was similar in all turbulent cases.

12. Drag curves obtained with the wake survey method tended to overestimate the values from literature, a fact that can be caused by the different methodology and due to the roughness of the model.
13. In general the stall angles were correctly predicted, and it was found that the maximum values of drag (after stall) were also similar between all turbulent cases. It is also worth noticing that the effect of Reynolds number was lower as turbulence increases.
14. The cambered aerofoil proposed by [Rainbird et al., 2015] delivered satisfactory results under turbulent flows; by raising the values of C_L and stall angle in the upwind part of the rotation, it could carry an increase of the overall turbine performance.
15. The tests at VKI showed that the blade coefficients do not differ significantly between uniform and shear flow, as long as the values of mean Re_c and I_u are similar.

7.3 Directions for future work

- The generation of turbulence was done in order to obtain isotropic uniform wind profiles. Other turbulence conditions for more specific cases (i. e. flow after a building corner, skewed flow, gusts) could be generated to increase the range of the conclusions.
- The results open an interesting possibility to improve urban turbines efficiency, but still could be expanded with other VAWT models, a wider range of Reynolds numbers and higher levels of turbulence and length scales.
- The study of the turbine wake can continue by testing the rotor at other Reynolds numbers and tip-speed ratios in order to increase the knowledge on how the flow interacts with the blades; more wake distances could also be studied in order to acquire useful information of practical use in designing VAWT array configurations for urban roofs.

- Concerning the optimization of the aerofoils, the continuation of the work will be devoted into improving the accuracy of the method. Experimentally, the measurements can be recreated at more Reynolds numbers and different values of turbulence. A set-up with oscillating blade like in [Amandolèse and Széchényi, 2004] would allow obtaining the curves with the dynamic stall effects.

- The SST numerical code, also, was revealed too simple to extrapolate accurately the aerofoil curves onto the behaviour of the whole turbine. The use of more refined codes (like multiple streamtube) or CFD modelling, and including the effect of the shaft is recommended to try to obtain better agreement with experimental results.

Appendix A

Annex

A.1 Technical data

This section provides extra information about the facilities and equipment described in Chapter 2.

A.1.1 Details of the wind tunnels

Apart from the size, the main difference between the three wind tunnels is their configuration. The VUB one is an open circuit where air is blown and the diffuser sends it upwards. CRIACIV, also open-circuit, is a suction wind tunnel with the fan behind the test chamber, and has a particular T-shaped diffuser. In both cases, the return circuit is the same room where the wind tunnel is located. The VKI L1-B wind tunnel, on the other hand, is a closed circuit tunnel. However, any of those differences should affect how the wind conditions are obtained after the boundary layer length. The following images present several of these details.

Figure A.1: Detail of the blower of the VUB wind tunnel (more information at `http://mech.vub.ac.be/thermodynamics/wind_engineering/tunnel.htm`

Figure A.2: Detail of the diffuser of the VUB wind tunnel (more information at `http://mech.vub.ac.be/thermodynamics/wind_engineering/tunnel.htm`

Figure A.3: Top view of the CRIACIV wind tunnel (more information at `http://www.criaciv.com/`

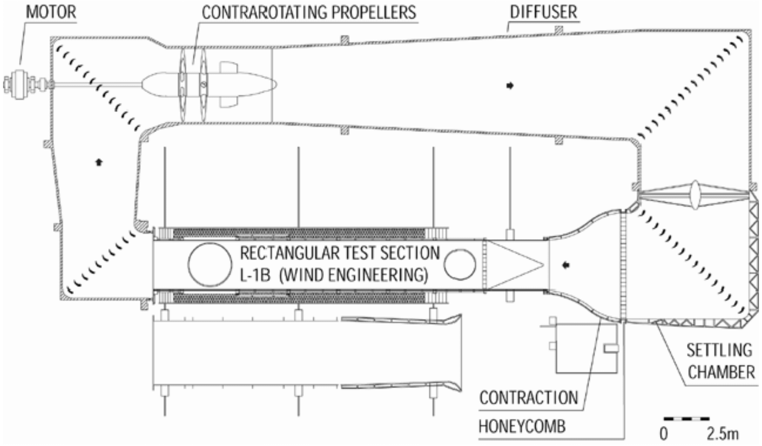

Figure A.4: Schematics of the VKI-L1B wind tunnel [Buckingham, 2010] (more information at `https://www.vki.ac.be/`

A.1.2 Equipment technical details

Hot-wire anemometers were one of the key measurement systems used in the project. In the following images their characteristics and an example of a calibration curve is presented.

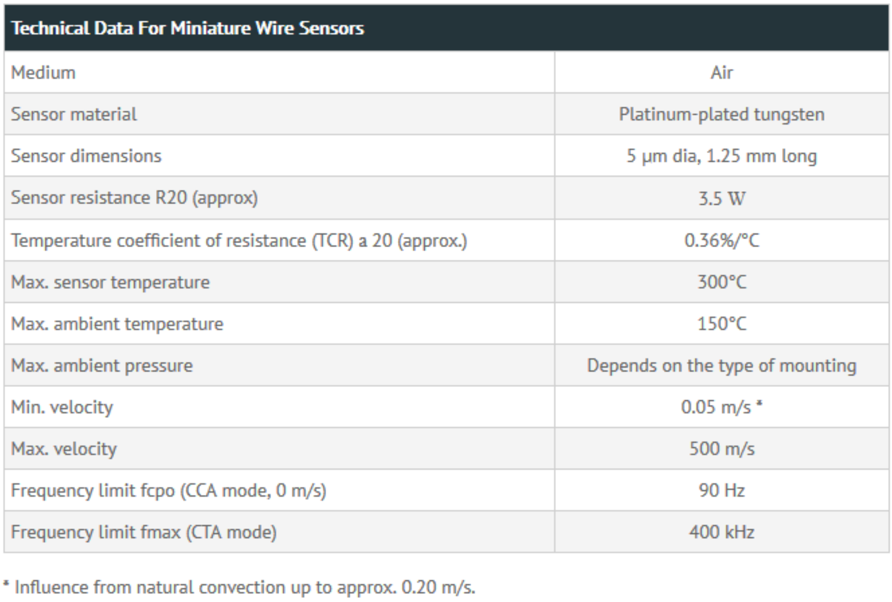

Technical Data For Miniature Wire Sensors	
Medium	Air
Sensor material	Platinum-plated tungsten
Sensor dimensions	5 µm dia, 1.25 mm long
Sensor resistance R20 (approx)	3.5 W
Temperature coefficient of resistance (TCR) a 20 (approx.)	0.36%/°C
Max. sensor temperature	300°C
Max. ambient temperature	150°C
Max. ambient pressure	Depends on the type of mounting
Min. velocity	0.05 m/s *
Max. velocity	500 m/s
Frequency limit fcpo (CCA mode, 0 m/s)	90 Hz
Frequency limit fmax (CTA mode)	400 kHz

* Influence from natural convection up to approx. 0.20 m/s.

Figure A.5: Specifications of the HWA CTA-55P11 from DANTEC, as the one used in the CRIACIV wind tunnel.

Figure A.6: Mini CTA compact model 54T42, as the one used for the VUB measurements.

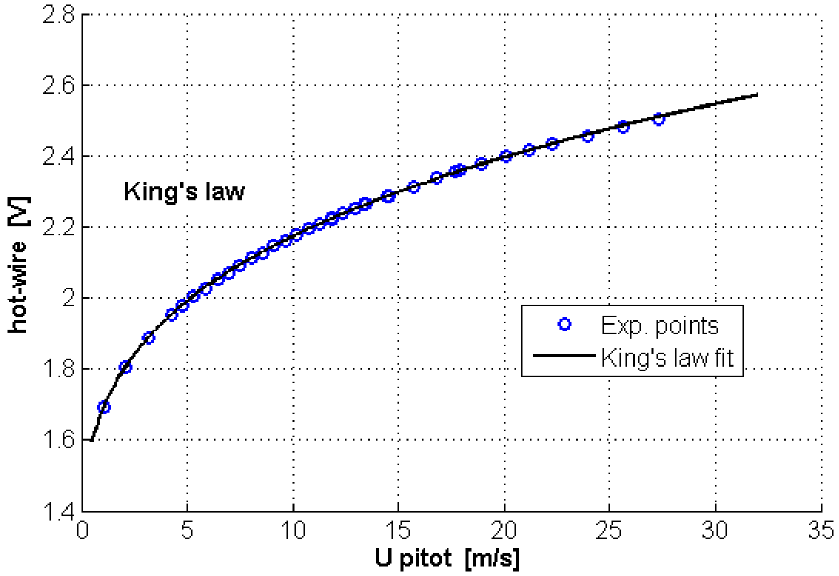

Figure A.7: HWA calibration curve obtained in one of the experiments at the CRIACIV wind tunnel.

Another key component used during the project were the traverse systems built for its use in the CRIACIV and VUB wind tunnels (subsection 2.2.3). At CRIACIV, as more time was available, a dedicated system was design, with an endless screw that allowed more precision in order to be used in other campaigns. At VUB a more simple set-up was built using aluminium profiles and a belt that moved a cart with the probe. The movement of both systems was activated with a NEMA23 stepper motor, controlled via an Arduino board using a dedicated shield Tb6560. The connection of the three parts can be seen in Figure A.8, and the Arduino code to control the motor at subsection A.3.4.

Technical data of other significant equipment used within the campaign is presented in the following figures:

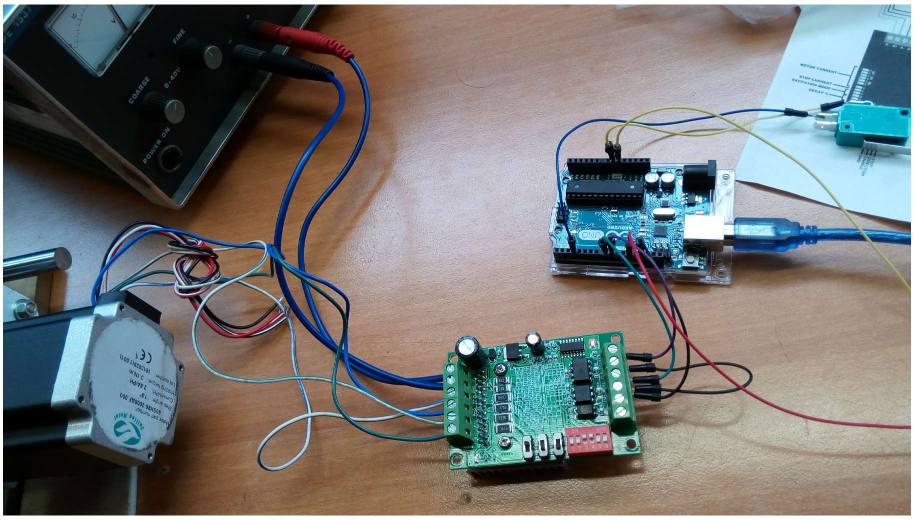

Figure A.8: Detail of the connection between the NEMA23 motor, the shield and the Arduino board.

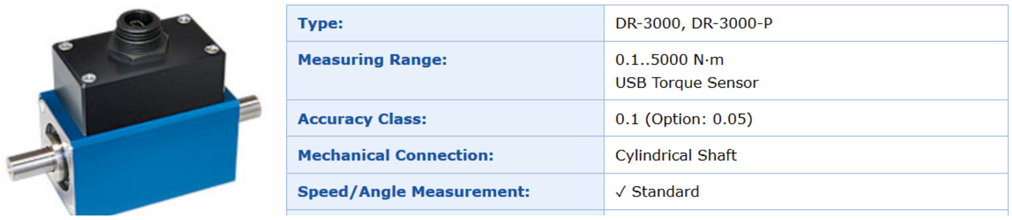

Type:	DR-3000, DR-3000-P
Measuring Range:	0.1..5000 N·m USB Torque Sensor
Accuracy Class:	0.1 (Option: 0.05)
Mechanical Connection:	Cylindrical Shaft
Speed/Angle Measurement:	✓ Standard

Figure A.9: Specifications of torque sensor used in the VAWT power measurements.

Figure A.10: Image of the K6D Multi-component balance by ME-Messysteme GmbH.

A.1.3 Turbine support structure

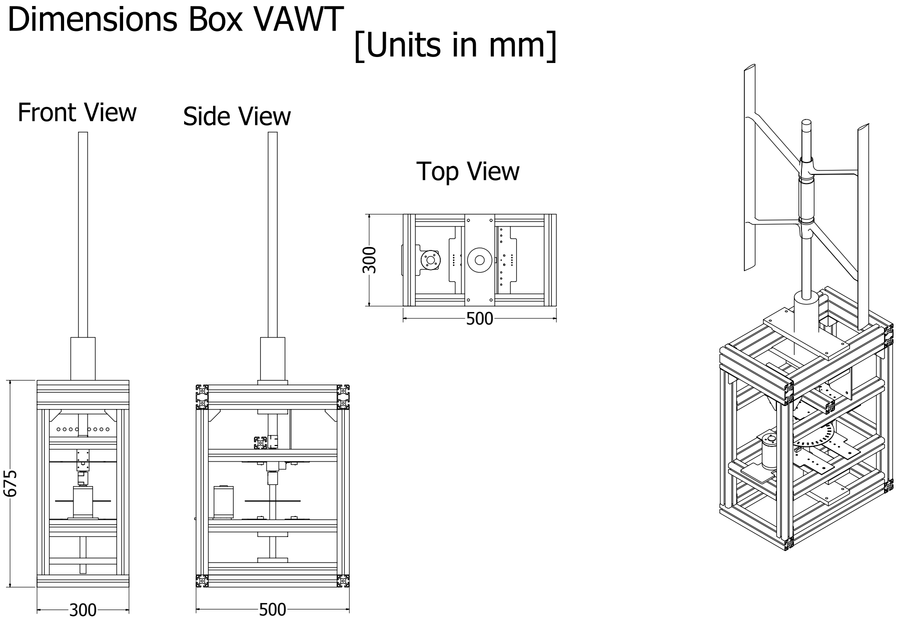

Figure A.11: Dimensions of the VAWT equipment contention box, built by the VUB FLOW group.

The CRIACIV and VKI support structures where versions of the VUB one, but with the width and height adapted for each wind tunnel.

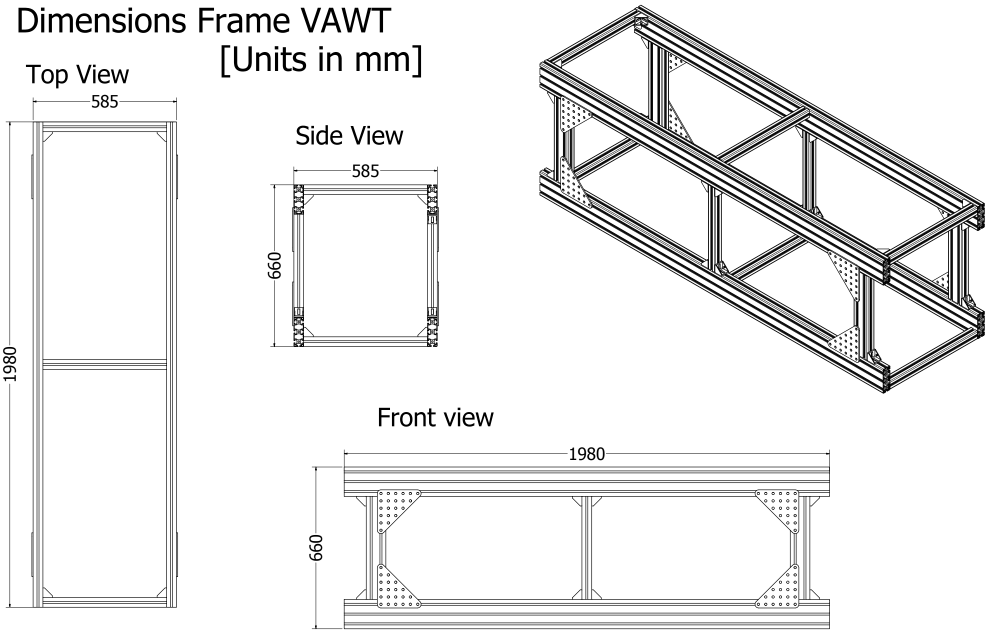

Figure A.12: Dimensions of the VAWT support structure, built by the VUB FLOW group.

A.2 Extra experimental data

A.2.1 Effect of λ upon blockage

As seen in section 2.5, blockage was a key aspect in the wind tunnel measurements. Pope's correction was applied in all cases to overcome this issue, and although its application to the power curves was satisfactory when regarding C_{Pmax} values, some doubt remained about if the blockage effect was also influenced by the VAWT rotational speed. According to some previous studies used as reference [Dossena et al., 2015], λ could have a large influence, increasing the correction factor by 15% from $\lambda = 1.5$ to $\lambda = 8$, where the turbine is turning much faster and therefore appears to the flow as a much less porous body. In the current study λ range was much more reduced (approximately 2.5 to 3.5) but still this effect had to be taken in mind. To measure it, a hot wire anemometer was placed in parallel to the VAWT during the CRIACIV experimental campaing (Figure A.13).

Figure A.13: Position of the control HWA during the VAWT tests at CRIACIV.

Figure A.14 shows the time histories of the normalized windspeed measured by the HWA and the rotational speed of the turbine. It can be seen how upon switching on the VAWT, there is indeed an increase of the wind speed measured inside the wind tunnel. The effect of the change of ω on this increase is visible, but not very relevant, of around 0.2% of the initial windspeed $U_{initial}$. In the graph is also plotted the expected blockage correction by [Pope and Harper, 1966], which is aproximately twice as high as the one recorded. This might be because the HWA is not located very close to the VAWT, where U must be higher.

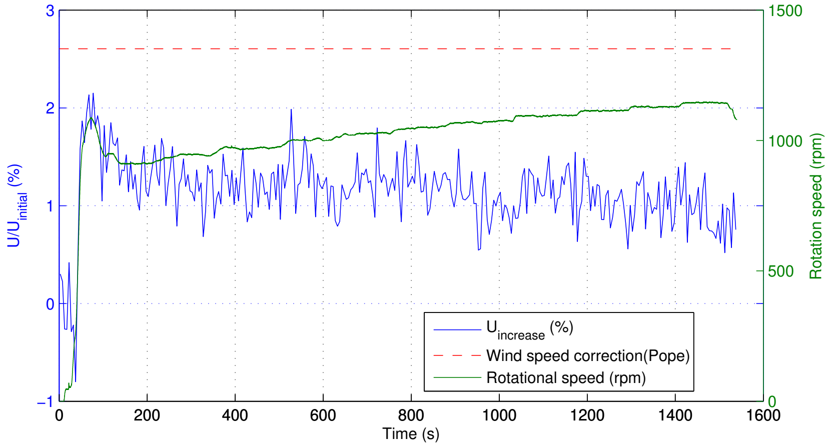

Figure A.14: Time histories of ω of the turbine and the wind speed measured by the control anemometer, during one of the tests at CRIACIV wind tunnel.

A.2.2 Calculation of extra power available due to turbulent flow

In subsection 4.1.2, while analysing the influence of turbulence on power curves, it is noted how turbulent flow is by definition more energetic than smooth flow, and how this could contribute to the detected VAWT performance boost. This section offers more detail about the samples of wind speed data obtained at low and high turbulence conditions at VUB is analysed to corroborate the statements done. Figure A.15 presents the time history of two samples obtained at the VUB wind tunnel, without grid and 3m behind the turbulence grid (conditions described at subsection 3.3.1). In those measurements, the mean U was 8.95 m/s.

As done in Figure 4.4, here it is presented the histograms of the signals (with the turbulent one scaled up 10 times for comparative purposes) of the

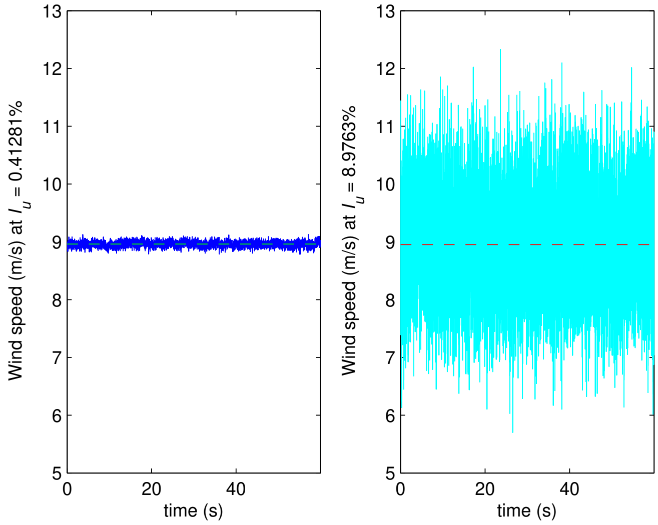

Figure A.15: Time history of U with the U_{mean} indicated,at low and high turbulence at VUB wind tunnel.

wind speed signal under the two turbulence conditions (Fig. A.16). It must be noted that the mean wind speed is exactly the same in both samples.

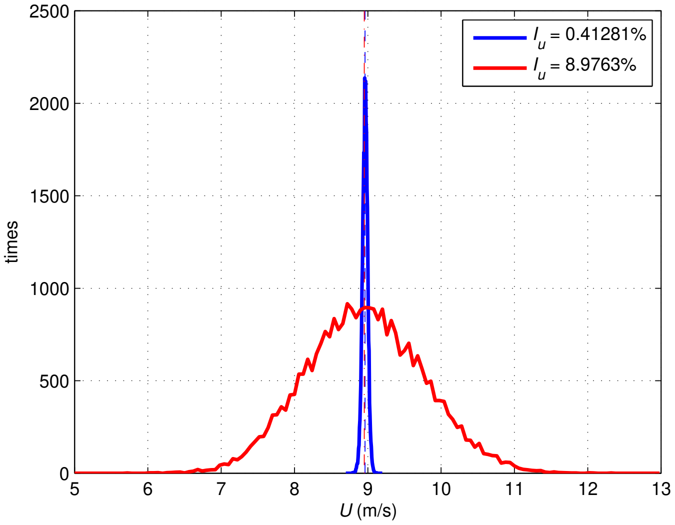

Figure A.16: Histogram of the wind speed signal at low (real scale) and high (scaled up 10 times) turbulence.

When the power available from this wind speed is calculated using equation 1.8, the resulting P_{av} is as represented in Figure A.17. These samples are the ones used to plot 4.4.a.

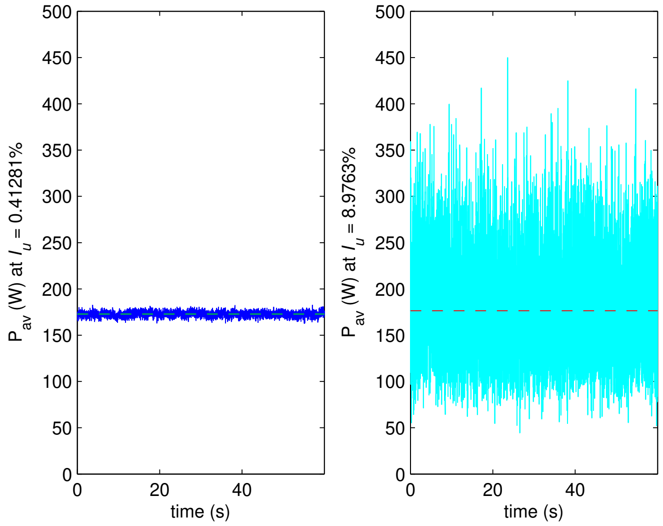

Figure A.17: Time history of P_{av} with the P_{avmean} indicated, for the two turbulent conditions.

A.3 Codes for data analysis

A.3.1 Wind profile analysis

```
%Data analysis for data from VUB (CTA system directly provides time
% histories of U)

%%Import data
 clear all
 close all

 global F Su u_m u_std

% inputs for Lux Calculation
a0=0.1;%initial approximation of Lux
f_a=500;%Acquisition frequency
D=0.072;%Reference length (bar size)

 for i=1:9

 filename=['10m' num2str(i*10-2)];
%Filename includes the measurement number)
 data = dlmread(filename,'\t',22,0);

 t=data(:,1);
 u_t=data(:,2);

%Lux code from VKI (written by Antonino Marra)
[L_u_x, L_u_x_spettro]=Lu_von_karman_spectrum(a0,u_t,f_a,i,n_oriz,n_vert,D)

%Calculation of length scale from Taylor's frozen turbulence hypothesis
%(written by Giulio Vita)
     [r,lag]      = xcov(u_t,'unbiased');
     autocorrf    = r/u_std^2;
     tau          = lag/f_a;
     TAU          = tau(tau>=0);
     TAU          = TAU';
     acf          = autocorrf(tau>=0);

     modelfun = @(a,x) exp(a*x);
     beta = 1;

     % Criterion first 0 crossing
     ind0     = min(find(acf<=0));
```

```
% index for first zero crossing
    beta0    = nlinfit(TAU(1:ind0),acf(1:ind0),modelfun,beta);
% nl esponential fitting
    acf0     = @(x) exp(beta0*x);
% fitting esponential function
    iT0      = integral(acf0,0,TAU(ind0));
% area [0:ind0]
    Li0 (i)     = iT0 * u_m;

y(i)=i/10-0.02;
U(i)=u_m;
I_u(i)=u_std/u_m*100;
Lux(i)=L_u_x;

end

%%%%%%%%%%%%%%%%%%%%%%%%%%%%%%%%%%%%%%%%%%%%%%%%%%

function [L_u_x, L_u_x_spettro]=Lu_von_karman_spectrum(a0,u_t,f_a,i,...
...n_oriz,n_vert,D)

global F Su u_m u_std

% Longitudinal component spectrum
u_m=mean(u_t);
u_std=std(u_t);
U_sm = u_t-u_m; % to have a value with mean 0
[Su,F] = pwelch(U_sm,[],[],[],f_a);

% Fit with von Karman spectrum
opzioni = optimset('MaxFunEvals',100000,'TolX',1e-06,'Tolcon',...
...1e-06,'MaxIter',10000,'Algorithm','active-set');
[a]=fminsearch('errore_spettro',a0,opzioni);
SSu=(4/u_m*a.*F)./(1+70.8.*(a.*F./u_m).^2).^(5/6);
L_u_x=a;

% Lux
[SSu_max,j]=max(SSu);
F_picco=F(j);
L_u_x_spettro=0.146*u_m/F(j); % Empirical fit

%%%%%%%%%%%%%%%%%%%%%%%%%%%%%%%%%%%%%%%%%%%%%%%%%%%%%%

function err=errore_spettro(a)
```

```
global F Su u_m u_std

err = sum((Su - ((4/u_m*u_std^2*a)./(1+70.8*(a.*F./u_m).^2).^(5/6))).^2);
```

A.3.2 Determination of the power curves

```
% Data analysis of the first tests done at the VUB on the H-Darrieus
%turbine

%SECTION 1
%Data gathering and Processing

 clear all

%Measurement informations:

% Sensortype:   DR-3000
% Serial number:          148931
% Upper range value:      2.00 N·m
% Accuracy class:         0.1 %
samp=2500 % Sampling rate (Hz)

% Column 1 (number of measurement #
%Column 2 Torque (cN·m)
% Column 3 Speed (1/min)
% Column 4 Power (W)

 filename='TS20170803165502000_2m9.csv';

 data = csvread(filename,21,0);
 time=data(:,1)/samp;

%Turbine characteristics
H=0.8; %m
D=0.5; %m

%Wind characteristics
rho=1.2; %Kg/m^3
V=9; %m/s

Q=data(:,2); %cNm
w=data(:,3)*2*pi/60; %rad/s
P=data(:,4); %W
P_av=0.5*rho*D*H*V^3; %Power available from the wind

%% Calculation of CP_lambda curve

%inputs
 seg=60; %seconds needed for validate value
```

```
rads=2.5; %+-Margin of rad/s (approx rpm/10), to consider stable omega

%Uncertainties--------------------------------------------------------
%vector with uncertainties of Q(Nm),w(rad/s),rho(Kg/m^3),H(m),D(m),V(m/s)
u_CP=[0.002 0.2 1.15E-5 0.002 0.002 0.045];
u_TSR=[u_CP(2) u_CP(5) u_CP(6)];

%calculations
steps=seg*samp;

j=0;
k=0;

for i=2:size(data,1)
    point=1;
    j=j+1;
    Wi(j)=w(i);
    Qi(j)=Q(i)/100;
    Pi(j)=P(i);

      if abs(w(i)-w(i-j))>rads
              point=0;
              j=0;
      end

      if j==steps
           k=k+1;
           Res(k,1)=(i-j)/samp;
           Res(k,2)=mean(Wi)*D/2/V;
           Res(k,3)=mean(Pi)/P_av;

           %Calculation of Uncertainties-----------

           %Inputs of each measurement
           Qk=mean(Qi);
           Wk=mean(Wi);
           stdCP=std(Pi)/P_av;

           %Derivatives and contribution to the error of each factor

           %CP error
           cu_CP(1)=Wk/(0.5*rho*H*D*V^3)*u_CP(1); %Q
           cu_CP(2)=Qk/(0.5*rho*H*D*V^3)*u_CP(2); %w
           cu_CP(3)=Qk*Wk/(0.5*rho^2*H*D*V^3)*u_CP(3); %rho
```

```
        cu_CP(4)=Qk*Wk/(0.5*rho*H^2*D*V^3)*u_CP(4); %H
        cu_CP(5)=Qk*Wk/(0.5*rho*H*D^2*V^3)*u_CP(5); %D
        cu_CP(6)=Qk*Wk/(0.5*rho*H*D*V^4)*u_CP(6); %V

        errCP=sqrt(sum(cu_CP.^2));
        deltaCP=std(Pi)/P_av;
        %/sqrt(steps)

        Res(k,4)=errCP+deltaCP;

        %TSR error
        cu_TSR(1)=D/V/2*u_TSR(1); %w
        cu_TSR(2)=Wk/V/2*u_TSR(2); %D
        cu_TSR(3)=Wk*D/V^2/2*u_TSR(3); %V


        errTSR=sqrt(sum(cu_TSR.^2));
        deltaTSR=std(Wk)*D/V/2/sqrt(steps);
        Res(k,5)=errTSR+deltaTSR;
        j=0;

        if k>1&&abs(Res(k,2)-Res(k-1,2))<0.05||Wk<0.5
            Res(k,:)=[];
            k=k-1;
        end
    end

end

Res1 = sortrows(Res,2);


figure()
plot(Res1(:,2),Res1(:,3),'-x','MarkerSize',10,'Linewidth',2)
hold on
errorbar(Res1(:,2),Res1(:,3),Res1(:,4))
%herrorbar(Res1(:,2),Res1(:,3),Res1(:,5),'x')
xlabel('\lambda','FontSize',14)
ylabel('C_P','FontSize',14)
axis([2.2 3.6 0.1 0.22])
grid on
```

A.3.3 Polar curves from pressure taps

```
%Import and read data from Scanivalve
%Tests with S. Van de Maele's NACA0018 blade for urban VAWT testing
%VUB, 24/04/2018

close all
clear all

%% Inputs--------------------
x=[90 80 70 60 50 40 30 20 15 11 6 3 2]; %taps positions
c=100; %chord (mm)

me=[0 8 10 11 12 14 17 20]; %angles measured

load('readmeU12T0.mat'); %flow characteristics
load('wakesU12T0.mat'); %wake survey profiles

%% Cl calculation

for i=1:1:size(me,2)

%Calculates Cp for positive and negative angle
for ang =2*i-1:2*i

V=read(ang,1);
Iu=read(ang,2);
al=read(ang,3);
P=read(ang,4);
T=read(ang,5);

pres_name=['P_U' num2str(V) '_T' num2str(Iu) '_A' num2str(al) '_845.txt'];

Pres=dlmread(pres_name,'\t',5,1);

Pdif(ang,:)=mean(Pres(:,1:13));

%Dynamic pressure
R=287;
rho=P/(R*(T+273.15));
Pdin(ang)=0.5*rho*V^2;

Cp(ang,:)=Pdif(ang,:)/Pdin(ang);

end
```

```
%Change tap 13 between the two measurements and puts it in right position

    Cp(:,[12 13])=Cp(:,[13 12]);

    Cpc=Cp(ang-1,12);
    Cp(ang-1,12)=Cp(ang,12);
    Cp(ang,12)=Cpc;


% Cl calculation

 %Trapezoidal integration

Cn(i) = trapz(x/c,Cp(ang-1,:)-Cp(ang,:));


% Cd calculation

    y=wakes(:,2*i-1)/1000;
    U=wakes(:,2*i);

    U(U==0) = [];%eliminates zeros values
    y=y(1:size(U,1));

    Umean=mean([U(1),U(size(U,1))]);
    Uint=rho.*U.*(Umean-U);
    D=trapz(y,Uint);

    CD(i)=D/(0.5*rho*c/1000*V^2);


end
Cl=Cn.*cos(me*pi/180);
```

A.3.4 Traverse system control

```
//Arduino code to control the traverse system operated by a NEMA23 motor

int Distance = 0;
int pos=0;
int timedelay=100;
char val='s';
int CLK=9; //pulse
int CW=8; //direction
int cm=5333; //steps for 1 cm
int dm=26667; //step for half dm
int FCB=2; //fine corsa 1 (bottom)
int FCT=12; //fine corsa 2 (top)

//INSTRUCTIONS
//In the serial monitor write:
//'s' stop
//'u' up 1 cm
//'w' up 5 cm
//'d' down 1 cm
//'c' down 5 cm
//'b' bottom (0 cm)
//'t' top (150 cm)

void setup() {
  // put your setup code here, to run once:
pinMode(CW, OUTPUT);
pinMode(CLK, OUTPUT);
pinMode(FCB, INPUT);
pinMode(FCT, INPUT);

digitalWrite(CW, LOW);
digitalWrite(CLK, LOW);

Serial.begin(9600);
}

void loop() {
  // put your main code here, to run repeatedly:

  val=Serial.read();

 if(val=='b'){
  //goes to the bottom (fine corsa posiion zero)
```

```
  digitalWrite(CW, HIGH);
  while (digitalRead(FCB) == HIGH ) {
    digitalWrite(CLK, HIGH);
    delayMicroseconds(timedelay);
    digitalWrite(CLK, LOW);
    delayMicroseconds(timedelay);
  }
  pos=0;
  val='s';
 }

  if(val=='t'){
    //goes to the top (fine corsa position *150*)
  digitalWrite(CW, LOW);
  while (digitalRead(FCT) == HIGH ) {
    digitalWrite(CLK, HIGH);
    delayMicroseconds(timedelay);
    digitalWrite(CLK, LOW);
    delayMicroseconds(timedelay);
  }
  pos=150;
  val='s';
 }

  if(val=='s'){
    //stop, keeps still
    digitalWrite(CW, LOW);
    digitalWrite(CLK, LOW);
    Serial.println(pos);
  }

  if(val=='u'){
    //up, goes 1 cm up
    digitalWrite(CW, LOW);
    while(Distance < cm){
      digitalWrite(CLK, HIGH);
      delayMicroseconds(timedelay);
      digitalWrite(CLK, LOW);
      delayMicroseconds(timedelay);
      Distance = Distance + 1;
    }

    delay(500);
    pos=pos+1;
```

```
    val='s';
    Serial.println(pos);
    Distance = 0;
  }

  if(val=='w'){
    //goes 5 cm up
    digitalWrite(CW, LOW);
    while(Distance < dm){
      digitalWrite(CLK, HIGH);
      delayMicroseconds(timedelay);
      digitalWrite(CLK, LOW);
      delayMicroseconds(timedelay);
      Distance = Distance + 1;
    }

    delay(500);
    pos=pos+5;
    val='s';
    Serial.println(pos);
    Distance = 0;
  }

  if(val=='d'){
    //goes 1 cm down
    digitalWrite(CW, HIGH);
    while(Distance < cm){
      digitalWrite(CLK, HIGH);
      delayMicroseconds(timedelay);
      digitalWrite(CLK, LOW);
      delayMicroseconds(timedelay);
      Distance = Distance + 1;
    }

    delay(500);
    pos=pos-1;
    val='s';
    Serial.println(pos);
    Distance = 0;
  }

    if(val=='c'){
      //goes 5 cm down
    digitalWrite(CW, HIGH);
```

```
    while(Distance < dm){
      digitalWrite(CLK, HIGH);
      delayMicroseconds(timedelay);
      digitalWrite(CLK, LOW);
      delayMicroseconds(timedelay);
      Distance = Distance + 1;
    }

    delay(500);
    pos=pos-5;
    val='s';
    Serial.println(pos);
    Distance = 0;
  }

}
```

Publications

This research activity has led to several publications. These are summarized below.

International Journals

1. A. Vergaerde, T. De Troyer, **A. Carbó Molina**, L. Standaert, M. C. Runacres. "Design, manufacturing and validation of a vertical-axis wind turbine setup for wind tunnel tests", *Journal of Wind Engineering and Industrial Aerodynamics*, vol. 193, October 2019. [https://doi.org/10.1016/j.jweia.2019.103949]
2. **A. Carbó Molina**, T. De Troyer, T. Massai, A. Vergaerde, M. C. Runacres, G. Bartoli "Effect of turbulence on the performance of VAWTs: an experimental study in two different wind tunnels", *Journal of Wind Engineering and Industrial Aerodynamics*, vol. 193, October 2019. [https://doi.org/10.1016/j.jweia.2019.103969]

International Conferences and Workshops

1. **A. Carbó Molina**, G. Bartoli, T. De Troyer. "Wind Tunnel testing of small Vertical-Axis Wind Turbines in Turbulent Flows", in *Proc. of X International Conference on Structural Dynamics, EURODYN 2017*, Rome (Italy), 2017. *3 citations*
2. **A. Carbó Molina**, G. Bartoli, T. De Troyer. "Generation of Uniform Turbulence Profiles in the Wind Tunnel for Urban VAWT Testing", in *Battisti L., Ricci M. (eds) Wind Energy Exploitation in Urban Environment. TUrbWind 2017*, Riva del Garda (Italy), 2017. *3 citations*
3. **A. Carbó Molina**, T. Massai, F. Balduzzi, A. Bianchini, G. Ferrara, T. De Troyer, G. Bartoli. "Combined experimental and numerical study on

the near wake of a Darrieus VAWT under turbulent flows", in *The Science of Making Torque from Wind (TORQUE 2018)* , Milan (Italy), 2018.

4. **A. Carbó Molina**, S. Van de Maele, G. Bartoli, T. De Troyer, M. C. Runacres. "Experimental Characterization of VAWT Airfoils Under Turbulent Flows", in *Battisti L. (eds) Wind Energy Exploitation in Urban Environment. TUrbWind 2018*, Riva del Garda (Italy), 2018.

Bibliography

[A4F, 2014] A4F (2014). AEOLUS4FUTURE Efficient harvesting of the wind energy proposal. Innovative Training Networks (ITN). Technical Report Call: H2020-MSCA-ITN-2014, European Commission.

[A4F, 2016] A4F (2016). AEOLUS4FUTURE website. `http://www.aeolus4future.eu/`. Accessed: 27/09/2018.

[Aeolos, 2015] Aeolos (2015). Aeolos wind turbine, 2015. `http://www.windturbinestar.com/`. Accessed: 26/06/2016.

[Ahmadi-baloutaki et al., 2015] Ahmadi-baloutaki, M., Carriveau, R., and Ting, D. S. (2015). Performance of a vertical axis wind turbine in grid generated turbulence. *Sustainable Energy Technologies and Assessments*, 11:178–185.

[Amandolèse and Széchényi, 2004] Amandolèse, X. and Széchényi, E. (2004). Experimental study of the effect of turbulence on a section model blade oscillating in stall. *Wind Energy*, 7(4):267–282.

[Anup et al., 2019] Anup, K., Whale, J., and Urmee, T. (2019). Urban wind conditions and small wind turbines in the built environment: A review. *Renewable Energy*, 131:268 – 283.

[Araya et al., 2017] Araya, D. B., Colonius, T., and Dabiri, J. O. (2017). Transition to bluff-body dynamics in the wake of vertical-axis wind turbines. *Journal of Fluid Mechanics*, 813:346–381.

[Aslam Bhutta et al., 2012] Aslam Bhutta, M. M., Hayat, N., Farooq, A. U., Ali, Z., Jamil, S. R., and Hussain, Z. (2012). Vertical axis wind turbine - A review of various configurations and design techniques. *Renewable and Sustainable Energy Reviews*, 16(4):1926–1939.

[Bachant and Wosnik, 2016] Bachant, P. and Wosnik, M. (2016). Effects of Reynolds number on the energy conversion and near-wake dynamics of a high solidity vertical-axis cross-flow turbine. *Energies*, 9(2):1–18.

[Baines and Peterson,] Baines, W. and Peterson, E. An investigation of flow through screens. *Trans. Am. Soc. Mech. Engrs.*

[Balduzzi et al., 2016] Balduzzi, F., Bianchini, A., Ferrara, G., and Ferrari, L. (2016). Dimensionless numbers for the assessment of mesh and timestep requirements in CFD simulations of Darrieus wind turbines. *Energy Conversion and Management*, (136):318–328.

[Balduzzi et al., 2019] Balduzzi, F., Zini, M., Ferrara, G., and Bianchini, A. (2019). Development of a Computational Fluid Dynamics Methodology to Reproduce the Effects of Macroturbulence on Wind Turbines and Its Application to the Particular Case of a VAWT. *Journal of Engineering for Gas Turbines and Power*, 141(11). 111010.

[Barlow et al., 1999] Barlow, J., Rae, W. H., and Pope, A. (1999). *Low-speed wind tunnel testing.* John Wiley & Sons.

[Barlow, 2014] Barlow, J. F. (2014). Urban Climate Progress in observing and modelling the urban boundary layer. *Urban Climate*, 10:216–240.

[Battisti, 2012] Battisti, L. (2012). *Gli impianti motori eolici.* Lorenzo Battisti Editore.

[Battisti et al., 2016] Battisti, L., Zanne, L., Anna, S. D., Dossena, V., Persico, G., and Paradiso, B. (2016). Aerodynamic Measurements on a Vertical Axis Wind Turbine in a Large Scale Wind Tunnel. 133(September 2011):1–9.

[Bearman and Morel, 1983] Bearman, P. W. and Morel, T. (1983). Effect of free stream turbulence on the flow around bluff bodies. *Prog. Aerospace Sciences*, 20:97–123.

[Bertényi et al., 2010] Bertényi, T., Wickins, C., and Mcintosh, S. (2010). Enhanced Energy Capture Through Gust-Tracking in the Urban Wind Environment. In *48th AIAA Aerospace Sciences Meeting and Exhibit*, number January.

[Biadgo and Simonovic, 2012] Biadgo, A. M. and Simonovic, A. (2012). Numerical investigation of vertical axis wind turbine. *The 15th International Conference on Fluid Flow Technologies*, 41(February 2013):49–58.

[Bianchini et al., 2017a] Bianchini, A., Balduzzi, F., Bachant, P., Ferrara, G., and Ferrari, L. (2017a). Effectiveness of two-dimensional CFD simulations for Darrieus VAWTs : a combined numerical and experimental assessment. *Energy Conversion and Management*, 136:318–328.

[Bianchini et al., 2017b] Bianchini, A., Balduzzi, F., Ferrara, G., Persico, G., and Battisti, L. (2017b). Detailed analysis of the wake structure of a straight-blade H-Darrieus wind turbine by means of wind tunnel experiments and CFD simulations. In *ASME Turbo Expo 2017*, pages 1–11.

[Bianchini et al., 2011] Bianchini, A., Ferrari, L., and Magnani, S. (2011). Start-up behavior of a three-bladed H-Darrieus VAWT: experimental and numerical analysis. In *ASME Turbo Expo 2011*, pages 1–10.

[Bianchini et al., 2015] Bianchini, A., Rainbird, J. M., Marta, S., Marta, S., Graham, J. M. R., and Ferrara, G. (2015). An Experimental and Numerical Assessment of Airfoil Polars for use in Darrieus Wind Turbines. Part 1 - Flow Curvature effects. In *Proceedings of the ASME Turbo Expo 2015*, pages 1–12.

[Blackwell et al., 1977] Blackwell, B. F., Sheldahl, R. E., and Feltz, L. V. (1977). Wind Tunnel Performance Data for two- and three-Bucket Savonius Rotors. Technical report, Sandia National Laboratories.

[bobmcgov, 2016] bobmcgov (2016). The trailer sailor forum, 2016. `http://forum.trailersailor.com/post.php?id=1405754`. Accessed: 21/06/2016.

[Brahimi, 1970] Brahimi, M. (1970). Analyse aérodynamique d'un rotor Darrieus en présence d'un vent turbulent. Technical report, University of Montreal.

[Brochier et al., 1986] Brochier, G., Fraunie, P., and Beguier, C. (1986). Water Channel Experiments of Dynamic Stall on Darrieus Wind Turbine Blades. *J. PROPULSION*, 2(5):445–449.

[Brown, 2009] Brown (2009). Wikimedia commons 2009. `https://commons.wikimedia.org/wiki/File:Vindm%C3%B8lleparken_N%C3%B8rrek%C3%A6r_enge_091013.jpg`. Accessed: 18/05/2016.

[Buckingham, 2010] Buckingham, S. (2010). Wind park sitting in complex terrains assessed by wind tunnel simulations. Technical Report June, Von Karman Intitute for Fluid Dynamics.

[Burton et al., 2001] Burton, T., Sharpe, D., Jenkins, N., and Bossanyi, E. (2001). *Wind Energy Handbook*. John Wiley & Sons.

[Carbó Molina et al., 2018] Carbó Molina, A., Massai, T., Balduzzi, F., Bianchini, A., Ferrara, G., De Troyer, T., and Bartoli, G. (2018). Combined experimental and numerical study on the near wake of a Darrieus VAWT under turbulent flows. In *Journal of Physics: Conference Series 1037*.

[Clark, 2012] Clark, B. (2012). Helix collapse fails to crush hope for vertical wind turbines, 2012. `http://news.nationalgeographic.com/news/energy/2012/08/120820-helix-wind-collapse/`. Accessed: 21/06/2016.

[Coudou et al., 2017] Coudou, N., Buckingham, S., and Van Beeck, J. (2017). Experimental study on the wind-turbine wake meandering inside a scale model wind farm placed in an atmospheric-boundary-layer wind tunnel. *Journal of Physics: Conference Series*, 854(1).

[Dabiri, 2011] Dabiri, J. O. (2011). Potential order-of-magnitude enhancement of wind farm power density via counter-rotating vertical-axis wind turbine arrays. *Journal of Renewable and Sustainable Energy*, 3(4):1–12.

[Dallman, 2013] Dallman, A. R. (2013). *Flow and turbulence in urban areas*. PhD thesis, University of Notre Dame.

[Darrieus, 1931] Darrieus, G. (1931). Turbine having its rotating shaft transverse to the flow of the current. Technical report, US patent US1835018 A.

[Dénos, 2005] Dénos, R. (2005). *Fundamentals of data acquisition and processing. Course note 171*. Von Karman Istitute for Fluid Dynamics.

[Devinant et al., 2002] Devinant, P., Laverne, T., and Hureau, J. (2002). Experimental study of wind-turbine airfoil aerodynamics in high turbulence. *Journal of Wind Engineering and Industrial Aerodynamics*, 90(6):689–707.

[Dossena et al., 2015] Dossena, V., Persico, G., Paradiso, B., Battisti, L., Dell'Anna, S., Brighenti, A., and Benini, E. (2015). An Experimental Study of the Aerodynamics and Performance of a Vertical Axis Wind Turbine in a Confined and Unconfined Environment. *Journal of Energy Resources Technology*, 137(5):051207.

[Drew et al., 2013] Drew, D. R., Barlow, J. F., and Cockerill, T. T. (2013). Estimating the potential yield of small wind turbines in urban areas : A case study for Greater London , UK. *Jnl. of Wind Engineering and Industrial Aerodynamics*, 115:104–111.

[Dunne, 2016] Dunne, R. (2016). *Dynamic Stall on Vertical Axis Wind Turbine Blades*. PhD thesis, California Institute of Technology.

[Echeverria, 2018] Echeverria, J. (2018). Manufacturing and Testing of a VAWT blade. Technical report, Vrije Universiteit Brussel.

[Euromech, 2016] Euromech (2016). European Mechanics Society. Colloquium 583. Scientific and Technological Challenges in Offshore Vertical Axis Wind Turbines, 2016. `http://583.euromech.org/`. Accessed: 09/10/2018.

[European Commission, 1997] European Commission (1997). Communication from the Commission Energy for the future: renewable sources of energy. White Paper for a Community Strategy and Action Plan. Technical Report 97.

[EWEA, 2016] EWEA (2016). Wind in power, 2015 European statistics. Technical Report February.

[Ferreira, 2009a] Ferreira, C. J. S. S. (2009a). *The near wake of the VAWT: 2D and 3D views of the VAWT aerodynamics*. PhD thesis.

[Ferreira, 2009b] Ferreira, C. S. (2009b). The VAWT in skew: stereo-PIV and vortex modeling. (January).

[Ferreira et al., 2014] Ferreira, C. S., Madsen, H. A., Barone, M., Roscher, B., Deglaire, P., and Arduin, I. (2014). Comparison of aerodynamic models for vertical axis wind turbines. *Journal of Physics: Conference Series*, 524(1).

[Gasch, 2012] Gasch, R. (2012). *Wind Power Plants*. Springer.

[Gipe, 2013] Gipe, P. (2013). P. Gipe. FloWind: The World's Most Successful VAWT (Vertical Axis Wind Turbine), 2013. `http://www.wind-works.org/`. Accessed: 22/06/2016.

[GWEC, 2015] GWEC (2015). Global Wind Report.

[H2020, 2018] H2020 (2018). Horizon 2020 website, 2018. `https://ec.europa.eu/programmes/horizon2020/en/`. Accessed: 27/09/2018.

[Hand and Cashman, 2017] Hand, B. and Cashman, A. (2017). Conceptual design of a large-scale floating offshore vertical axis wind turbine. *Energy Procedia*, 142(December 2017):83–88.

[Hau, 2006] Hau, E. (2006). *Wind Turbines*. Springer.

[Hi-VAWT, 2012] Hi-VAWT (2012). Hi-VAWT Technology Corp, 2012. `http://www.hi-vawt.com.tw/en`. Accessed: 23/06/2016.

[Hoffmann, 1991] Hoffmann, J. A. (1991). Effects of freestream turbulence on the performance characteristics of an airfoil. *AIAA Journal*, 29(9):1353–1354.

[Hohman et al., 2018] Hohman, T. C., Martinelli, L., and Smits, A. J. (2018). The effects of inflow conditions on vertical axis wind turbine wake structure and performance. *Journal of Wind Engineering and Industrial Aerodynamics*, 183(October):1–18.

[Howell et al., 2010] Howell, R., Qin, N., Edwards, J., and Durrani, N. (2010). Wind tunnel and numerical study of a small vertical axis wind turbine. *Renewable Energy*, 35(2):412–422.

[IEA, 2018] IEA (2018). IEA Wind TCP Task 27, 2018. `https://community.ieawind.org/task27/home`. Accessed: 24/10/2018.

[ITTC, 2008] ITTC (2008). Recommended Procedures and Guidelines - Uncertainty Analysis: Particle Imaging Velocimetry (PIV). *25th International Towing Tank Conference, Fukuoka*, pages 1–12.

[Jacobs and Sherman, 1937] Jacobs, E. N. and Sherman, A. (1937). Airfoil section characteristics as affected by variation of the Reynolds number. Technical report.

[Jeong et al., 2014] Jeong, H., Lee, S., and Kwon, S.-d. (2014). Wind tunnel interference effects on power performance of small Darrieus wind turbines. In *Advances in Civil, Environmental, and Materials Research (ACEM14)*.

[Jiménez, 2004] Jiménez, J. (2004). The Contributions of A. N. Kolmogorov to the theory of turbulence. *Arbor: Ciencia, Pensamiento y Cultura*, 178.

[Kirchner, 2001] Kirchner, J. (2001). Data Analysis Toolkit #5: Uncertainty Analysis and Error Propagation. Technical report, University of California, Berkeley.

[Kirke and Lazauskas, 1993] Kirke, B. and Lazauskas, L. (1993). Experimental verification of a mathematical model for predicting the performance of a self-acting variable pitch vawt. *Wind Engineering*, 17(2).

[Kooiman and Tullis, 2015] Kooiman, S. and Tullis, S. (2015). Response of a Vertical Axis Wind Turbine to Time Varying Wind Conditions found within the Urban Environment. *Wind Energy*, (January).

[Kröger et al., 2018] Kröger, L., Frederik, J., van Wingerden, J.-W., Peinke, J., and Hölling, M. (2018). Generation of user defined turbulent inflow conditions by an active grid for validation experiments. *Journal of Physics: Conference Series*, 1037:052002.

[Kubo and Kato, 1986] Kubo, Y. and Kato, K. (1986). The role of end plates in two dimensional wind tunnel tests. *Structural Engineering and Earthquake Engineering*, 3:167–174.

[Laneville, 1973] Laneville, A. (1973). *Effects of turbulence on wind induced vibrations of bluff cylinders*. PhD thesis, Laval University , Quebec.

[Lee et al., 2018] Lee, K.-Y., Tsao, S.-H., Tzeng, C.-W., and Lin, H.-J. (2018). Influence of the vertical wind and wind direction on the power output of a small vertical-axis wind turbine installed on the rooftop of a building. *Applied Energy*, 209(September 2017):383–391.

[Lubitz, 2014] Lubitz, W. D. (2014). Impact of ambient turbulence on performance of a small wind turbine. *Renewable Energy*, 61:69–73.

[Lux, 2015] Lux (2015). Lux wind turbines, 2015. `http://www.luxwindturbines.com/`. Accessed: 23/06/2016.

[Maldonado et al., 2015] Maldonado, V., Castillo, L., Thormann, A., and Meneveau, C. (2015). The role of free stream turbulence with large integral scale on the aerodynamic performance of an experimental low Reynolds number S809 wind turbine blade. *Journal of Wind Engineering and Industrial Aerodynamics*, 142:246–257.

[Mannini et al., 2015] Mannini, C., Marra, A. M., Pigolotti, L., and Bartoli, G. (2015). Unsteady pressure and wake characteristics of a benchmark rectangular section in smooth and turbulent flow. In *14th International Conference on Wind Engineering*, pages 1–20.

[Maskell, 1987] Maskell, E. (1987). A theory of the blockage effects on bluff bodies and stalled wings in a closed wind tunnel. Technical report, Aeronautical Research Council.

[Mathew, 2006] Mathew, S. (2006). *Wind Energy Fundamentals, Resource Analysis and Economics*. Springer Berlin Heidelberg.

[McCroskey, 1981] McCroskey, W. J. (1981). The phenomenon of dynamic stall. Technical report, Ames Research Center, NASA, Moffett Field, California.

[Mertens, 2006] Mertens, S. (2006). Wind Energy in the Built Environment Concentrator Effects of Buildings. Technical report, Technische Universiteit Delft.

[Mertens and Bussel, 2003] Mertens, S. and Bussel, G. V. (2003). Performance of an H-Darrieus in the Skewed Flow on a Roof. *Journal of Solar Energy Engineering*, 125(November).

[Miau, 2012] Miau, J. J. (2012). Wind tunnel study on aerodynamic performance of small vertical-axis wind turbines. Technical report, Cheng Kung University, Taiwan.

[Miller et al., 2018] Miller, M. A., Duvvuri, S., Brownstein, I., Lee, M., Dabiri, J. O., and Hultmark, M. (2018). Vertical-axis wind turbine experiments at full dynamic similarity. *Journal of Fluid Mechanics*, 844:707–720.

[Möllerström et al., 2016] Möllerström, E., Ottermo, F., Goude, A., Eriksson, S., Hylander, J., and Bernhoff, H. (2016). Turbulence influence on wind energy extraction for a medium size vertical axis wind turbine. *Wind Energy*, 19(February):1963–1973.

[Olivari and Benocci, 2013] Olivari, D. and Benocci, C. (2013). *An Introduction to the Mechanics of Turbulence. Course note 157.* Von Karman Institute for Fluid Dynamics.

[Pagnini et al., 2015] Pagnini, L. C., Burlando, M., and Repetto, M. P. (2015). Experimental power curve of small-size wind turbines in turbulent urban environment. *Applied Energy*, 154:112–121.

[Paraschivoiu, 2002] Paraschivoiu, I. (2002). *Wind Turbine Design: With Emphasis on Darrieus Concept.* Presses inter Polytechnique.

[Paraschivoiu et al., 2017] Paraschivoiu, I., Ammar, S., and Saeed, F. (2017). VAWT vs. HAWT: a comparative performance study of 2-6 MW rated capacity turbines. In *International Symposium on Wind and Tidal Power*, pages 1–27, Montreal, Quebec, Canada.

[Peng and Lam, 2016] Peng, H. Y. and Lam, H. F. (2016). Turbulence effects on the wake characteristics and aerodynamic performance of a straight-bladed vertical axis wind turbine by wind tunnel tests and large eddy simulations. *Energy*, 109:557–568.

[Pierre5018, 2012] Pierre5018 (2012). Pierre5018 [public domain], via wikimedia commons, 2012. `https://commons.wikimedia.org/wiki/File:Eole_Cap-Chat.jpg`. Accessed: 22/06/2016.

[Pope and Harper, 1966] Pope, A. and Harper, J. (1966). *Low Speed Wind Tunnel Testing.* John Wiley and Sons.

[Porté-Agel et al., 2019] Porté-Agel, F., Bastankhah, M., and Shamsoddin, S. (2019). Wind-turbine and wind-farm flows: A review. *Boundary-Layer Meteorology.*

[Price, 2006] Price, T. J. (2006). UK Large-Scale Wind Power Programme From 1970 to 1990 : The Carmarthen Bay Experiments. *Wind Engineering*, 44(0).

[Ragheb, 2013] Ragheb, M. (2013). M. Ragheb. Historical Wind Generators Machines, 2013. Wind Power Systems course notes, University of Illinois at Urbana-Champaign, USA.

[Rainbird et al., 2015] Rainbird, J. M., Bianchini, A., Balduzzi, F., Peiró, J., Graham, J. M. R., Ferrara, G., and Ferrari, L. (2015). On the influence of virtual camber effect on airfoil polars for use in simulations of Darrieus wind turbines. *Energy Conversion and Management*, 106:373–384.

[Ramin, 2012] Ramin (2012). Historical Iranian sites and people. `http://historicaliran.blogspot.it/2012/03/nashtifan-windmills.html`. Accessed: 12/04/2016.

[Rezaeiha et al., 2017] Rezaeiha, A., Kalkman, I., Montazeri, H., and Blocken, B. (2017). Effect of the shaft on the aerodynamic performance of urban vertical axis wind turbines. *Energy Conversion and Management*, 149(July):616–630.

[Rezaeiha et al., 2018] Rezaeiha, A., Montazeri, H., and Blocken, B. (2018). Characterization of aerodynamic performance of vertical axis wind turbines: Impact of operational parameters. *Energy Conversion and Management*, 169(February):45–77.

[Roach, 1986] Roach, P. E. (1986). The generation of nearly isotropic turbulence by means of grids. *Heat and Fluid Flow*, (December):82–92.

[Ropatec, 2013] Ropatec (2013). Ropatec s.r.l., 2013. `http://www.ropatec.it/`. Accessed: 23/06/2016.

[Rosato, 2015] Rosato, M. (2015). *Progettazione di Microturbine Eoliche*. EPC Editore.

[Ross and Altman, 2011] Ross, I. and Altman, A. (2011). Wind tunnel blockage corrections: Review and application to Savonius vertical-axis wind turbines. *Journal of Wind Engineering and Industrial Aerodynamics*, 99(5):523–538.

[Roth, 1999] Roth, M. (1999). Review of atmospheric turbulence over cities. *Q. J. R. Meteorol. Soc*, 126.

[Savonius, 1925] Savonius, S. (1925). Rotor adapted to be driven by wind or flowing water. Technical report, US patent US1697574 A.

[Schlichting, 1979] Schlichting, H. (1979). *Boundary layer theory*. McGraw Hill.

[Sheldahl, 1981] Sheldahl, R. E. (1981). Comparison of Field and Wind Tunnel Darrieus Wind Turbine Data. Technical report, Sandia National Laboratories.

[Sheldahl and Klimas, 1981] Sheldahl, R. E. and Klimas, P. (1981). Aerodynamic Characteristics of Seven Symmetrical Airfoil Sections Through 180-Degree Angle of Attack for Use in Aerodynamic Analysis of Vertical Axis Wind Turbines. Technical report, Sandia National Laboratories.

[Stathopoulos et al., 2018] Stathopoulos, T., Alrawashdeh, H., Al-Quraan, A., Blocken, B., Dilimulati, A., Paraschivoiu, M., and Pilay, P. (2018). Urban wind energy: Some views on potential and challenges. *Journal of Wind Engineering and Industrial Aerodynamics*, 179:146 – 157.

[Staunited, 2018] Staunited (2018). M. Brown [Public domain], via Wikimedia Commons, 1975. `https://commons.wikimedia.org/wiki/File%3ANASA_MOD-0_Plum_Brook_OH_1975_03490L.jpg`. Accessed: 18/05/2016.

[Sucoplus, 2010] Sucoplus (2010). Wikimedia commons, 2010. `https://commons.wikimedia.org/wiki/File:Molinos_mota_del_cuervo.jpg`. Accessed: 12/04/2016.

[Sutherland et al., 2012] Sutherland, H. J., Berg, D. E., and Ashwill, T. D. (2012). A Retrospective of VAWT Technology. Technical Report January, Sandia National Laboratories.

[Tavoularis, 2002] Tavoularis, S. (2002). Turbulent flow. In *Fluid Flow Handbook*, chapter 31. McGraw-Hill.

[Templin, 1974] Templin, R. (1974). Aerodynamic Performance Theory for the NRC Vertical-axis Wind Turbine. Technical report, National Research Council Canada, National Aeronautical Establishment.

[Templin and Rangi, 1983] Templin, R. J. and Rangi, R. S. (1983). Vertical-axis wind turbine development in Canada. In *IEE Proceedings*, volume 130, pages 555–561.

[Tescione et al., 2014] Tescione, G., Ragni, D., He, C., Ferreira, C. J. S., and Bussel, G. J. W. V. (2014). Near wake flow analysis of a vertical axis wind turbine by stereoscopic particle image velocimetry. *Renewable Energy*, 70:47–61.

[Tong, 2010] Tong, W. (2010). *Wind Power Generation and Wind Turbine Design*. WIT Press.

[Turby, 2005] Turby (2005). The wind turbine for the built-up environment. Technical report.

[UGE, 2016] UGE (2016). UGE International Ltd. `http://www.ugei.com/`. Accessed: 28/06/2016.

[UN, 2007] UN (2007). United Nations: City planning will determine pace of global warming, 2007. `http://www.un.org/News/Press/docs/2007/gaef3190.doc.htm`. Accessed: 09/10/2018.

[Van de Maele, 2018] Van de Maele, S. (2018). Designing, making and testing of a NACA 0018 wind tunnel model equipped with pressure taps. Technical report, Vrije Universiteit Brussel, Belgium.

[Van Dyke, 1982] Van Dyke, M. (1982). *An Album of Fluid Motion*. The Parabolic Press.

[Veljkovic, 2016] Veljkovic, M. (2016). Design of supporting structures of onshore wind turbines. In *Advances in Wind Energy Technology. WINERCOST 2nd International Training School*, Chania, Greece.

[Vergaerde et al., 2019] Vergaerde, A., De Troyer, T., Carbó Molina, A., Standaert, L., and Runacres, M. (2019). Design, manufacturing and validation of a vertical-axis wind turbine setup for wind tunnel tests. *Journal of Wind Engineering and Industrial Aerodynamics*, 193(October):103949.

[Vergaerde et al., 2018] Vergaerde, A., Troyer, T. D., Kluczewska-Bordier, J., Parneix, N., Silvert, F., and Runacres, M. C. (2018). Wind tunnel experiments of a pair of interacting vertical-axis wind turbines. *Journal of Physics: Conference Series*, 1037:072049.

[Vita et al., 2018] Vita, G., Hemida, H., Andrianne, T., and Baniotopoulos, C. C. (2018). Generating atmospheric turbulence using passive grids in an expansion test section of a wind tunnel. *Journal of Wind Engineering & Industrial Aerodynamics*, 178(February):91–104.

[Windside, 2009] Windside (2009). Oy Windside Ltd. `http://www2.windside.com/products.html`. Accessed: 23/06/2016.

[Wire, 2009] Wire, B. (2009). Bussiness Wire. Mariah Power Launches Windspire Vertical Wind Turbine in Europe. `http://www.businesswire.com/news/home/20090825006204/en/Mariah-Power-Launches-Windspire%C2%AE-Vertical-Wind-Turbine`. Accessed: 26/06/2016.

[WWEA, 2014] WWEA (2014). World Wind Energy Association. `https://wwindea.org/`. Accessed: 21/10/2018.